The Thesis Committee for Doo Hyun Chung
Certifies that this is the approved version of the following thesis:

Transport of Nanoparticles during Drainage and Imbibition Displacements in Porous Media

APPROVED BY
SUPERVISING COMMITTEE:

Supervisor:

Steven L. Bryant

David A. DiCarlo

Transport of Nanoparticles during Drainage and Imbibition Displacements in Porous Media

by

Doo Hyun Chung, B.S.E

Thesis

Presented to the Faculty of the Graduate School of

The University of Texas at Austin

in Partial Fulfillment

of the Requirements

for the Degree of

Master of Science in Engineering

The University of Texas at Austin

August 2013

Dedication

To God and to my family.

Acknowledgements

I would like to first acknowledge Dr. Steven Bryant for his guidance through my graduate studies. His insights and feedbacks extended my research far beyond what I could imagine. I would also like to thank Dr. David DiCarlo and Dr. Chun Huh for their advice and help during my research.

Special thanks go to Tarek Hariz, Behdad Aminzadeh and Roy Wung, who helped me with experimentations throughout my time here. Also, I would like to acknowledge Tiantian (Tina) Zhang, Haiyang Yu, James Patterson, and Scott Gabel for their company and feedback.

I would like to thank Glen Baum and Gary Miscoe for helping with experimental set-up and preparations, Barbara Messmore for being helpful and prompt in ordering required materials and equipment, Dr. Do Hoon Kim for generously allowing me to use the rheometer in Dr. Pope's lab, Joanna Castillo for granting me access to old research materials and Roger Terzian for setting up the computer.

Finally, I would like to thank 3M Co., Nyacol, Inc. and Nissan Chemical America Corp. for generously donating nanoparticles in support of this research.

This research was funded by the Center for Frontiers of Subsurface Energy Security (CFSES), an Energy Frontier Research Center funded by the U.S. Department of Energy, Office of Science, Office of Basic Energy Sciences under award DE-SC0001114.

Abstract

Transport of Nanoparticles during Drainage and Imbibition Displacements in Porous Media

Doo Hyun Chung, M.S.E.

The University of Texas at Austin, 2013

Supervisor: Steven L. Bryant

During carbon dioxide (CO_2) sequestration, CO_2 injection suffers from viscous fingering and low sweep efficiency. In addition, the lower density of CO_2 compared to in-situ brine leads to the possibility of sequestered CO_2 rising up through the relatively permeable path in the cap rock and being emitted back out to the atmosphere. This research proposes a mechanism of CO_2-in-brine emulsion stabilization by surface-coated nanoparticles as a potential cure for these problems. This mechanism is studied in detail by conducting a series of core floods to investigate the interactions between nanoparticles and the surroundings such as fluids and rock surfaces during nanoparticle transport in sedimentary rocks.

The experiments presented here use n-octane as a low-pressure analog fluid to supercritical CO_2 as they share several key characteristics. Comparisons of pressure drop and CT images from drainage displacement experiments with and without nanoparticles show that nanoparticle-stabilized emulsions were generated in-situ in highly permeable

and homogeneous Boise sandstones tested in this study. Roof snap-off is proposed as the key mechanism for generating the emulsions.

The imbibition experiment presents a case where Roof snap-off does not occur. The pressure drop for the control experiment and the nanoparticle experiments confirmed that without Roof snap-off nanoparticles do not affect the dynamics of the displacement except for the viscosity increase of the aqueous phase. However, it was inferred from the saturation profiles and effluent concentration history that nanoparticles were traveling faster than the aqueous phase in which they were dispersed and accumulating at the main displacement front. Inaccessible pore volume is proposed as a mechanism responsible for the accelerated transport of nanoparticles.

The single-phase flow experiments demonstrate the accelerated transport of nanoparticles in porous media that was invoked to explain observations during imbibition displacement. During these experiments, tracer and nanoparticles were simultaneously injected into a porous medium and their effluent concentrations were monitored using a UV-Vis detector. The results show that nanoparticles traveled faster than the tracer in Boise and Berea sandstones studied in this research. Two-site model developed by Zhang (2012) was used to fit the data. Simulations suggested that the two-site model could replicate the overall shape of the experimental data when a slug of nanoparticle dispersion was injected, but it was not able to accurately predict the leading edge and the trailing edge of the effluent concentration history, where nanoparticles appeared before tracer due to accelerated transport. To account for the enhanced transport of nanoparticles, a modified two-site model with an acceleration factor, E, is proposed. The resulting fit matched the experimental data better than the original two-site model.

Table of Contents

List of Tables

List of Figures

Chapter 1

Introduction

During the last decade, nanotechnology has garnered a serious scientific attention and produced many notable achievements. Properties of nanomaterials, including color, hardness, conductivity, and thermodynamic effects such as melting temperature and specific heat capacity, often differ from those of bulk materials due to the large percentage of atoms at the surface. With the ability to synthesize materials at nanoscale, scientists can now engineer materials with desired properties. In medical science, for example, nanomaterials are used to deliver medicine and target specific cells such as cancer or brain tumor cells (Cho et al., 2008). In electronics, nano-RAM is a denser and less expensive alternative to DRAM and can retain memory despite loss of power (Rueckets et al., 2000). In apparel industry, silver and gold nanomaterials are used to make clothings that can repel dirt, water, and odors (Patra and Gouda, 2013).

In the petroleum industry, the opportunities presented by nanotechnology also abound. Nano-engineered polymers (Stuart et al., 2010) that change material properties in response to varying environmental conditions, such as temperature, pH, electrical potential difference, and moisture can increase the overall efficiency of chemical enhanced oil recovery (EOR). Nanopaint with external magnetic field can provide localized heating for pipelines carrying heavy oil (Davidson, 2012). Nanoparticles suspended in aqueous phase have also shown potential as a conformance agent for increasing sweep efficiency during carbon dioxide (CO_2) EOR (Hariz, 2012).

This thesis focuses on applications of surface-treated silica nanoparticles for CO_2 sequestration. Geologic CO_2 sequestration is considered a viable and economical method in a portfolio of technologies aimed to reduce greenhouse gas emissions. There are four

main trapping mechanisms once the CO_2 is placed with a geologic formation: Structural/stratigraphic trapping, residual trapping, solubility trapping, and mineral trapping. Structural trapping relies heavily on the integrity of the overlaying cap rock; any structural infirmities will lead to possibilities of CO_2 leakage through relatively permeable path back into the atmosphere. In this thesis, a foam-generation mechanism aided by surface-treated nanoparticles is demonstrated as a potential cure for such potential leakage. Another aspect of trapping mechanism highlighted in this thesis is residual trapping. By similar argument that nanoparticles are a potential conformance agent for CO_2 EOR, nanoparticle-stabilized foam can be used to increase the sweep efficiency of CO_2 injection during a sequestration project and to lead to a more robust capillary trapping of CO_2. In addition, transport of nanoparticles in porous media, as additives in chase water to push CO_2 away from the injection site to the storage site, is discussed in detail.

1.1 THESIS OUTLINE

There are a total of six chapters in this thesis. In the first introductory chapter, an overview of nanotechnology and its applications in the petroleum industry and CO_2 sequestration is provided, followed by the research objectives. The second chapter is a literature review of physics and background works related to this study. In the third chapter, experimental procedures and results for drainage displacement experiments bring up a potential preventive measure to securitize geological sequestration of CO_2. In the fourth chapter, experimental procedures and results for imbibition displacement experiments present ways to improve the efficiency of CO_2 storage. The fifth chapter explores the transport of nanoparticles in porous media during single-phase flow and

provides an explanation to an anomalous phenomenon observed during imbibition displacement experiments. The final sixth chapter summarizes the conclusions from the thesis and outlines recommendations for future work.

1.2 RESEARCH OBJECTIVES

The fundamental objective of this research is to investigate how nanoparticles interact with surrounding components such as fluids and rock surface during nanoparticle transport in porous media. More specifically, the effect of nanoparticles on the dynamics of drainage and imbibition displacements will be investigated. The findings are put into context of CO_2 sequestration to pinpoint possible utilizations of engineered nanoparticles to further securitize and enhance geological storage of CO_2.

Chapter 2

Literature Review

2.1 NANOPARTICLE-STABILIZED EMULSION

An emulsion is a mixture of two immiscible fluids where droplets of one phase are surrounded by another, traditionally stabilized by surfactants. About a century ago, Pickering (1907) discovered that small colloidal particles can also stabilize droplets of oil in bulk water phase by adsorbing on the oil-water interface.

For oilfield applications, Bragg (1999) and Bragg and Varadaraj (2003) discuss advantages and disadvantages of using colloidal particles as emulsifier. Some of the advantages are: 1) low-cost colloidal solids such as clay can be used as emulsifiers, 2) with a tweak of parameters such as concentration, salinity and pH, emulsions with high apparent viscosity can be generated for effective mobility control and 3) colloidal particles are versatile in that both water-in-oil and oil-in-water emulsion can be stabilized depending on the particles' wettability. Figure 2.1 shows the relationship between contact angle and the position of a spherical particle at the oil-water interface and the resulting emulsion morphology based on the contact angle (Dickson et al., 2004).

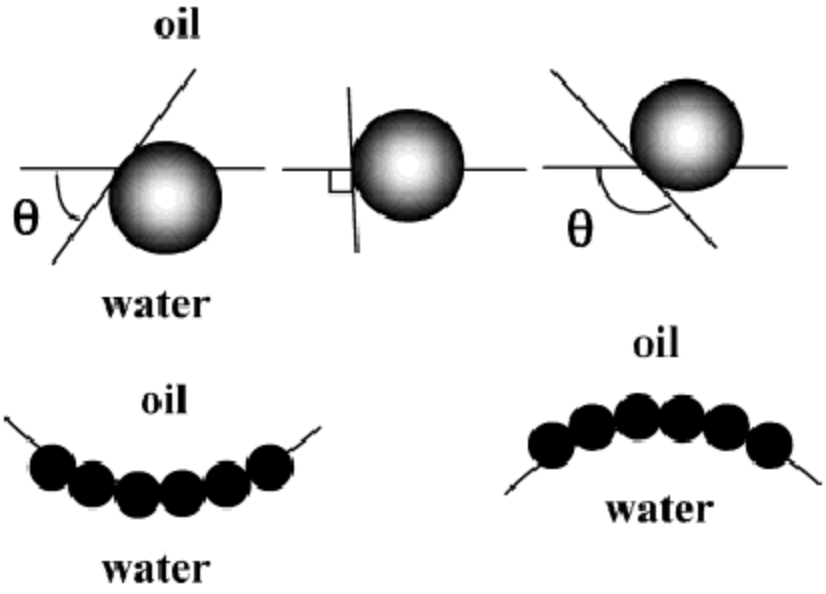

Figure 2.1: Contact angle on oil-water interface and its relationship to emulsion structure (Dickson et al., 2004).

In the left panel of Figure 2.1, hydrophilic particles have a contact angle less than 90° and the majority of the particle resides in the water phase. As a result, the interface bends around the oil droplet, resulting in oil-in-water emulsion. Hydrophobic particles have a contact angle greater than 90°, as in the right panel of Figure 2.1. The majority of the particle resides in the oil phase and the interface bends around the water phase, resulting in water-in-oil emulsion (Dickson et al., 2004).

A disadvantage of using colloidal particles is the high tendency of straining in pore throats and filtration, leading to loss of particles to the rock and reduction in permeability. Colloidal particles often have a wide size distribution which makes it difficult to control the quality and texture of emulsions. Using nanoparticles instead of "microparticles" allows us to circumvent these weaknesses of colloidal particles. Because of their small size, nanoparticles can travel long distances in reservoir rocks with little or no retention and uniform size distribution can be manufactured with ease.

Another big advantage of using nanoparticles is that the core material and the surrounding coatings (Figure 2.2) can be tailored for different applications. For example, the core materials can be made from environmentally benign silica or ferromagnetic substances that can be subject to external control by magnetic field and the outside coating can be catalytic, reactive, or associative with surfactant molecules (Zhang et al., 2009).

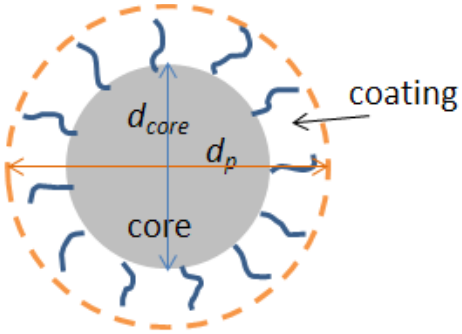

Figure 2.2: Schematic of a surface-treated nanoparticle (Zhang 2012).

In order to bring nanoparticles to the oil-water interface, a significant amount of energy is required. This adsorption energy, *E*, is given by the following equation (Binks and Horozov, 2006):

$$E = \pi r^2 \gamma_{\alpha\beta}(1 \pm \cos\theta)^2$$

where r is the radius of the particle, $\gamma_{\alpha\beta}$ is the interfacial tension, and θ is the contact angle of the particle at the interface as measured through the aqueous phase. For n-octane and water, the interfacial tension is 51 mN/m at 25℃. Assuming that the radius of the nanoparticle is 14 nm as is for Nyacol's DP9711 nanoparticles used in this study, the adsorption energy of a spherical particle at the planar n-octane-water interface as a function of contact angle is calculated and graphed in Figure 2.3.

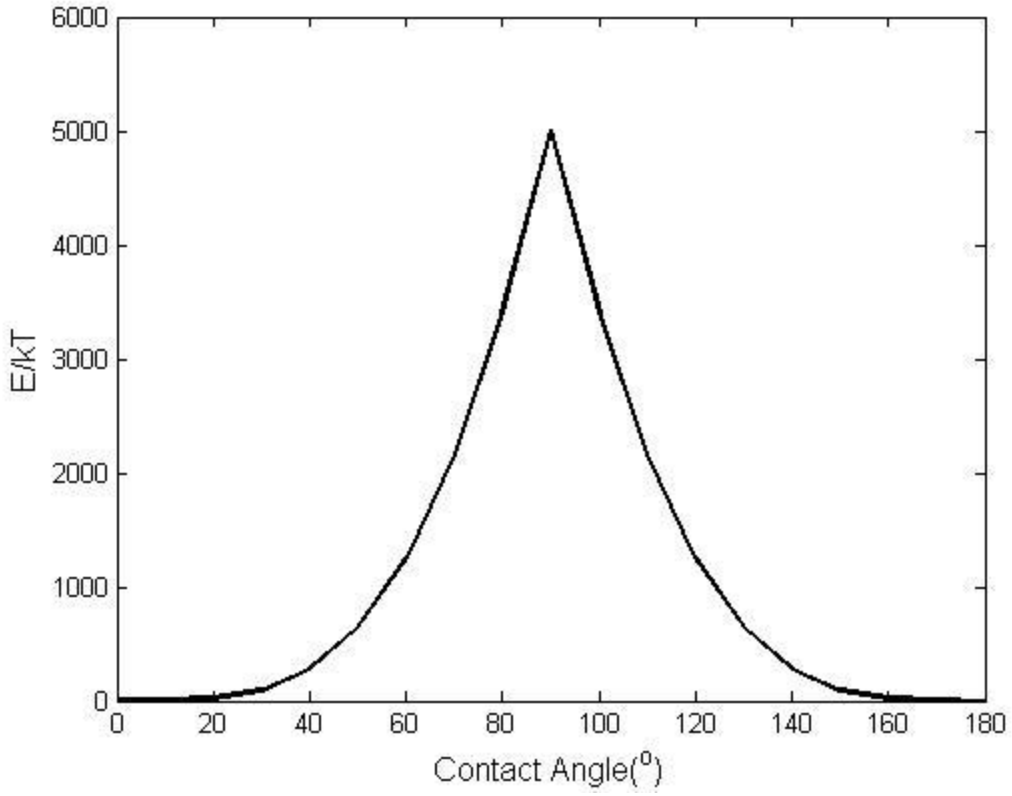

Figure 2.3: Attachment energy (E) of a spherical particle (r = 14 nm) at the planar n-octane-water interface as a function of contact angle.

Therefore, if the particle is too water-wet or too oil-wet, the adsorption energy becomes relatively small compared with the thermal energy (< 10kT) and the emulsion exhibits low stability. If the contact angle is assumed to be 60°, then the adsorption energy as a function of nanoparticle size can be plotted as shown in Figure 2.4.

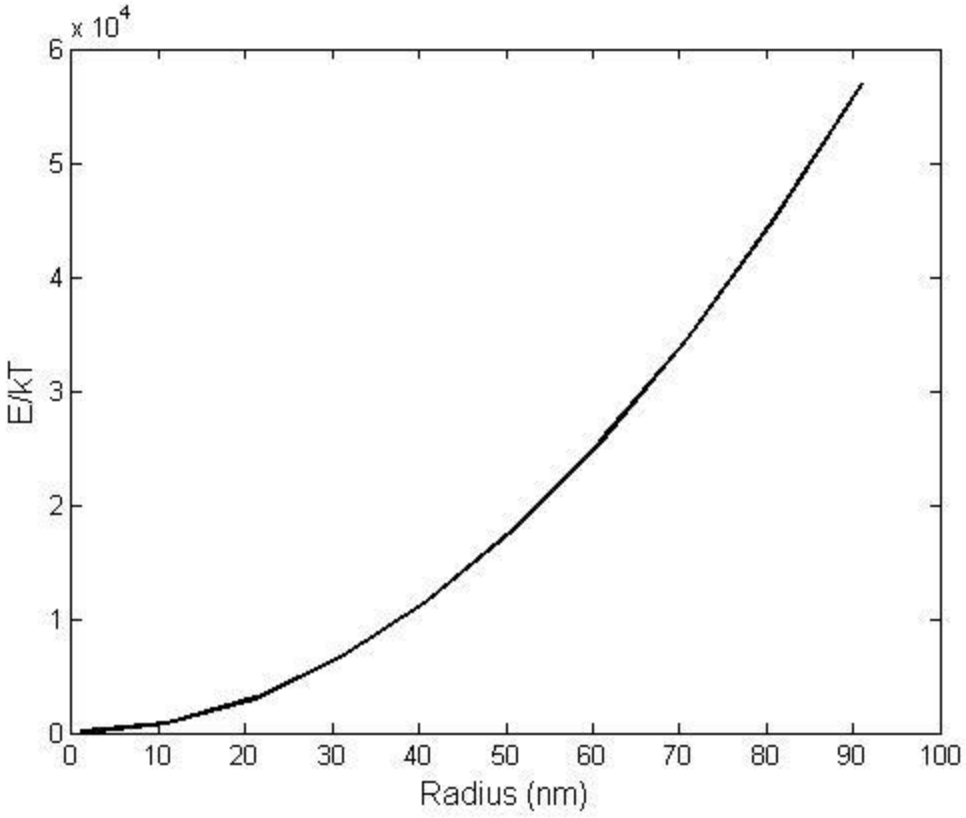

Figure 2.4: Attachment energy (E) of a spherical particle (θ = 60°) at the planar n-octane-water interface as a function of particle radius.

Figure 2.4 shows that the adsorption energy grows quadratically with particle radius. Therefore, it would be easier to stabilize oil-in-water emulsion using particles of nano-size than micro-size. However, nanoparticle-stabilized emulsions are more sensitive to thermal fluctuations than "microparticle"-stabilized ones. The smallest particles used for experiments in this thesis have a diameter of 5 nm and the calculated adsorption energy is 43 kT, indicating that emulsions stabilized by the 5-nm particles are still immune from thermal fluctuations.

Nanoparticle-Stabilized Emulsion in Porous Media

If nanoparticles were to stabilize emulsions of two immiscible phases within a porous medium, there has to be enough energy to bring the particles to the interface. Recent works by Espinosa (2011) and Roberts (2011) have shown that co-injection of two immiscible fluids at a high flow velocity provides enough mixing and shear rate to generate stable foam and emulsions. They found that there is a critical shear rate below which stable emulsions cannot be generated. Espinosa (2011) found this critical shear rate to be around 2,750 s^{-1} for co-injection of supercritical CO_2 and brine containing PEG-coated nanoparticles at 75℃ and 1350 psi. Roberts (2011) carried out an analog experiment with decane at room temperature and pressure and found the critical shear rate to be about 8,000 s^{-1}.

However, far from an injection site, shear rates on the order of 1,000 s^{-1} are hard to achieve. Furthermore, the more likely scenario for fluid flow in reservoir rocks would be displacement. Displacement can be categorized as either drainage or imbibition. During drainage displacement, non-wetting phase displaces wetting phase initially saturating the porous medium. Conversely, during imbibition displacement, wetting phase displaces non-wetting phase initially saturating the porous medium. During drainage displacement, it is well known that non-wetting phase invades a pore throat until the interface attains a critical curvature. At this point any more advancement of the non-wetting phase disrupts the configurational stability of the interface and the non-wetting phase "jumps" to the next available pore, a process known as Haines jump (Haines, 1927; Melrose, 1965). Roof (1970) showed that during Haines jump, a temporary decrease in local pressure drop creates disconnected droplets of the non-wetting phase. As more and more droplets invade the pore, the droplets coalesce and the non-wetting phase fills up the pore. An illustration of this mechanism is shown in Figure 2.5. Whether non-wetting

phase will jump to the pore space as a bulk phase or as droplets depends on the geometry of the pore network; Roof snap-off is most likely to occur in smoothly constricted pores that have a small throat to body ratio (Kovscek et al., 2007).

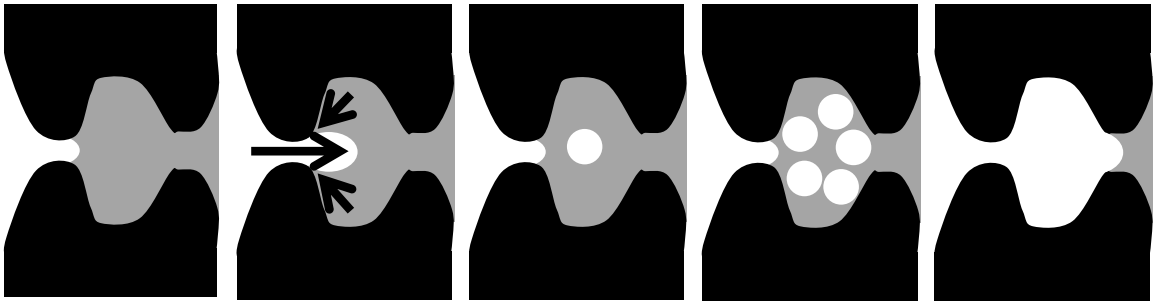

Figure 2.5: Schematic of snap-off in a single-constricted channel during drainage displacement without nanoparticles. White color indicates the invading non-wetting phase and grey color is the resident wetting phase.

If there are nanoparticles present in the wetting phase initially residing in the pore space in Figure 2.5, it is hypothesized that Roof snap-off provides the necessary adsorption energy to bring nanoparticles to the interface. The nanoparticles armor the droplets of the non-wetting phase and prevent them from coalescing and as a result, emulsion is stabilized as shown in Figure 2.6. Because these droplets form inside the bulk wetting phase, they move with the wetting-phase until they get stuck in a pore throat or crevice smaller than the droplet size.

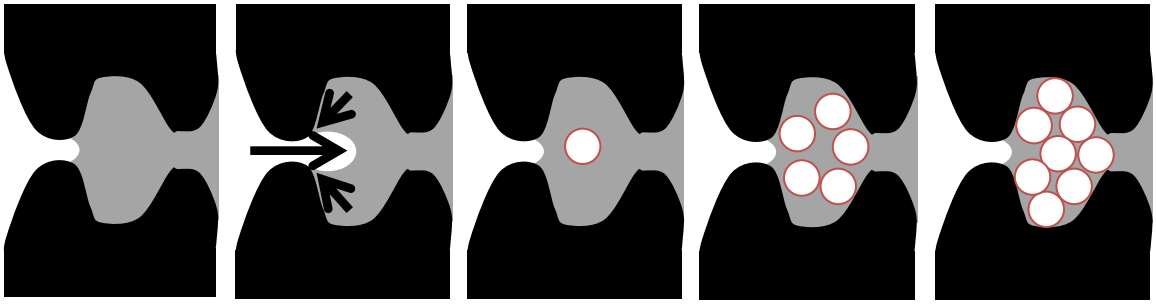

Figure 2.6: Schematic of snap-off in a single-constricted channel during drainage displacement with nanoparticles. White color indicates the invading non-wetting phase and grey color is the resident wetting phase. Droplets of the non-wetting phase are armored by nanoparticles (red).

Similar jumps also occur during imbibition displacement. As the wetting phase saturation increases, instability occurs when the advancing interfaces comes in contact with another interface. This instability induces the wetting phase to jump to the next stable position (Melrose, 1965). However, during this process, disconnected non-wetting phase is left behind as residual phase in pore spaces and does not move. Therefore, even if similar snap-off mechanisms stabilize nanoparticle-armored droplets of non-wetting phase during imbibition displacement, the droplets reside as disconnected phase in the same pore space that would be otherwise occupied by residual non-wetting phase. In other words during imbibition there is no practical difference between the two situations with and without nanoparticles.

Therefore, in order for nanoparticle-stabilized emulsions to have an impact on the displacement dynamics, it is hypothesized that not only do droplets need to form, but the generated emulsions must also disrupt the flow path of the displacement. During drainage, the stabilized droplets disrupt the flow path by pore blocking while the stabilized droplets yield the same flow patterns during imbibition displacement as unstabilized but disconnected droplets. This hypothesis will be tested during experimentations presented in Chapter 3 and Chapter 4.

Effect of Nanoparticles on Displacement Dynamics

One of the experimental results that support the proposed hypothesis is done by Aminzadeh (Aminzadeh, 2013; DiCarlo et al., 2011). Drainage experiment was done with n-octane invading a core initially saturated with 2 wt% sodium bromide (NaBr) brine (control experiment) or 2 wt% NaBr brine containing 10 wt% nanoparticles (nanoparticle experiment). During the experiment, the internal dynamics of the displacement was monitored with a modified medical CT scanner. The experimental set-up is shown in Figure 2.7.

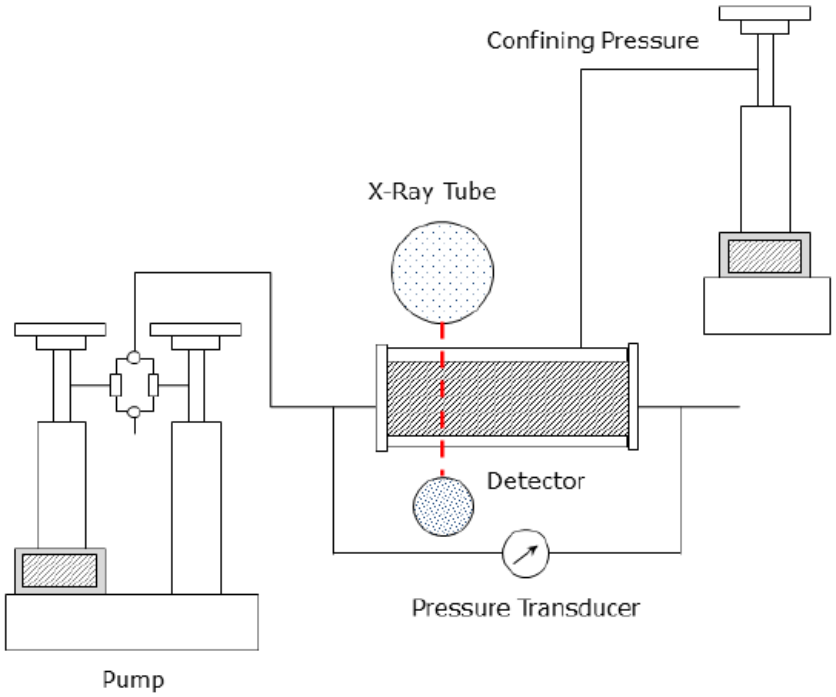

Figure 2.7: Schematic of the core flooding set-up by Aminzadeh (2013).

Figure 2.8 shows CT scans of the core after 0.1 PV of n-octane was injected to displace 2 wt% NaCl with and without nanoparticles (DiCarlo et al., 2011). From left to right the scans show slices of the core imaged at 0.30 mm resolution, starting at a

distance of 2 cm from the inlet and at equal intervals of 1 cm. 100% brine saturation is red, 100% n-octane is blue. If 0.1 PV of injected n-octane invades all available pore space, the first three slices (#1-#3) should be all blue. Compared to the control case, the scans from nanoparticle experiment show much less lateral variations of n-octane saturations (less extreme blue or red) and less fingering. Comparing the two sets of images after the same PV injected, the control image shows a sign of viscous fingering at 5 o'clock position in the last slice (#9) while the nanoparticle image indicates n-octane has not arrived to the same position yet. The inferred presence of fluid of density intermediate to that of brine and of n-octane from the CT image in Figure 2.8 (intermediate density is shown as green color) also suggests that emulsions that are generated in-situ inside the core. If emulsions are generated, the pressure drop across the core should be higher as emulsions are more viscous than two pure phases. However, the pressure drop across the core was not measured during this experiment. Drainage displacement experiment with pressure drop measurement is presented in Chapter 3 along with more detailed discussion.

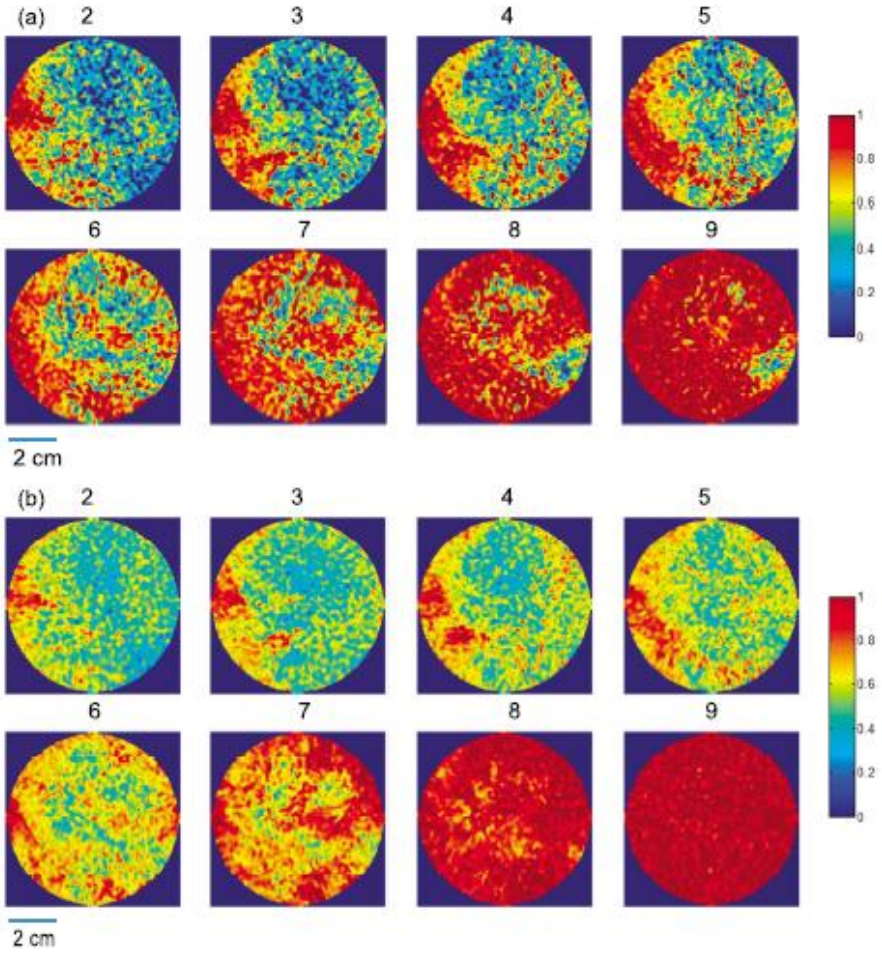

Figure 2.8: CT scans for n-octane injection into Boise sandstone core (1" diameter, 1 foot long) initially filled with a) 2 wt% brine and b) 2 wt% brine with 10 wt% nanoparticles, each after injection of 0.1 PV (DiCarlo et al., 2011).

2.2 NANOPARTICLE TRANSPORT IN SINGLE PHASE FLOW

Nanoparticle transport in porous medium has been of special interest to scientists and engineers as commercialized nanoparticles are bound to find their way into the environment. As a result, a risk assessment of the potential migration of nanoparticles in the porous media, such as groundwater aquifers has become a subject of prime importance. In oil field applications, the decision to deploy nanoparticles for EOR or CO_2 sequestration will depend strongly on their ability to flow through porous media. During flow in porous media, nanoparticles come in contact with immobile surface followed by attachment, or adsorption (O'Melia, 1989). The Happel model (Happel, 1958) predicts that particles may cross a critical region due to the effects of gravity and Brownian motion. For nanoparticles, Brownian motion is more likely to be the driving force of adsorption.

Leocoanet et al., 2004 performed systematic nanoparticle transport experiments to assess their mobility in water-saturated glass-bead columns. They demonstrated that depending on their material, coating, and size, nanoparticles exhibit widely differing transport behaviors. Figure 2.9 shows experimental results from Leocoanet et al.

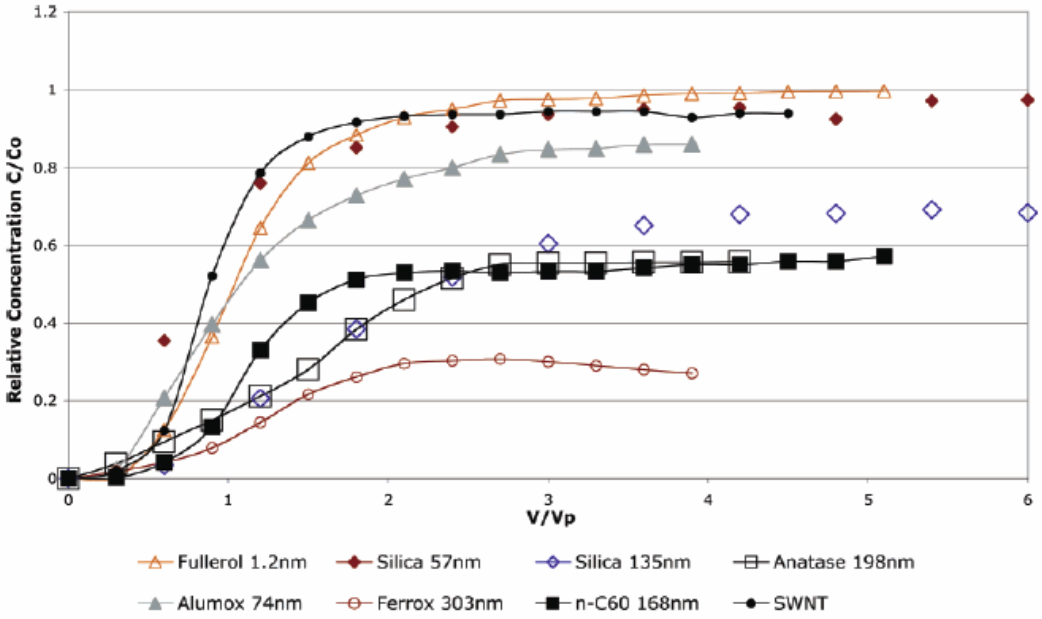

Figure 2.9: Normalized concentrations of different nanoparticle dispersions as a function of pore volume (PV) under the same physical and chemical conditions (Leocoanet et al., 2004).

One interesting grouping of the experimental results in Figure 2.9 can be done by the size of particles. Nanoparticles that exhibit relatively faster breakthrough curve (grey alumox curve and above) have a diameter less than 100 nm. The smaller silica nanoparticles exhibited less adsorption than the bigger silica nanoparticles.

More recent works by Caldelas (2010), Murphy (2012), and Yu (2012) offer hundreds of nanoparticle flow experiments through porous media. Some of the experimental observations are: 1) Nanoparticle retention is larger for larger injected concentration (Murphy, 2012). 2) In a porous medium with a fixed retention capacity, the effluent concentration eventually reaches the injected concentration (Murphy, 2012). 3) Higher flow rates generally lead to lower permanent nanoparticle retention (Yu, 2012). 4) Surface coatings attached to the nanoparticle core for dispersion stability does not

guarantee high transportability of nanoparticles; some of the coatings can wear away during transport through porous media (Yu, 2012).

Zhang (2012) developed a number of different nanoparticle transport models to fit this library of flow experiments. The models include colloidal filtration model, kinetic Langmuir adsorption model, two-step model, two-site model and two-rate model. History matching these models to experimental data shows that the two-site model is the best matching model. The two-site model assumes that adsorption sites can be categorized as irreversible or reversible, depending on their geometry. Nanoparticles that were attached to reversible adsorption sites are available for removal by Brownian motion or potential gradient while those found their place in irreversible adsorption sites are permanently retained on the rock surface. Therefore, the mathematical expressions for this model are:

$$\frac{\partial c}{\partial t} + \frac{\rho_b}{\phi}\frac{\partial s}{\partial t} = D\frac{\partial^2 c}{\partial x^2} - v_p\frac{\partial c}{\partial x}$$

$$\frac{\rho_b}{\phi}\frac{\partial s}{\partial t} = \frac{\rho_b}{\phi}\frac{\partial s_1}{\partial t} + \frac{\rho_b}{\phi}\frac{\partial s_2}{\partial t}$$

$$\frac{\rho_b}{\phi}\frac{\partial s_1}{\partial t} = k_{irr}\left(1 - \frac{s_1}{s_{1max}}\right)c$$

$$\frac{\rho_b}{\phi}\frac{\partial s_2}{\partial t} = k_{ra}\left(1 - \frac{s_2}{s_{2max}}\right)c - \frac{\rho_b}{\phi}k_{rd}s_2$$

The first equation is a convective dispersion equation with an adsorption term. c is concentration, t is time, ρ_b is bulk density, ϕ is porosity, s is the concentration of nanoparticles attached to reversible and irreversible sites, D is diffusion coefficient, x is distance, and v_p is interstitial velocity. The second equation states that there are two different sites for nanoparticle adsorption. s_1 is the nanoparticle concentration on solid

surface for irreversible adsorption and s_2 is for reversible adsorption. The third equation describes the irreversible adsorption process that is proportional to the irreversible adsorption rate coefficient, k_{irr} and the nanoparticle concentration. Adsorption continues until the irreversible site capacity, s_{1max}, is filled. The last equation describes the reversible adsorption and desorption process. The adsorption process is the same as the irreversible adsorption process with reversible adsorption rate coefficient, k_{ra}, and the reversible site capacity, s_{2max}. The desorption process is proportional to the desorption rate coefficient and the nanoparticle concentration that is adsorbed on the reversible site, s_2. In dimensionless form, the equation becomes:

$$\frac{\partial c_D}{\partial t_D} + M_1 \frac{\partial s_{1D}}{\partial t_D} + M_2 \frac{\partial s_{2D}}{\partial t_D} = \frac{1}{N_p} \frac{\partial^2 c_D}{\partial x_D^2} - \frac{\partial c_D}{\partial x_D}$$

$$M_1 \frac{\partial s_{1D}}{\partial t_D} = M_3 (1 - s_{1D}) c_D$$

$$M_2 \frac{\partial s_{2D}}{\partial t_D} = M_4 (1 - s_{2D}) c_D - M_5 s_{2D}$$

where the dimensionless variables and groups are defined as:

$$c_D = \frac{c}{c_0} \quad , \quad s_{1D} = \frac{s_1}{s_{1max}} \quad , \quad s_{2D} = \frac{s_2}{s_{2max}}$$

$$M_1 = \frac{\rho_b}{\phi} \frac{s_{1max}}{c_0} \quad , \quad M_2 = \frac{\rho_b}{\phi} \frac{s_{2max}}{c_0} \quad , \quad M_3 = k_{irr} \frac{l}{v_p}$$

$$M_4 = k_{ra} \frac{l}{v_p} \quad , \quad M_5 = \frac{\rho_b}{\phi} \frac{s_{2max}}{c_0} \frac{l}{v_p} k_{rd} \quad , \quad N_p = \frac{v_p l}{D}$$

where *l* is the length of the porous medium.

The equations are solved using an implicit finite difference method with the following initial and boundary conditions:

$$\text{I.C.:} \quad c(x,0) = 0 \;\; , \;\; s(x,0) = 0 \;\; , \;\; 0 \le x \le l$$

$$\text{B.C. 1:} \quad c(0,t) = \begin{cases} c_0 \;\; , & 0 \le t \le t_s \\ 0 \;\; , & t > t_s \end{cases}$$

$$\text{B.C. 2:} \quad \left.\frac{\partial c}{\partial x}\right|_{x=l} = 0 \;\; , \;\; t \ge 0$$

where c_0 is the injected concentration and t_s is the pore volume of nanoparticle dispersion injected. . Figure 2.10 through Figure 2.13 show select experimental results from Murphy (2012) with two-site model fit from Zhang (2012)'s work.

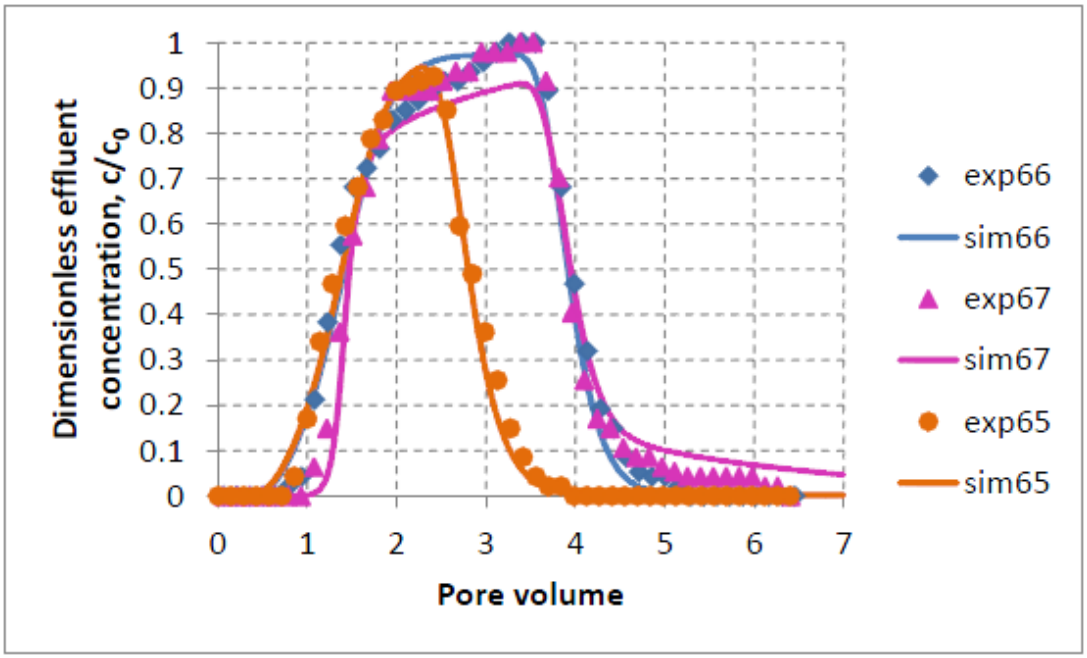

Figure 2.10: Experimental (points) and simulated (curves) effluent curves by the two-site model for salt-tolerant silica nanoparticle (Zhang, 2012).

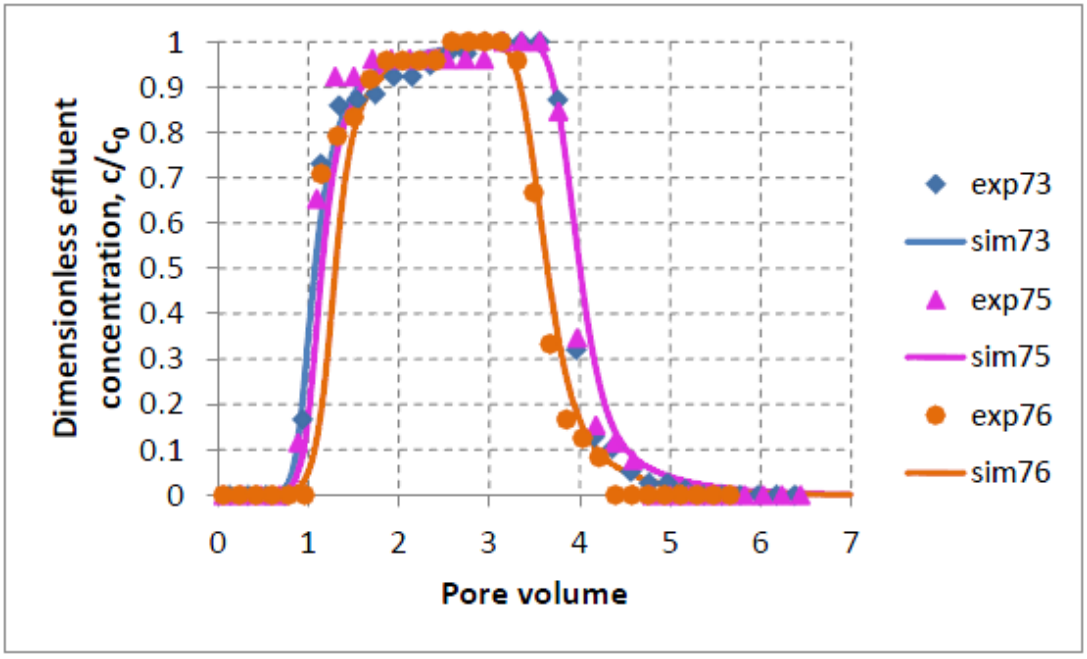

Figure 2.11: Experimental (points) and simulated (curves) effluent curves by the two-site model for Nyacol DP nanoparticle (Zhang, 2012).

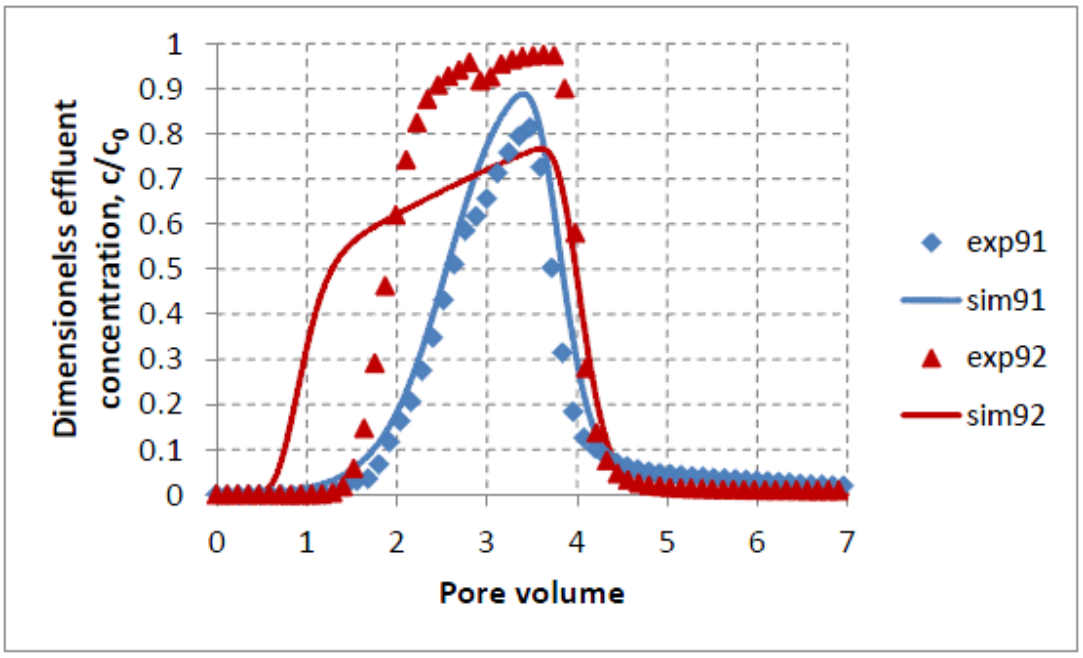

Figure 2.12: Experimental (points) and simulated (curves) effluent curves by the two-site model for iron oxide nanoparticle (Zhang, 2012).

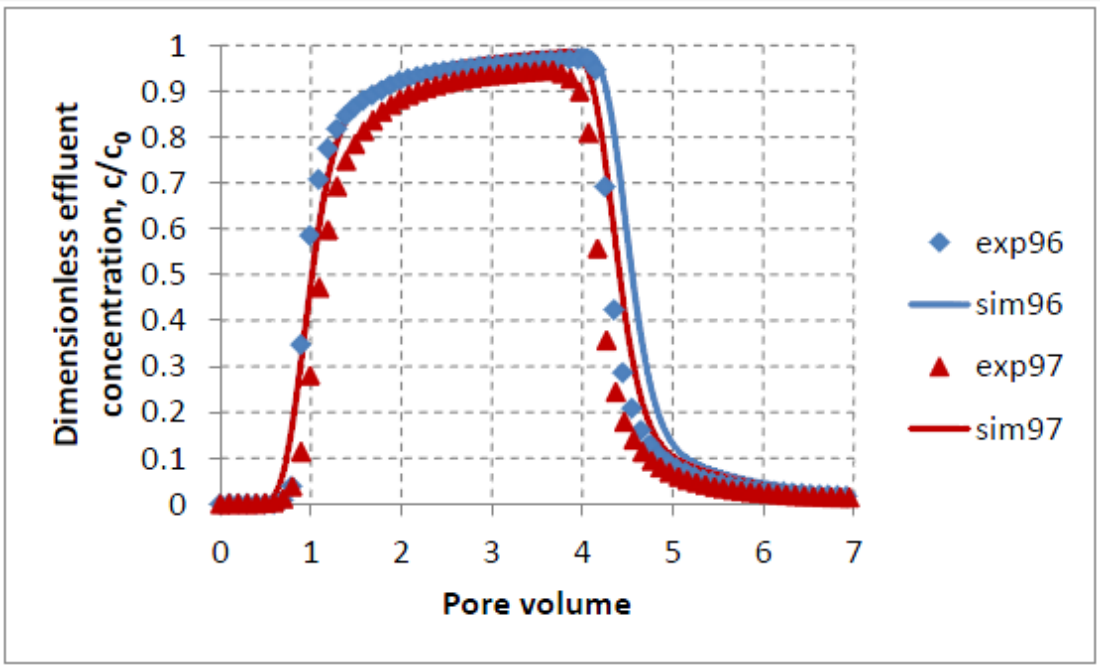

Figure 2.13: Experimental (points) and simulated (curves) effluent curves by the two-site model for fluorescent silica nanoparticle (Zhang, 2012).

It is interesting to note that there is a similar nanoparticle size effect that we saw in Leocoanet, 2004. In Murphy and Zhang's experiments, the salt-tolerant silica nanoparticles had a diameter of 15 nm, Nyacol DP nanoparticles 27 nm, and fluorescent silica nanoparticle 10 nm while the iron oxide nanoparticles had a diameter ranging from 108 nm to 150 nm depending on the coating type. Clearly, there is a higher retention for the bigger iron oxide nanoparticles. Of the three nanoparticles that showed little affinity to adsorption, Nyacol's DP silica nanoparticles seem to suffer least from adsorption as the normalized concentration of these nanoparticles reaches unity fastest. Furthermore, Nyacol DP nanoparticles' ability to stabilize high-quality oil-in-water emulsions made it stand out as the preferred nanoparticle for experimentations in this thesis.

Chapter 3

Drainage Displacement

3.1 MOTIVATION

One of the key concerns for subsurface CO_2 storage is that CO_2 is less dense and less viscous than in-situ brine. Instability arises from viscosity contrast between the two fluids and the resulting viscous fingering leads to a poor sweep efficiency of CO_2 injection within the storage formation. Buoyant force resulting from density difference between CO_2 and brine presents the possibility for sequestered CO_2 to rise through relatively thin paths in the geologic strata and be emitted back into the atmosphere. In an effort to prevent such failure, this project aims to engineer the sequestration in such a way that any potential leaks would be self-sealing. An analogy is "run flat" tires in the automobile industry in which the first pulse of escaping gas in a punctured tire induces a chemical reaction that seals the leak.

One potential way to implement this preventive measure is to use chemically coated nanoparticles to stabilize foam of supercritical CO_2 in brine. The nanoparticle-stabilized foams (or emulsions if CO_2 is in liquid phase) are less mobile than the separate pure phases. As illustrated in Figure 3.1, these nanoparticles can be pre-injected into locations where risk of leakage is expected to be greatest. If sequestered CO_2 were to rise through the nanoparticle treated rock, nanoparticles will be attracted to the CO_2-brine interface and immobilize the escaping CO_2 by forming CO_2-in-brine foam. This study investigates whether such a hypothesized mechanism takes place by performing core floods where n-octane displaces brine with and without nanoparticles. The core flood experiments presented in this thesis are carried out with n-octane, which is a convenient analog to liquid CO_2 phase as discussed in the next section.

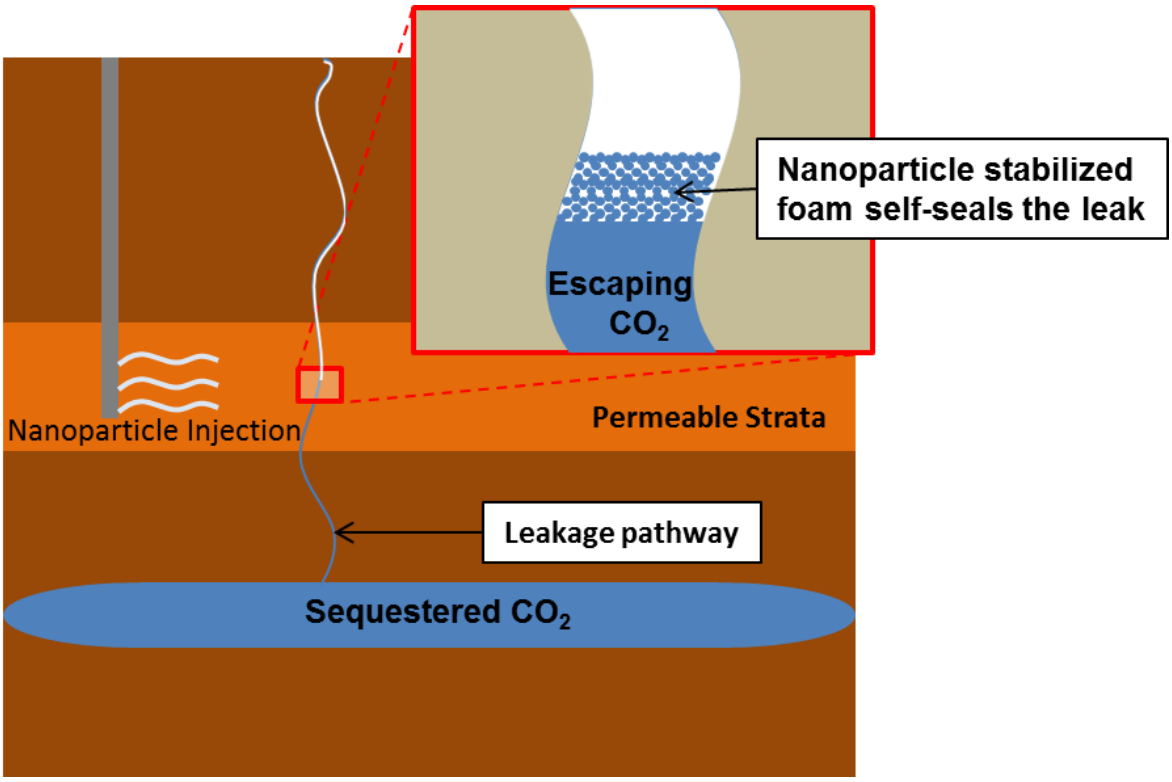

Figure 3.1: Schematic of a self-sealing CO_2 storage site.

3.2 ANALOGIES BETWEEN N-OCTANE AND SUPERCRITICAL CO_2

In all of the experiments done for this study, n-octane is used as a low pressure surrogate fluid to supercritical CO_2 as it mimics the key features of supercritical CO_2:

1. Both fluids form nanoparticle stabilized droplets in brine.
2. Both fluids act as the non-wetting phase in the sandstone.
3. Both fluids are condensed phases and have roughly the same density.
4. Both fluids give displacements that are capillary dominated at the pore scale.
5. Both fluids are less viscous than brine.

The relevant fluid parameters are listed in Table 3.1. "5 wt% NP" indicates the weight concentrations of nanoparticles suspended in brine. The types and details of nanoparticles used are described in each of the experimental materials and methods sections. The surface tensions for n-octane and CO_2 are reported with respect to brine. Capillary numbers *Ca* are calculated at a flow velocity of 0.02 cm/s. The supercritical CO_2 properties are at a temperature of 40℃ and a pressure of 10 MPa while all other properties are at room temperature and pressure.

	Brine	5 wt% NP	n-Octane	CO_2
$\mu\ (cP)$	1.1	1.5	0.54	0.046
$\rho\ (kg/m^3)$	1,010	1,040	703	685
σ (mN/m)	N/A	N/A	51	24
Ca (--)	N/A	N/A	2.1×10^{-6}	3.8×10^{-7}

Table 3.1: Relevant fluid properties for drainage displacement experiments (Vargaftik, 2005, DiCarlo et al., 2000; da Rocha et al., 1999).

3.3 EXPERIMENTAL MATERIALS AND METHODS

Drainage displacement is defined as a process where non-wetting phase displaces wetting phase in a porous media. In this experiment, the non-wetting phase is n-octane and the wetting phase initially saturating the porous medium is brine or brine containing nanoparticles. These experiments conducted here are low-pressure analogues of how CO_2 escapes through a permeable layer that is saturated with brine with and without nanoparticles. The goal is to determine whether the change in displacement dynamics in presence of nanoparticles will be able to slow down or even stop the advance of CO_2. This section describes the necessary materials and procedures for the drainage displacement experiments.

3.3.1 Materials

Ultrapure Type 1 water with a resistivity of 18.2 MΩ-cm was prepared by Thermo Scientific Barnstead E-Pure system. Nanoparticles (Nyacol DP9711) used for drainage experiment were received from Nyacol Nano Technologies, Inc. These particles consist of silica cores and trade-secret coating for dispersion stability and the diameter is 27 nm. They were received as dispersions of 20.1 wt% nanoparticle concentration in tap water. Sodium chloride (NaCl) and n-octane were purchased from FisherScientific and ACROS, respectively. The purity of NaCl is 99%, n-octane 97%. Two one-inch-diameter and one-foot-long cores were cut from a high-permeability, homogeneous Boise sandstone block.

3.3.2 Experiment Set-up and Procedure

Epoxy Core Preparation

An epoxy core is a cheap and fast alternative to using a standard core holder. However, its applications are limited to low-pressure experimental conditions (generally less than 100 psi). Two Boise sandstone epoxy cores were prepared using the preparation steps detailed in Appendix A1.

Vacuum Saturation

Before the core is used for an experiment, it has to be completely saturated with initial fluid. The set-up used to vacuum saturate the core is shown in Figure 3.2. First, the core is vacuumed to remove any fluid or liquid present in the core. A vacuum pump (Emerson model C63CXGZP-4780) applies a pressure of -3.3 psi. It is connected to a jar full of desiccants that will prevent any moisture from going into the vacuum pump. This process should continue for at least 12 hours. Once the core is completely evacuated, its dry weight is measured. Second, initial fluid is loaded into a glass column and the valve connection between the glass column and the core is opened to let the fluid imbibe into the vacuumed core. In the control case, the initial fluid is 1 wt% NaCl brine. In the nanoparticle experiment, the initial fluid is 5 wt% nanoparticles dispersed in 1 wt% NaCl brine. Vacuum may be applied to ensure that the core is completely saturated with the initial fluid. After the core is saturated, the wet weight of the core is measured. The dry and wet weight of the core can be used to calculate the porosity and pore volume (PV) of the core.

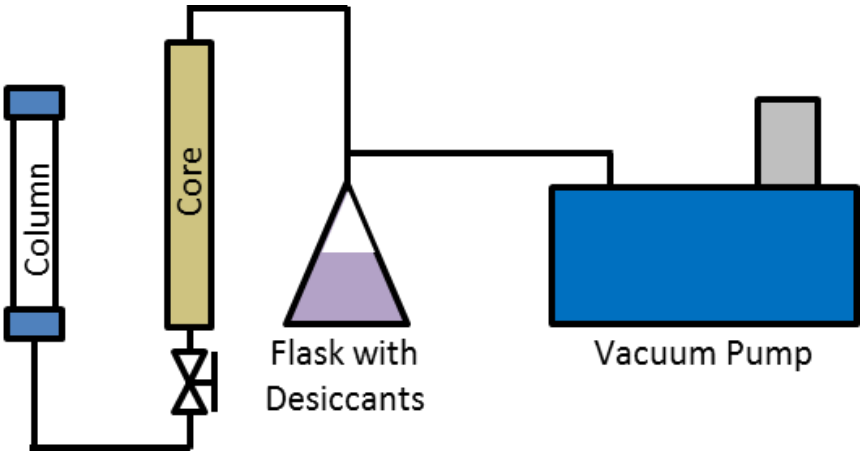

Figure 3.2: Schematics of the vacuum and saturation set-up.

Permeability Measurement

Figure 3.3 is a schematic of the coreflood system that was used to measure the permeability of the core. The set-up consists of a syringe pump (Teledyne ISCO model 1000D), two glass columns (Kontes Chromaflex), a pressure transducer (Rosemount), and a fraction collector (Teledyne ISCO Retriever 500). The procedure to measure the permeability of the core is as follows:

1. Mount epoxy molded core horizontally. Pressure transducer connects to the two ends of the core.
2. Mount two glass columns (Column A and Column B) vertically.
3. Fill Column A with mineral oil.
4. Fill Column B with sample to be injected into the core. In the control experiment, 1 wt% NaCl brine was used. In the nanoparticle experiment, 5 wt% nanoparticles dispersed in 1 wt% NaCl brine was loaded as sample.
5. Load syringe pump with ultrapure water.
6. Set up tubing connections as shown in Figure 3.3.

7. Start syringe pump. Water from the pump enters Column A from the bottom and displaces oil. The displaced oil enters Column B from the top and displaces sample into the core.
8. Record the pressure drop across the core measured by the pressure transducer using a LabVIEW program.
9. Check the flow rate and collect effluent samples using the fraction collector.
10. Values from three different flow rates were averaged to obtain permeability of the core.

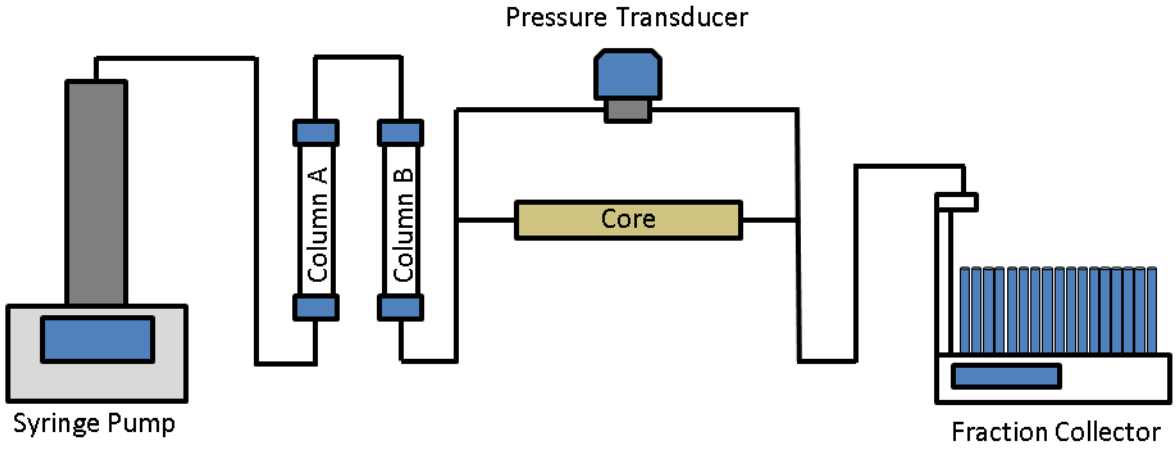

Figure 3.3: Schematics of the coreflood system for permeability measurement.

Drainage Experiment

Figure 3.4 is a schematic of the coreflood system that was used to carry out the drainage displacement experiment. The set-up is identical to the one used for permeability measurement except there is one less column. The procedure for drainage displacement experiment immediately follows permeability measurement and is as follows:

1. Remove and clean both glass columns from permeability measurement set-up shown in Figure 3.3.
2. Mount a column vertically.
3. Fill the column with n-octane.
4. Load syringe pump with water.
5. Set up tubing connections as shown in Figure 3.4.
6. Set the flow rate for 2 mL/min and start the syringe pump. Water from the pump enters the column from the bottom and displaces oil into the core.
7. Record the pressure drop across the core measured by the pressure transducer using a LabVIEW program.
8. Check the flow rate and collect effluent samples using fraction collector.

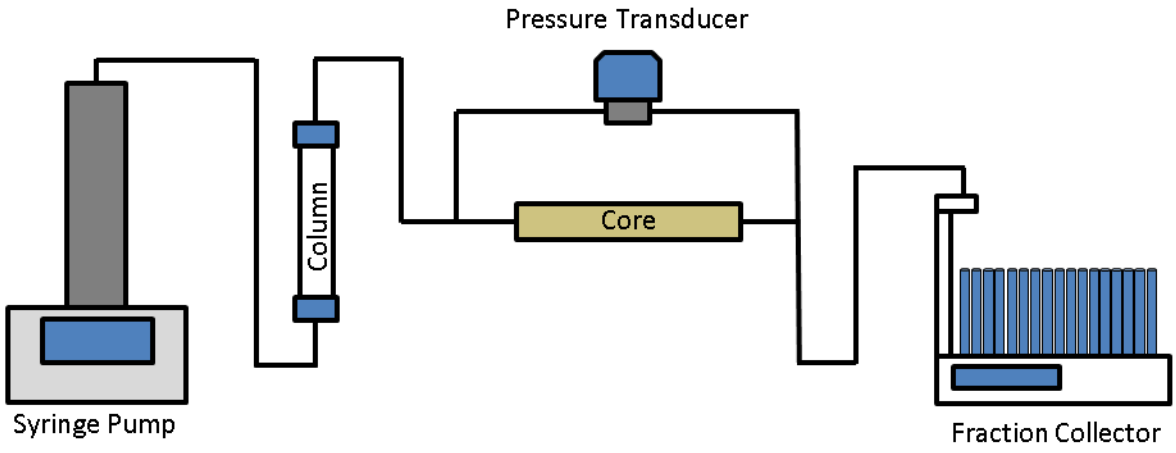

Figure 3.4: Schematic of the coreflood system for drainage displacement experiment.

A summary of experimental protocols and core properties are summarized in Table 3.2 and Table 3.3.

Exp. #	Resident Fluid	Invading Fluid	Flow Rate	Note
D1	1 wt% NaCl	n-octane	2 mL/min	Pressure Measurement
D2	1 wt% NaCl, 5 wt% NP	n-octane	2 mL/min	Pressure Measurement

Table 3.2: Experimental protocols for drainage displacement experiments.

Exp. #	Permeability	Porosity	Pore Volume	Dimensions
D1	1,300 mD	21%	33 mL	1" diameter, 1' length
D2	1,400 mD	19%	30 mL	1" diameter, 1' length

Table 3.3: Boise sandstone core properties for drainage displacement experiments.

3.4 RESULTS AND DISCUSSION

Experimental Results

Figure 3.5 shows the overall pressure drop as a function of time for Exp. D1 and Exp. D2.

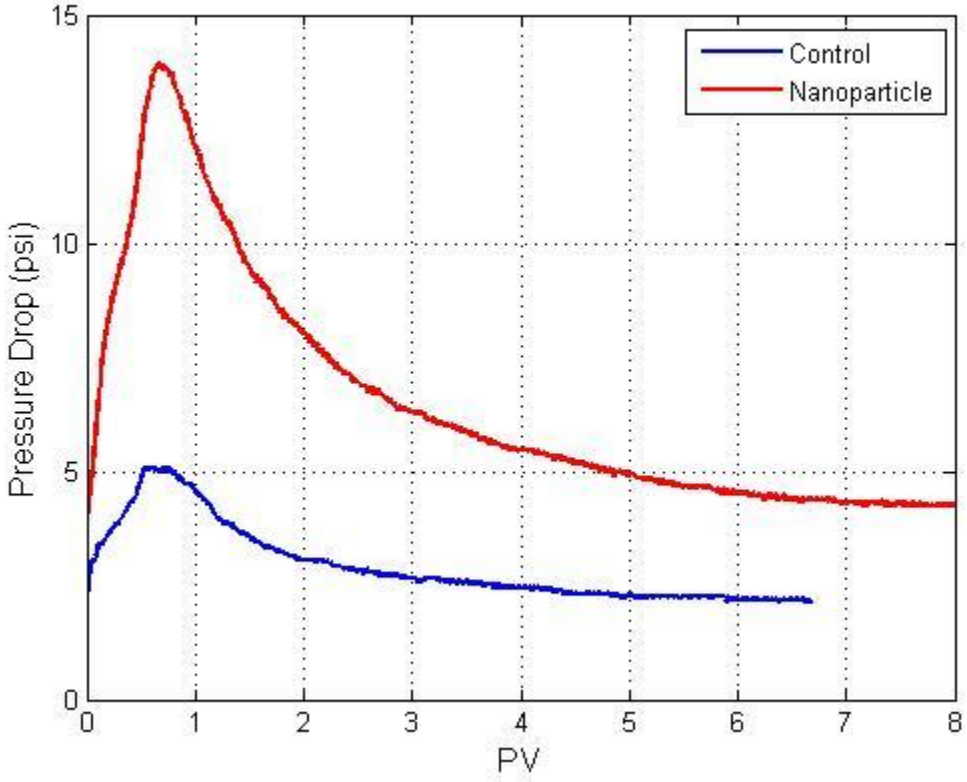

Figure 3.5: Measured pressure drop as a function of time for n-octane injection for the control case (Exp. D1; blue) and the nanoparticle case (Exp. D2; red).

Because two experiments were done with two different cores that have slightly different pore volumes and permeabilities, the pressure drop was normalized by the pressure drop of single-phase 1 wt% NaCl brine flowing at the same rate (2 mL/min) through the core for ease of comparison. For the control case, this pressure drop was 2.23

psi and for the nanoparticle case, 3.13 psi. The normalized pressure drop as a function of time is shown in Figure 3.6.

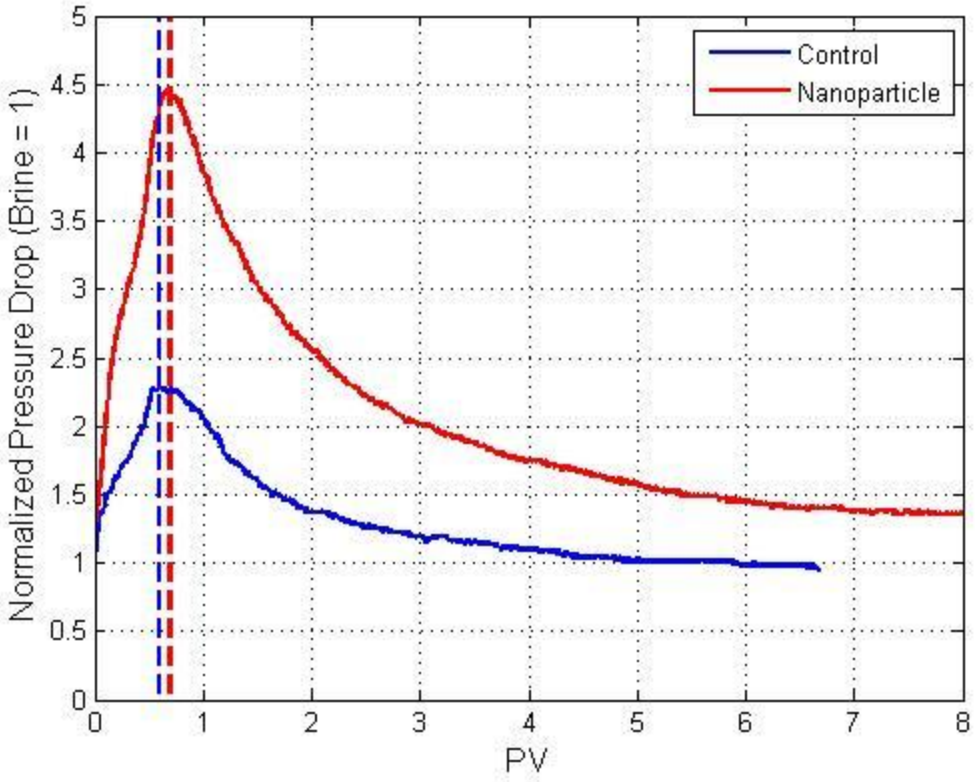

Figure 3.6: Normalized pressure drop as a function of time for n-octane injection for the control case (Exp. D1; blue) and the nanoparticle case (Exp. D2; red). The dashed line indicates the breakthrough time (blue for the control case, red for the nanoparticle case).

Both experiments in Figure 3.6 show a similar pattern where the pressure drop builds up across the core for the first 0.7 PV injected due to multi-phase flow. After less than one PV of injection, n-octane breaks through at the core outlet as indicated by the presence of n-octane in the effluent. After breakthrough, the pressure drop gradually decreases to a steady-state value corresponding to n-octane flow at residual brine saturation. However, the nanoparticle experiment shows a normalized pressure drop

consistently 1.3 to 2 times greater the control case throughout the experiment. In addition, during the nanoparticle experiment, small droplets of oil-in-water emulsion were observed in the effluent tubing traveling down to the fraction collector. However, their stability was very weak and they separated into pure phases before they reached the fraction collector.

The residual saturation of brine or brine containing nanoparticles was calculated by comparing the total volume of n-octane collected in the effluent samples and the pore volume of the core. The residual saturation for the control case was 31% and for the nanoparticle case 43% as summarized in Table 3.4.

	Control Exp. (Exp. D1)	Nanoparticle Exp. (Exp. D2)
Residual Saturation of Brine or Brine with Nanoparticles	31%	43%

Table 3.4: Residual saturation of brine or brine containing nanoparticles after the control (Exp. D1) and nanoparticle (Exp. D2) experiments.

Closely analogous experiments were reported by DiCarlo et al. (2011) where the internal dynamics of the displacement was observed with a modified medical CT scanner. Figure 3.7 shows CT scans of the core after 0.1 PV of n-octane was injected to displace 2 wt% NaBr with and without nanoparticles. From left to right the scans show slices of the 1" diameter core imaged at 0.30 mm resolution, starting at a distance of 2 cm from the inlet and at equal intervals of 1 cm. Full brine saturation is red, n-octane is blue. If 0.1 PV of injected n-octane invades all available pore space, the first three slices of the CT images should be all blue. Compared to the control case, the scans from the nanoparticle

experiment show much less lateral variations of n-octane saturations (less extreme blue or red) and less fingering. Comparing the two sets of images after the same PV injected, the control image shows a sign of viscous fingering at 5 o'clock position in the last slice (#9) while the nanoparticle image indicates n-octane has not arrived to the same position yet.

The presence of fluid of density intermediate to that of brine and of n-octane in the nanoparticle experiment CT image (displayed as green in Figure 3.7) also suggests the possible presence of emulsions generated in-situ during drainage displacement.

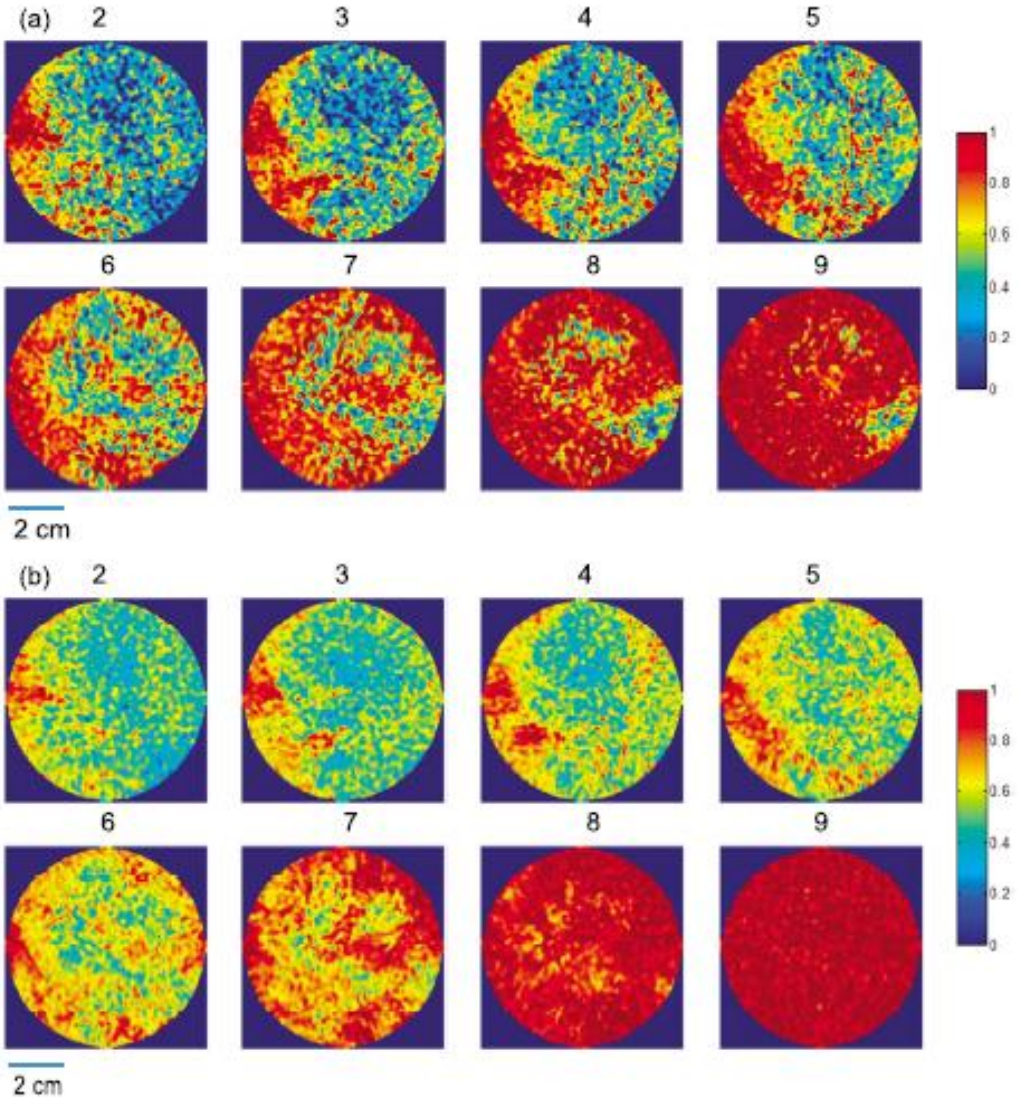

Figure 3.7: CT scans for n-octane injection into Boise sandstone core (1" diameter, 1 foot long) initially filled with a) 2 wt% brine and b) 2 wt% brine with 10 wt% nanoparticles, each after injection of 0.1 PV (DiCarlo et al., 2011).

Generation of Nanoparticle-Stabilized Emulsions during Drainage Displacement

As reviewed in Chapter 2, nanoparticles are believed to form an armor-like coating around disconnected droplets of non-wetting phase to stabilize the droplets during Roof snap-offs of advancing non-wetting phase. Although there is a debate, some researchers have argued that Roof snap-off is the main mechanism for generating CO_2-in-water foam in porous media (Kovscek et al., 2007). Since emulsions and foam are analogous in having disconnected droplets or bubbles, respectively, inside a bulk continuous phase, the same mechanism is likely to be responsible for generating nanoparticle-stabilized oil-in-water emulsion during displacement flow. In the following, we offer a discussion of the experimental results through the formation of nanoparticle-stabilized emulsions at the main displacement front.

Discussion

Compared to the control case, the nanoparticle experimental results show a higher pressure drop, less fingering, and larger residual water saturation. All of these observations are associated with stabilization of the displacement front. The displacement front can be stabilized by reducing the mobility of the invading phase. Mobility is a ratio of effective permeability to phase viscosity and is defined as:

$$\lambda = \frac{K k_r}{\mu}$$

where K is absolute permeability, k_r is relative permeability, and μ is viscosity. The mobility reduction factor of the flowing fluid(s) with and without nanoparticle can be inferred from the pressure drop ratio between the two graphs in Figure 3.6. Figure 3.8 shows the mobility reduction factor calculated by dividing the pressure drop of the

nanoparticle experiment by that of the control experiment. During the early part of the experiments (until about 0.6 PV injected) multiple fluid phases are flowing, including brine, n-octane and possibly emulsion, and the mobility reduction factor lumps the multiphase flow into an equivalent (in terms of pressure drop) single phase. As n-octane injection continues, the aqueous phase flow stops at residual aqueous phase saturation and the mobility reduction factor applies to the n-octane phase.

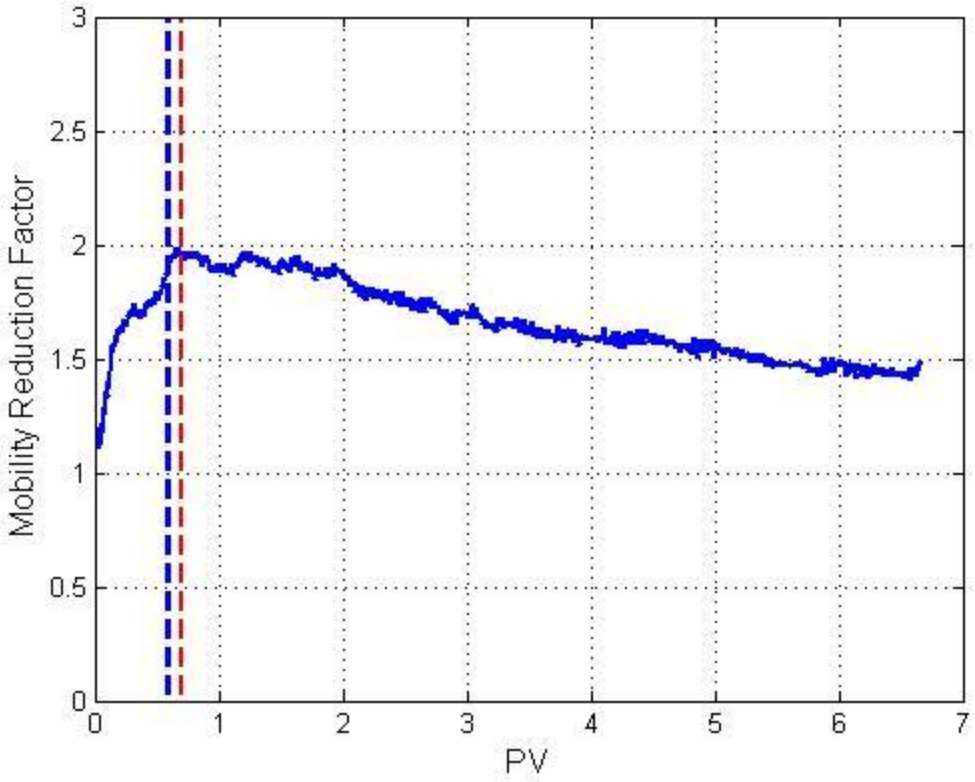

Figure 3.8: Mobility reduction factor inferred from the ratio of the normalized pressure drop of the nanoparticle experiment (Exp. D2) to that of the control experiment (Exp. D1). The dashed line indicates the breakthrough time (blue for the control case, red for the nanoparticle case).

Figure 3.8 shows that the mobility reduction factor ranges from 1.1 to 2. The mobility reduction factor is largest at breakthrough and gradually decreases after

breakthrough. Since it is hypothesized that mobility reduction is caused by Haines jump and oil droplet stabilization during pore-scale displacement, mobility reduction factor should be greatest when Haines jumps are the most prevalent pore-scale event. Haines jump into a pore requires a wetting phase to be present in the pore. Therefore, Haines jump will occur most actively at the main displacement front where the contact area between the wetting phase and the non-wetting phase is greatest. The main displacement front moves along the core, stabilizing more droplets and increasing the mobility reduction factor to its maximum of 2 until breakthrough when the main displacement front exits the core. Coincidentally, this mobility reduction factor of 2 is equivalent to the viscosity ratio between brine and n-octane (2.04). As a result, displacement is stabilized and viscous fingering is less prominent at the displacement front as pointed out in Figure 3.7.

In a viscously unstable displacement, pore-scale displacement continues and stabilizes droplets behind the main displacement front but these droplet stabilization events occur at a much smaller frequency. As the brine saturation inside the core decreases, the relative permeability of n-octane slowly increases, resulting in a gradual decrease in the pressure drop after breakthrough as shown in Figure 3.6. Far behind the front, brine is at its residual saturation and only n-octane flows through the core. Consequently, the pressure drop is stabilized for n-octane flow at residual brine saturation as shown in Figure 3.6. The continuous decrease in the mobility reduction factor suggests that some of the stabilized droplets were leaving the core; this argument is supported by observations of droplets in the effluent line. However, the observed droplets were unstable and broke before they reached the fraction collector. It is also possible that the mobility reduction factor decreases because emulsions broke and came out of the core as less-viscous pure phases.

Generation of in-situ emulsion can reduce the mobility in two ways. The first is a reduction in effective permeability due to pore blocking. The second is by an increase in viscosity as a result of emulsion formation and flow. The extent of pore blocking can be evaluated by the reduction in the end point relative permeabilities of the invading phase during the nanoparticle and control experiments. The end point relative permeability of n-octane at residual brine saturation can be calculated by

$$k_{ro}^{o} = \frac{\mu_o}{\mu_w}\frac{\Delta P_w}{\Delta P_o}$$

where k_{ro}^{o} is the relative permeability of n-octane, μ_o and μ_w are viscosities of n-octane and brine, respectively, ΔP_w is pressure drop from single-phase brine flow at a constant flow rate q_w and ΔP_o is pressure drop from n-octane flow at residual brine saturation at constant flow rate $q_o = q_w$. For the control experiment, the equilibrium pressure drop is 0.95 of the single-phase brine flow. Using the viscosities in Table 3.1, the calculated end point relative permeability of n-octane for the control experiment is 0.52.

For the nanoparticle experiment, the pressure drop for the nanoparticles case is 1.3 to 2 times greater than that seen in the control case throughout the injection period. This difference in pressure drop is not due solely to the viscosity contrast between brine and nanoparticle dispersion. Figure 3.9 shows the viscosity of 5 wt% Nyacol DP9711 nanoparticle dispersions as a function of shear rate. Assuming that the mixture of n-octane, brine, and emulsion acts like a non-Newtonian fluid, shear rate in porous media can be estimated by:

$$\gamma = \frac{4q}{A\sqrt{8k\phi}}$$

where q is volumetric flow rate, A cross-sectional area of the porous medium, k single-phase permeability and ϕ porosity (Lake, 1989). In the experimental condition tested in this study, the shear rate is about 85 s^{-1}. At this shear rate, the viscosity of 5 wt% nanoparticle dispersion is about 1.5 cP compared to 1.1 cP for brine. Thus, during the portion of the displacement when the aqueous phase (brine or nanoparticle dispersions) is flowing, we would expected the normalized pressure to be a factor of 1.5/1.1 = 1.36 greater when the aqueous phase is the nanoparticle dispersion. As shown in Figure 3.8, the ratio of normalized pressure drop exceeds this value for nearly the entire displacement.

For the nanoparticle experiment, the steady-state pressure drop is 1.36 times the pressure drop for single-phase brine flow. Using these values and the formula above, the end point relative permeability of n-octane at residual water saturation when nanoparticles are present is 0.36. As discussed in Chapter 5, there is substantial evidence that the viscosity of a nanoparticle dispersion flowing through a sedimentary rock is smaller than the viscosity measured in a rheometer at the same shear rate. Thus the value of the endpoint relative permeability is likely to be smaller than 0.36. In any case, the presence of nanoparticles in the brine clearly reduced the end point relative permeability from its value of 0.52 in the control experiment.

Also, emulsions are highly shear-thinning and are two orders of magnitude more viscous than n-octane in the shear rate range used for this experiment, i.e. 85 s^{-1}, as shown in Figure 3.10. As a result, any stable emulsions that were generated during drainage displacement are likely to become trapped in the core as n-octane flows past them; confirming thise expectation, no visual evidence of produced stable emulsions can be observed at the outlet. Another possible indication of in-situ generation of nanoparticle-stabilized emulsions is a higher residual water saturation of 43% after the

nanoparticle experiment compared to the control experiment's 31%; the difference of 12 percentage points could be remaining as oil-in-water emulsions stuck in small pore throats and crevices that hinder flow of n-octane but would be accessible to n-octane flow in the control experiment. Therefore, the reduction in the end point relative permeability is most likely a combined effect of a larger residual water saturation, which may incorporate a volume of viscous emulsion, and pore blocking by nanoparticle-stabilized droplets of n-octane.

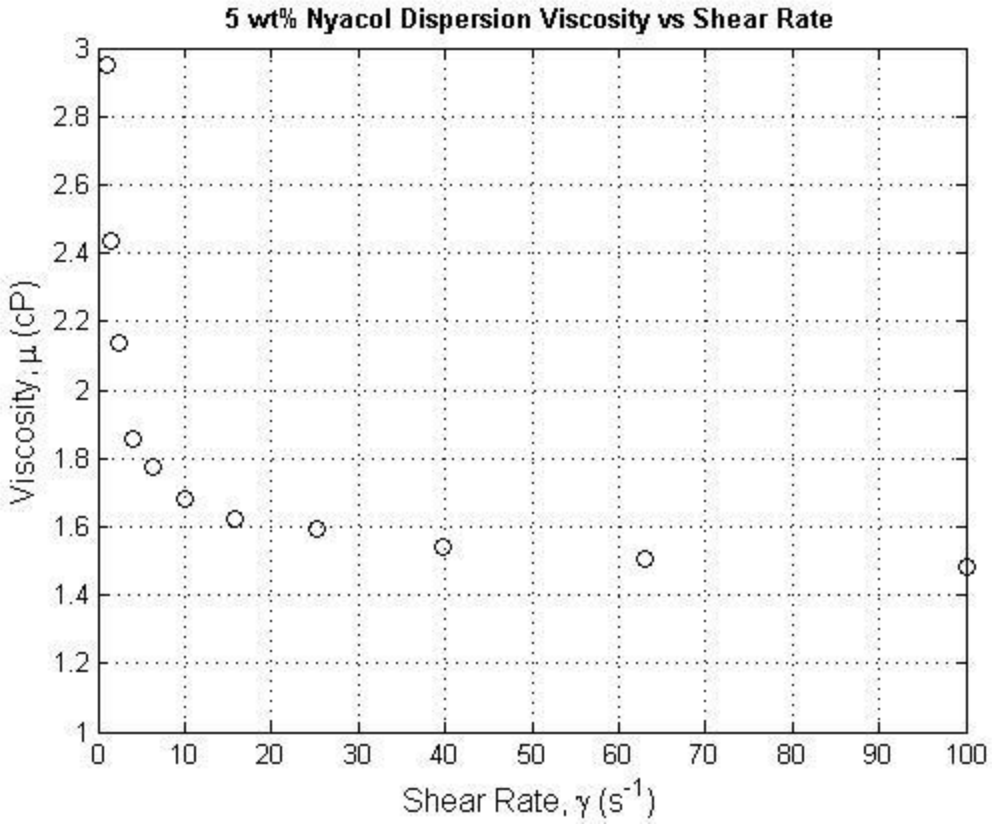

Figure 3.9: Viscosity of 5 wt% Nyacol DP9711 nanoparticle dispersion as a function of shear rate measured by ARES-LS1 machine. Detailed instructions are available in Appendix A2.

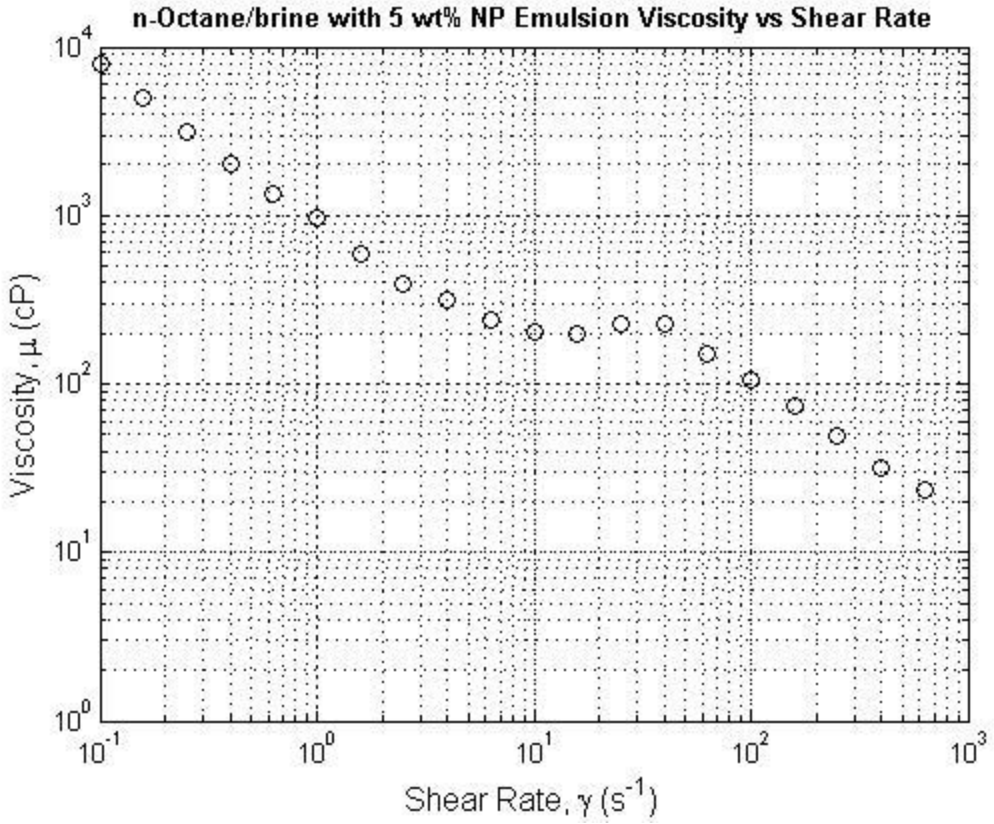

Figure 3.10: Viscosity of n-octane-in-water emulsion stabilized with 5 wt% Nyacol DP9711 nanoparticles at 1:1 n-octane:water ratio as a function of shear rate measured by ARES-LS1 machine. Detailed instructions are available in Appendix A2.

Mobility can also be reduced by an increase in the viscosity. Because emulsions are two orders of magnitude more viscous than the pure phases, the formation of emulsion decreases the effective mobility of the n-octane, brine and emulsion flowing simultaneously in the porous medium. However, the exact extent of the viscosity increase could not be quantified because no effluent sample was available for further characterizations. As discussed above, the large viscosity of the emulsion makes it likely that injected fluid will flow past it, and the shear-thinning rheology of the emulsion

makes it likely to become immobilized in the core once the bypassing by injected fluid begins.

One of the important implications of this experiment is that emulsions can be generated during pore-scale displacement even at a very low shear rate. The shear rate of 85 s^{-1} used during these experiments is two orders of magnitudes smaller than the critical shear rate of 8,000 s^{-1} which Roberts found as the minimum shear rate required to generate stable emulsion during co-injection of nanoparticle dispersion and decane into fractured cores. Although drainage displacement experiment does not produce a continuous stream of stable emulsions, the experimental results suggest that even during a low-shear pore-scale displacement, Roof snap-off exists as an alternative mechanism to co-injection that can generate nanoparticle-stabilized emulsion in porous media.

CO_2 Drainage Displacement Experiment

An analogous experiment was done by Aminzadeh (2013) with CO_2 instead of n-octane. These experiments were carried out in a 3-inch-diameter, 1-foot-length Berea sandstone core using a flow velocity of 0.02 cm/min at 24 ℃ and 1,350 psi. Figure 3.11 shows the overall pressure drop as a function of time, normalized by single-phase brine flow for ease of comparison. These graphs are very similar in pattern to graphs in Figure 3.6 from build-up of pressure drop to the stabilization after breakthrough. The high-frequency noise observed in Figure 3.11 is experimental artifacts due to the presence of a back-pressure regulator. Throughout the injection period, the normalized pressure drop for the nanoparticle case is 1.5 to 2.5 times greater than the control case. Following the same reasoning as n-octane experiment, the overall mobility of CO_2 was decreased by a factor of 1.5 to 2.5, as inferred from the ratio of the normalized pressure drop in the

control and nanoparticle experiments. However, the viscosity ratio between brine and CO_2 is 24, so the viscosity ratio between nanoparticle dispersion and CO_2 is around 10, and the displacement is still unstable in the presence of nanoparticles. Figure 3.12 and Figure 3.13 show the 0.30 mm resolution lateral (y-z plane) CT scans showing slices along the core at 1.5 cm intervals after 0.5 PV injection of CO_2 into the core containing brine with and without nanoparticles. Red corresponds to full water saturation and blue corresponds to full CO_2 saturation. The saturation profile of each slice is shown inside the circle. Compared to the control experiment, images from the nanoparticle experiment show less patches of blue and yellow, indicating that the displacement was more uniform and there was less viscous fingering throughout the core. However, the mobility reduction due to nanoparticles was not enough to stabilize the displacement as both sets of images show significant amount of saturation variations and fingering.

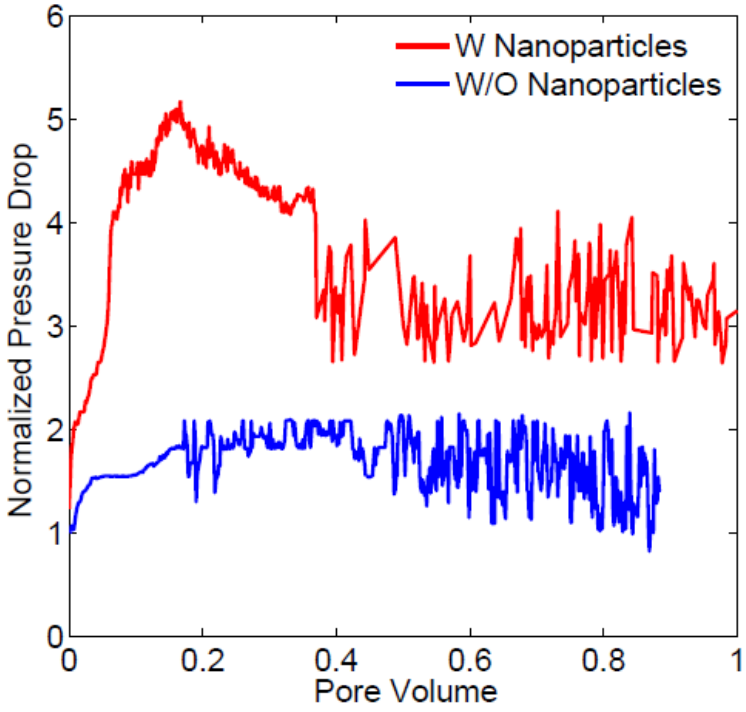

Figure 3.11: Measured pressure drop, normalized by single-phase brine flow, as a function of time for CO_2 injection for the control case (blue) and the nanoparticle case (red) (Aminzadeh 2013).The high frequency noise is due to the presence of a back-pressure regulator.

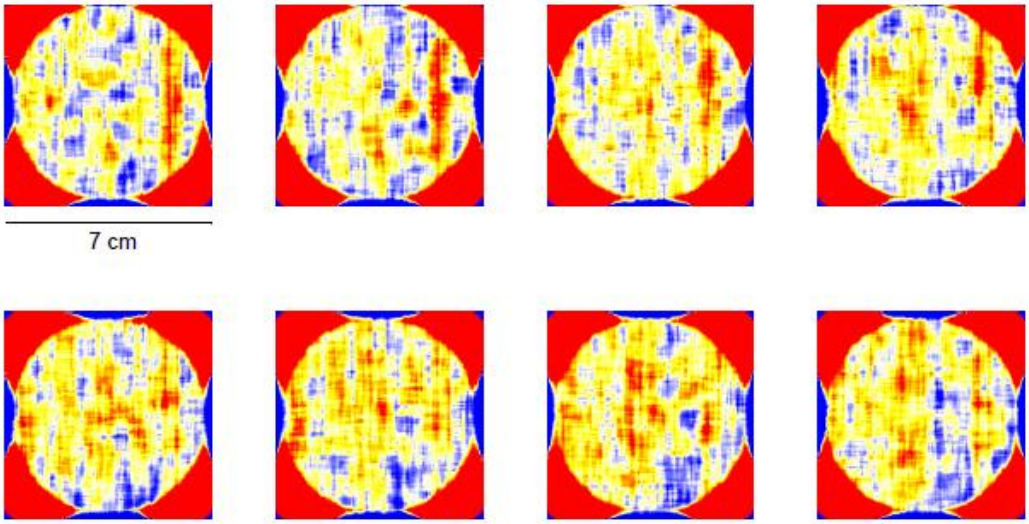

Figure 3.12: Water saturation distribution along the core after 0.5 PV CO_2 injection into a Berea sandstone core initially filled with 2 wt % brine. These z-y slices are 1.5 cm apart longitudinally starting 7 cm from inlet of the core.

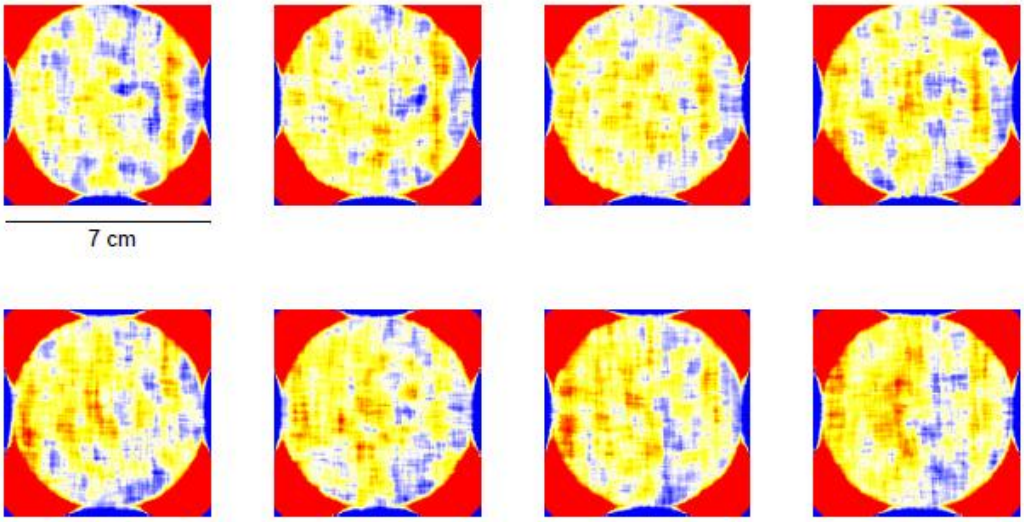

Figure 3.13: Water saturation distribution along the core after 0.5 PV CO_2 injection into the same Berea sandstone core initially filled with 2 wt % brine containing 5 wt% nanoparticle dispersion. These z-y slices are 1.5 cm apart longitudinally starting 7 cm from inlet of the core.

3.5 CONCLUSIONS

Drainage displacement experiments suggest that nanoparticle-stabilized emulsions were generated within the core by pore scale events (Roof snap-off). For n-octane displacing brine with nanoparticles, the generation of emulsion reduced the effective mobility by a factor of 2, which was large enough to stabilize the displacement front and reduce viscous fingering of n-octane. The responsible mechanism for generating these emulsions is Roof snap-off where a brief decrease in capillary pressure at the pore throat during a Haines jump creates disconnected droplets of oil which are then armored by nanoparticles to stabilize oil-in-water emulsions. Haines jumps are common in slow drainage displacements, so this behavior is anticipated to occur for any non-wetting phase injection/invasion process into a reservoir containing wetting phase.

One way to apply this concept to CO_2 sequestration would be to inject an aqueous dispersion of suitable nanoparticles into formations where the risk of leakage is anticipated to be greatest. If buoyancy-driven CO_2 were to enter one of these formations, CO_2 and brine would form nanoparticle-stabilized foam at the displacement front. However, with the mobility reduction factor seen in the CO_2 experiment, any generated foam cannot seal the leak but can only buy time for another remediation method.

Chapter 4

Imbibition Displacement

4.1 MOTIVATION

After injecting CO_2 into an aquifer, some researchers have proposed to inject chase water to push CO_2 away from the injection well to the sequestration site while trapping disconnected droplets of CO_2 as immobile phase (Qi et al., 2009). One potential way to improve residual trapping of CO_2 is by adding colloidal additives in the chase water. Nanoparticles are excellent candidates for such colloids. Nanoparticles have been shown to improve the amount of trapping in the pore space or to increase the sweep efficiency of subsequent CO_2 injection (Aminzadeh et al., 2012). Furthermore, the small size of nanoparticles allows them to travel significant distances in the porous medium with little or no retention on the grain surface.

In the preceding chapter, we have concluded that during drainage displacement Roof snap-off generates oil-in-water emulsions stabilized by nanoparticles. The evidence for formation of oil-in-water emulsion is manifested in the pressure drop data; the pressure drop across the core (relative to pressure drop for single phase brine flow) was 1.3 to 2 times higher in the presence of nanoparticles than the control case. This greater resistance to flow is consistent with the greater viscosity of a flowing emulsion phase, larger saturation of residual phase, and with the blocking of pore throats by stable oil droplet surrounded by aqueous phase. The substantially larger residual phase saturation when nanoparticles were present (S_{wr} = 43% vs S_{wr} = 31% for the control) is also consistent with the establishment of a stationary oil-droplets-in-water phase in the core.

During an imbibition process, Roof snap-off does not occur because no Haines jumps occur. Other forms of snap-off occur during imbibition and cause droplets of non-

wetting phase to be disconnected from the bulk. This disconnection is inherent in pore-level imbibition processes which occur independently of the presence of nanoparticles. The residual phase, whether made up of emulsions or n-octane, will alter the flow path of subsequent nanoparticle injection in the same fashion. Therefore, the hypothesis that Roof snap-off is the main mechanism for generating nanoparticle-stabilized emulsion can be tested by an imbibition displacement experiment. If evidence of nanoparticle-stabilized oil-in-water emulsion were observed in imbibition displacement just as in drainage displacement, there would exist other processes beside Roof snap-off that govern formation of nanoparticle-stabilized emulsions. If, on the other hand, no such evidence is found, it shows that Roof snap-off is the key mechanism for generating nanoparticle-stabilized emulsion, at least in the high permeability, relatively homogeneous sandstones studied here.

4.2 EXPERIMENTAL MATERIALS AND METHODS

Imbibition displacement is defined as a process where wetting phase displaces non-wetting phase in a porous medium. In these experiments described in this chapter, the wetting phase is brine or brine containing nanoparticles and the non-wetting phase initially saturating the porous medium is n-octane. This experiment will test if the Roof snap-off is the main mechanism for triggering formation of nanoparticle-stabilized emulsion in porous media. This section describes the necessary materials and procedures for the imbibition displacement experiments.

4.2.1 Materials

Ultrapure Type 1 water with a resistivity of 18.2 MΩ-cm was prepared by Thermo Scientific Barnstead E-Pure system. Two different types of nanoparticles were used for imbibition experiment. Nyacol Nano Technologies, Inc.'s DP9711 nanoparticles consist of 27 nm silica cores with trade-secret coating for dispersion stability. They were received as dispersions of 20.1 wt% concentration in tap water. 3M Co.'s nanoparticles consist of 5 nm silica cores with PEG chains grafted to the surface. They were received as dispersions of 19.3 wt% concentration. Sodium chloride (NaCl) and isopropyl alcohol (IPA) were purchased from FisherScientific, and n-octane was purchased from ACROS. The purity of NaCl is 99%, IPA 99.9% and n-octane 97%. Three one-inch-diameter and one-foot-length cores were cut from a high-permeability, homogeneous Boise sandstone block.

4.2.2 Experiment Set-up and Procedure

Epoxy Core Preparation

Three Boise sandstone epoxy cores were prepared using the preparation steps detailed in Appendix A1.

Vacuum Saturation

Before the core is used for an experiment, it has to be completely saturated with brine. The set-up used to vacuum saturate the core is shown in Figure 4.1. First, the core is vacuumed to remove any fluid or liquid present in the core. A vacuum pump (Emerson model C63CXGZP-4780) applies a pressure of -3.3 psi. It is connected to a jar full of desiccants that will prevent any moisture from going into the vacuum pump. This process should continue for at least 12 hours. Once the core is completely evacuated, its dry weight is measured. Second, 1 wt% NaCl brine is loaded into a glass column and the valve connection between the glass column and the core is opened to let brine imbibe into the vacuumed core. After the core is saturated, the full weight of the core is measured. The dry and full weight of the core can be used to calculate the porosity and pore volume (PV) of the core.

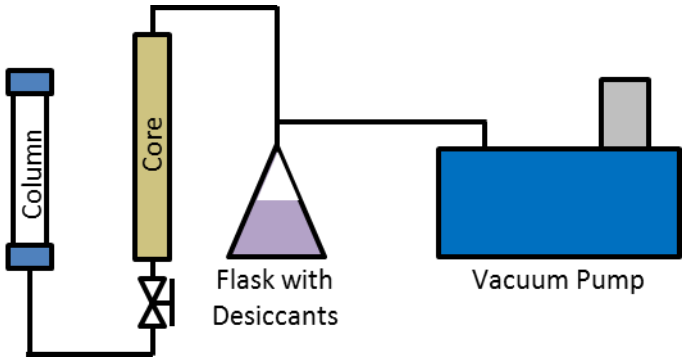

Figure 4.1: Schematics of the vacuum and saturation set-up.

Permeability Measurement

Figure 4.2 is a schematic of the coreflood system that was used to measure the permeability of the core. This procedure also serves as a preparation step for imbibition experiment, which requires 100% n-octane saturation inside the core. The set-up consists of a syringe pump (Teledyne ISCO model 1000D), one glass column (Kontes Chromaflex), and a pressure transducer (Rosemount). The procedure to measure the permeability of the core is as follows:

1. Mount epoxy molded core horizontally. Pressure transducer connects to the two ends of the core.
2. Load syringe pump with ultrapure water.
3. Set up tubing connections as shown in Figure 4.2 a).
4. Set the flow rate at 1 mL/min and start syringe pump.
5. Record the pressure drop across the core measured by the pressure transducer using a LabVIEW program.
6. Check the flow rate.
7. Vary the flow rate; values from three different flow rates were averaged to obtain permeability of the core.
8. After water injection is done, load the syringe pump with IPA.
9. Flush the core with at least 10 PV's of IPA. This miscible displacement replaces all ultrapure water with IPA in the core.
10. After IPA injection is finished, load the syringe pump with ultrapure water.
11. Mount one glass column (Column) vertically.
12. Fill the column with n-octane.
13. Set up tubing connections as shown in Figure 4.2 b).

14. Start syringe pump. Water from the pump enters the column from the bottom and displaces oil into the core.
15. Inject at least 10 PV's of n-octane at 1 mL/min. This miscible displacement replaces all IPA with n-octane and establishes 100% n-octane saturation in the core.

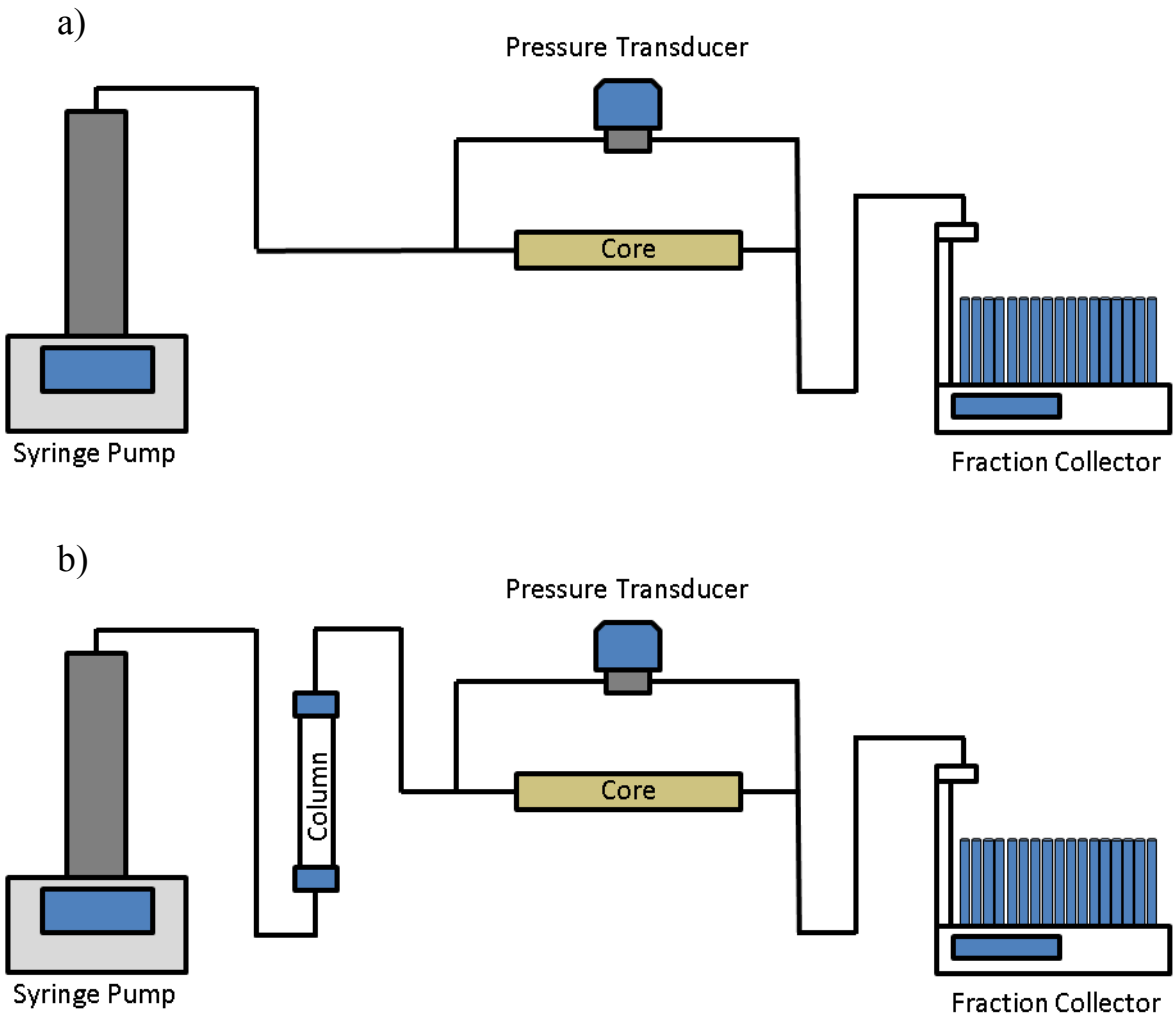

Figure 4.2: Schematics of the coreflood system for a) permeability measurement and b) n-octane saturation process.

Imbibition Experiment

Figure 4.2 is a schematic of the coreflood system that was used to carry out the imbibition displacement experiment. The set-up is a slight modification to the one used for imbibition preparation step. The procedure for imbibition displacement experiment immediately follows the imbibition preparation step as follows:

1. Mount two more glass columns (Column A and Column B) vertically. The Column remaining from the previous procedure is labeled as Column C.
2. Fill Column A with mineral oil.
3. Fill Column B with sample to be injected into the core. In the control experiment, 3 wt% NaCl brine was used. In the nanoparticle experiment, 4 wt% nanoparticles dispersed in 3 wt% NaCl brine was loaded as sample. Load syringe pump with 3 wt% NaCl brine.
4. Fill Column C with n-octane if there is less than 20 mL of n-octane left in the column.
5. Set up tubing connections as shown in Figure 4.2
6. Turn Valve 1 (V1) toward Column C. Set the flow rate for 1 mL/min and start the syringe pump. Water from the pump enters the column from the bottom and displaces n-octane into the core. This step ensures that the core is completely saturated n-octane.
7. Inject until n-octane flow is stabilized as monitored by the pressure drop across the core.
8. After flow stabilizes, turn V1 toward Column A. Set the flow rate for 1 mL/min. Water from the pump enters Column A from the bottom and displaces oil. The displaced oil enters Column B from the top and displaces sample into the core.

9. Record the pressure drop across the core measured by the pressure transducer using a LabVIEW program.
10. Check the flow rate and collect effluent samples using fraction collector.
11. Measure refractive index of collected samples to calculate concentrations.

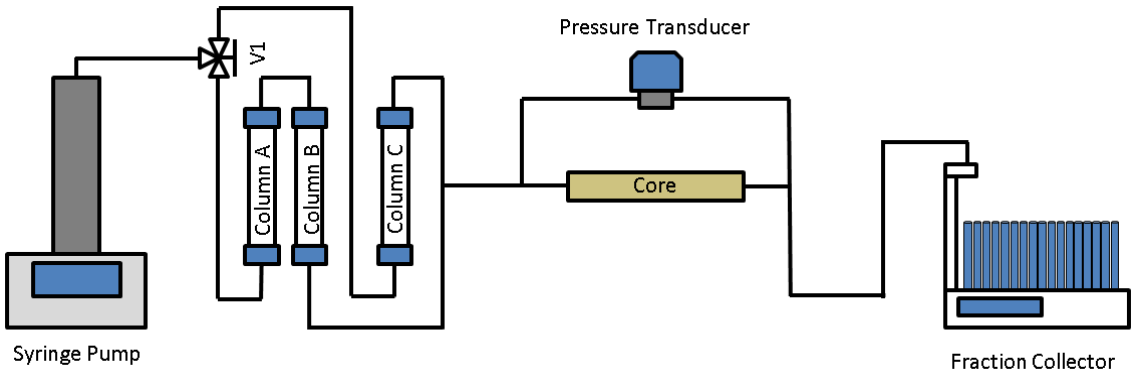

Figure 4.3: Schematic of the coreflood system for imbibition displacement experiment.

The presence of nanoparticles in water alters the refractive index of the aqueous phase, offering a simple method for measuring nanoparticle concentrations in effluent samples. In order to measure concentration of nanoparticles, refractive index has to be calibrated with known concentrations of nanoparticles beforehand. The calibration process is detailed in Appendix A3.

In two of the imbibition displacement experiments, the internal dynamics of the displacement were observed with a modified medical CT scanner (Universal Systems HD-350). The CT scanner allows a direct measurement of the displacement patterns as well as in-situ saturations during flow. The schematic of the coreflood system with a CT scanner is shown in Figure 4.4.

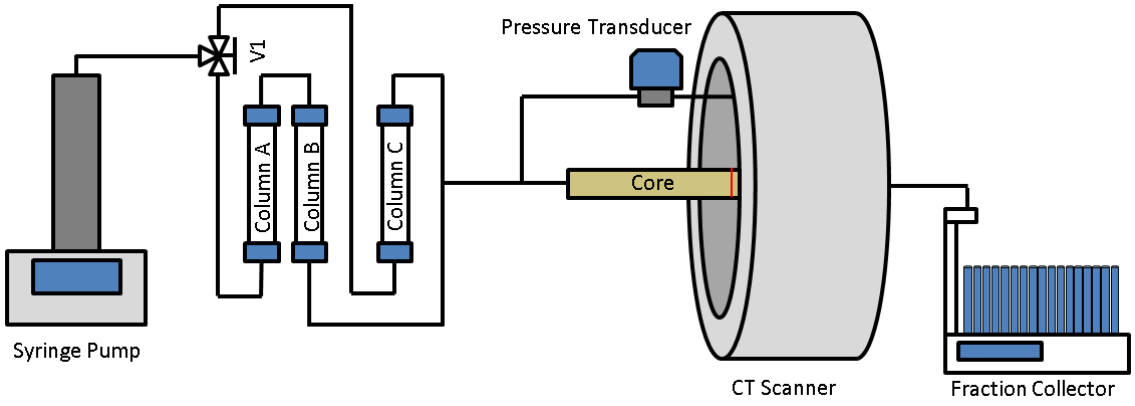

Figure 4.4: Schematic of the coreflood system for imbibition displacement experiment with a CT scanner.

Figure 4.5: Picture of the experiment set-up of Figure 4.4 in a CT scanner.

A summary of experimental protocols are summarized in Table 4.1.

Exp. #	Resident Fluid	Invading Fluid	Flow Rate	Particle	Permeability Porosity	Note
I1	n-octane	1 wt% NaCl	1 mL/min	N/A	1200 mD 21%	Pressure Sample Collection
I2	n-octane	1 wt% NaCl 5 wt% NP	1 mL/min	Nyacol DP9711 27 nm	Same as I1	Pressure Sample Collection
I3	n-octane	2 wt% NaBr	0.5 mL/min	N/A	732 mD* 21%	CT Scan
I4	n-octane	2 wt% NaBr 5 wt% NP	0.5 mL/min	Nyacol DP9711 27 nm	Same as I3	CT Scan
I5	n-octane	2 wt% NaBr 5 wt% NP	0.5 mL/min	3M PEG-Coated 5 nm	1100 mD 23%	CT Scan

Table 4.1: Experimental protocols for imbibition displacement experiments.

* Permeability may be inaccurate due to an unreliable pressure drop measurement.

4.3. RESULTS AND DISCUSSION

Nyacol DP9711 Silica Nanoparticle

As discussed in Chapter 3, during low-shear-rate displacement, any generated emulsions are likely to stay trapped in the porous media and no visual evidence of their generation appears in the effluent samples. Therefore, judgment on whether emulsions are generated must rely on the pressure drop data. Figure 4.6 shows the overall pressure drop as a function of time for Exp I1 and Exp I2.

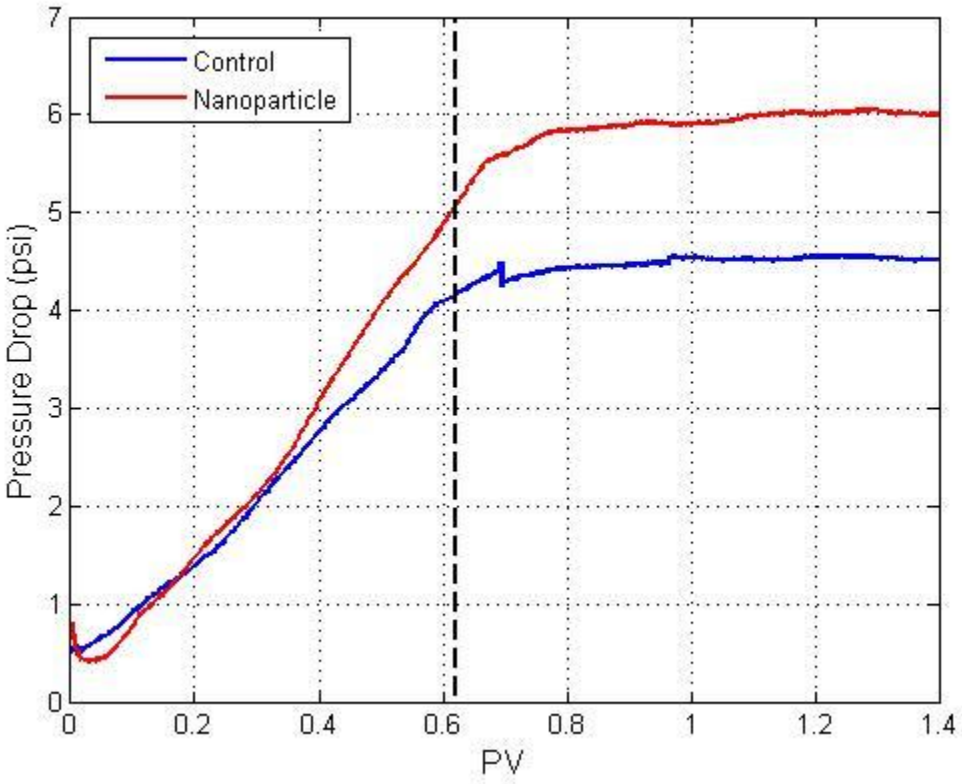

Figure 4.6: Measured pressure drop as a function of time for brine (Exp. I1; blue) or nanoparticle dispersion (Exp. I2; red) injection into Boise sandstone core saturated with n-octane. The dashed line indicates the breakthrough time.

Because the two experiments were done in the same core, the pressure drop histories for the two experiments are directly comparable and no normalization was done. Both graphs in Figure 4.6 show a similar pattern where the pressure drop builds up across the core due to multi-phase flow until breakthrough at 0.62 PV, which was observed in the effluent sample. After breakthrough, the pressure drop goes back down to approach steady-state phase flow of brine or nanoparticle dispersion at residual n-octane saturation. The mobility reduction factor can be calculated by dividing the pressure drop of the nanoparticle experiment by that of the control experiment. The resulting graph is shown in Figure 4.7.

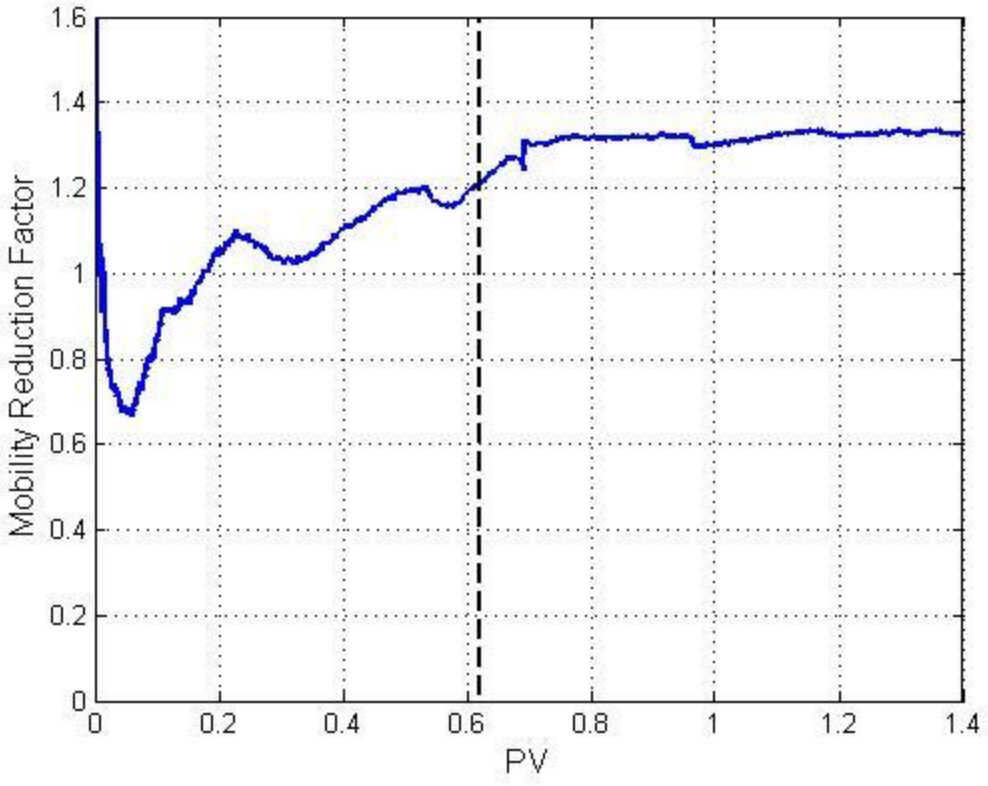

Figure 4.7: Mobility reduction factor inferred from the ratio of the normalized pressure drop of the nanoparticle experiment (Exp. I2) to that of the control experiment (Exp. I1). The dashed line indicates the breakthrough time.

As in Figure 4.7, the mobility reduction factor ranges from 1.1 to 1.4. This difference in pressure drop can be accounted for by the viscosity ratio of 5 wt% nanoparticle dispersion and brine, which is 1.36. The end point relative permeability can be calculated by using the equation

$$k_{rw}^{o} = \frac{\mu_w}{\mu_o}\frac{\Delta P_o}{\Delta P_w}$$

where k_{rw}^{o} is the relative permeability of the aqueous phase (brine for the control and nanoparticle dispersion for the nanoparticle experiment), μ_o and μ_w are viscosities of n-octane and the aqueous phase, respectively, ΔP_o is pressure drop from single-phase n-octane flow at a constant flow rate q_o and ΔP_w is pressure drop from the aqueous phase flow at residual n-octane saturation at constant flow rate $q_w = q_o$. The calculated end point relative permeability of n-octane is 0.27 for the control experiment and 0.28 for the nanoparticle experiment; therefore, there is no evidence for formation of any viscous phase inside the core.

The effluent histories in Figure 4.8 were constructed by collecting effluent samples, determining oleic/aqueous volumes, measuring refractive index of aqueous phase, converting refractive index to concentration, and normalizing concentration by the injected concentration.

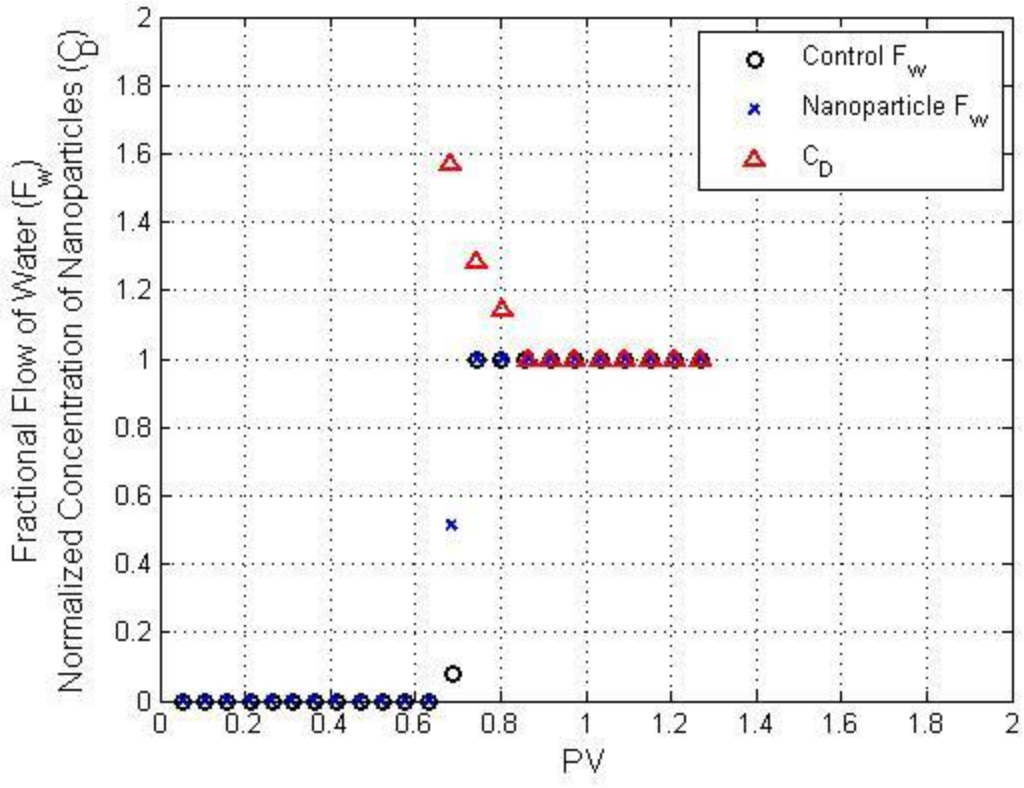

Figure 4.8: Measured fractional flow of water and nanoparticle concentration (normalized by the injected concentration, 5 wt%) as a function of time for Exp. I1 and Exp. I2.

The water cut history and residual oil saturation were similar for both control and nanoparticle experiments, affirming that the overall dynamics of the displacement were similar for the two cases. If emulsions are generated and present in the core, there should be a more significant difference in the pressure drop and residual oil saturation between the control experiment and the nanoparticle experiment, as there was in the drainage experiments described in Chapter 3. This result corroborates the hypothesis that Roof snap-off is the main mechanism by which nanoparticle-stabilized emulsions form and that consequently such emulsions will be formed only during drainage displacements.

During imbibition, other forms of snap-off may also occur depending on the geometry and topology of pore structure. However, the resulting volumes of disconnected oil reside in pore spaces as residual phase. The residual oil remains disconnected, regardless of whether nanoparticles are present. In terms of mobility, the displacing agent, brine, does not care whether the residual oil exists as a phase disconnected by classical imbibition process or, if emulsions were formed, whether the residual oil exists as nanoparticle-armored droplets, as long as the flow path for brine is the same in both cases. Furthermore, residual n-octane saturation from mass balance of effluent samples was the same for both experiments at 38%, indicating the displacement dynamics remained the same even in the presence of nanoparticles.

Although no emulsions were generated during imbibition displacement, Figure 4.8 shows an interesting feature: the measured nanoparticle concentration in the aqueous phase of the effluent is 1.6 times the injected concentration at breakthrough and gradually decreases to the injected concentration. The concentration overshoot suggests that nanoparticles traveled faster than the aqueous phase in which they are dispersed and accumulated at the displacement front. Congruous phenomena were observed during Exp. I3 and Exp. I4, where the internal dynamics of the displacement were captured using a modified medical CT scanner. Figure 4.9 shows the average aqueous phase saturation in a 1-cm thickness slice as a function of distance along the core at different times (PV aqueous phase injected).

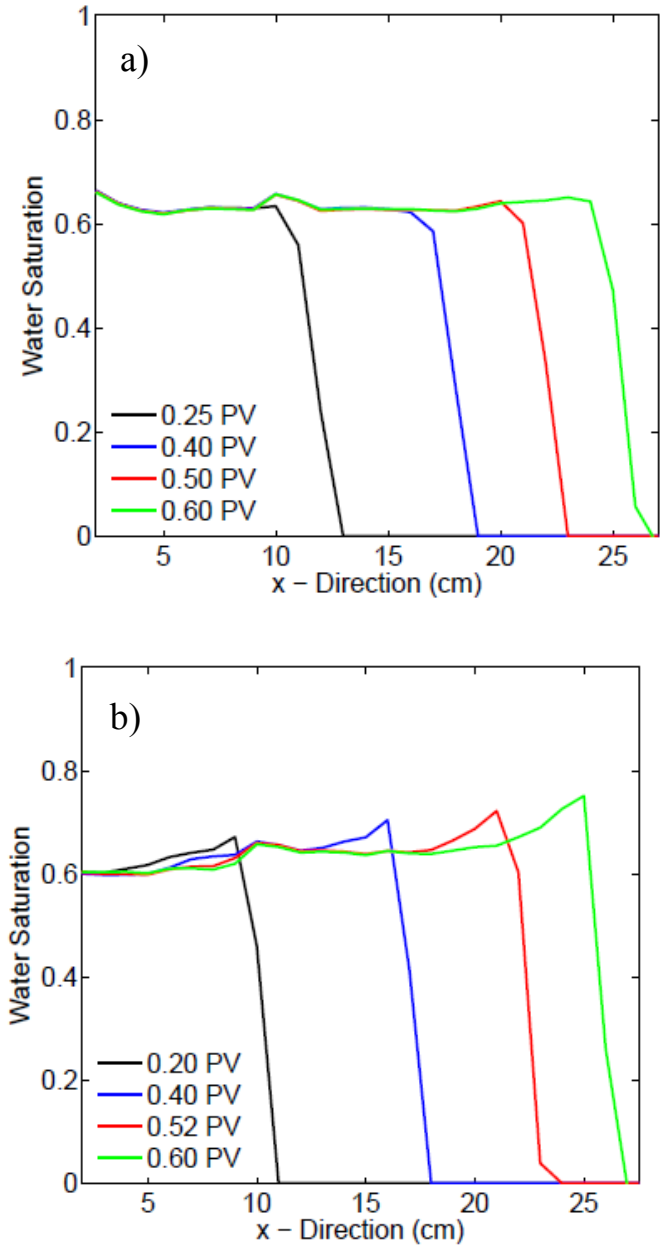

Figure 4.9: Measured laterally-averaged (i.e. slice by slice) aqueous phase as a function of longitudinal distance for injection of: (a) brine, Exp. I3 and (b) brine with nanoparticles, Exp. I4, into Boise sandstone core saturated with n-octane.

Figure 4.9 a) shows the control case and exhibits a sharp decrease in saturation as expected in a piston-like stable displacement where more viscous brine is displacing less viscous n-octane. The nanoparticle experiment in Figure 4.9 b) shows an interesting feature: the aqueous phase saturation at the front appears to be larger than in the plateau behind the front. After the front has passed any given x-direction location, the local aqueous phase saturation in the corresponding slice of the core comes back to normal saturation similar to the control case. However, physically speaking, local aqueous phase saturation cannot suddenly increase and then decrease while a steady flow of brine is being supplied. This apparent saturation overshoot is the result of interpreting the density difference captured by the CT scanner in terms of differences in fluid saturation. If we instead assume that the aqueous phase saturation profile is the same in Figure 4.9 a) and b), then Figure 4.9 b) would show that the aqueous phase density at the front of the flood was higher than the aqueous phase density elsewhere in the core. If we assume that the aqueous phase density is a function of nanoparticle concentration, Figure 4.9 b) would indicate that the nanoparticle concentration at the front of displacement was higher than the injected nanoparticle concentration. This interpretation is in agreement with the effluent concentration measurement in Figure 4.8 during Exp. I2. Furthermore, the nanoparticle concentration at the front seems to be increasing with time as the amplitude of the "saturation overshoot" peak plotted in Figure 4.9 b) suggests.

Figure 4.10 shows the measured pressure drop across the core, normalized by the single-phase n-octane flow, as a function of time for Exp. I3 and Exp. I4. During this experiment, the pressure transducer was not calibrated correctly and the measured values do not reflect the true pressure drop across the core. This inaccuracy leads to the core permeability that is significantly lower than the permeability in other cores from the same rock block as shown in Table 4.1. Nonetheless, nanoparticle curve being on top of the

control curve is still consistent with the previous observations in Figure 4.6 that no nanoparticle-stabilized droplets formed during imbibition.

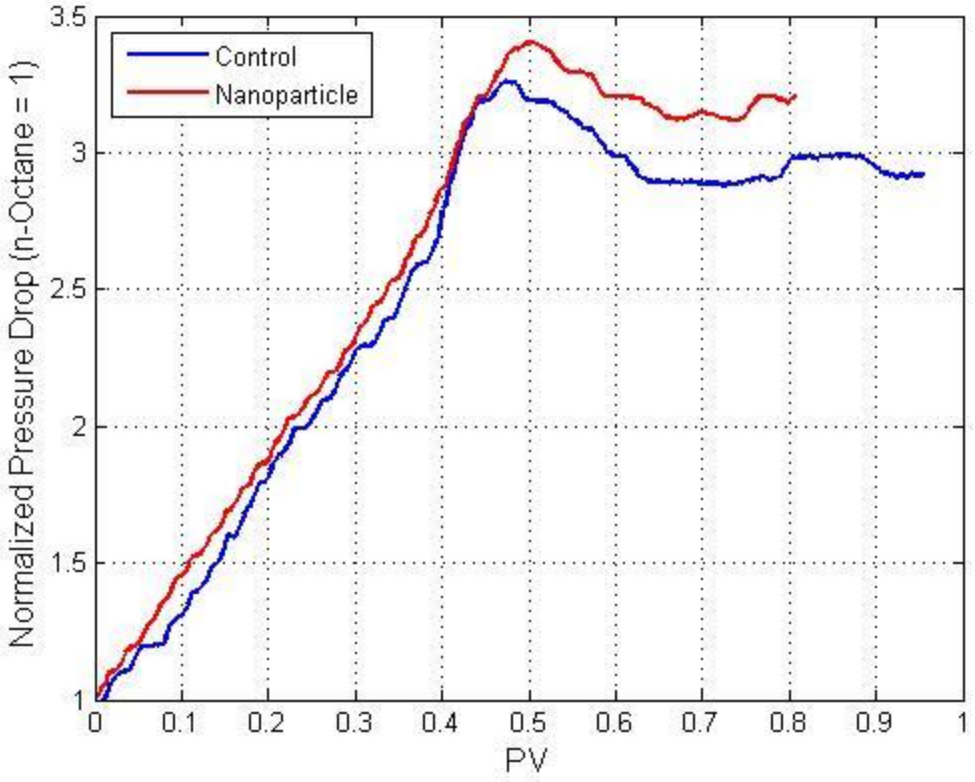

Figure 4.10: Normalized pressure drop as a function of time for brine (Exp. I3; blue) or nanoparticle dispersion (Exp. I4; red) injection into Boise sandstone core saturated with n-octane.

In order to see if this "saturation overshoot" can be universally observed with other nanoparticles, Exp. I5 was run with 3M's 5 nm PEG-coated silica nanoparticles instead of Nyacol's 27 nm nanoparticles. Figure 4.11 shows the overall aqueous phase saturation as a function of distance along the core at different PV of nanoparticle dispersion injection.

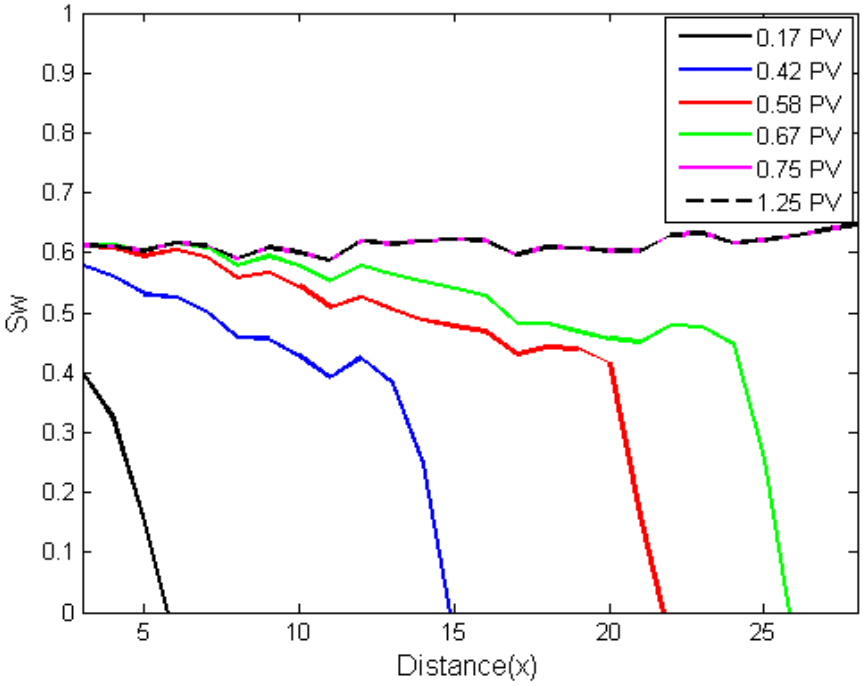

Figure 4.11: Measured laterally-averaged water saturation as a function of longitudinal distance for injection of brine with nanoparticles, Exp. I5, into Boise sandstone core saturated with n-octane.

Saturation profiles indicate no sign of overshoot; variations near the front of the saturation profile, such as one found in blue curve at 0.42 PV injection, seems to be due to variations in local heterogeneity of the core at x = 13 cm. The lack of saturation overshoot with 5 nm 3M nanoparticles suggests that the physics governing the overshoot seen with Nyacol's 27 nm nanoparticles is dependent on the size of the particle.

Potential Mechanism for Concentration Overshoot

One potential explanation that results in higher concentrations of nanoparticles at the displacement front is enhanced transport of nanoparticles; that is, nanoparticles are traveling faster than the brine phase in which they are dispersed and as they encounter the displacement front, they start to accumulate because ahead of the displacement front is pore space that is 100% saturated with n-octane into which nanoparticles cannot diffuse. One physical mechanism that can cause such accelerated transport of nanoparticle is size exclusion. Size exclusion or excluded pore volume effect is a well-known phenomenon in polymer flooding (Dawson and Lantz, 1973). The interstitial velocity V_p of the solvent phase is

$$V_p = \frac{q}{A\phi}$$

where q is the volumetric flow rate of the solvent, A is the cross-sectional area of the porous medium and ϕ is the total porosity of the porous medium. If the individual molecules that make up the concentration of a solute in the solvent are too big to travel through certain sizes of pores, the resulting smaller porosity accessible to the molecules ϕ_{eff} will lead to higher interstitial velocity V_m for the molecules than for the solvent. This can be written as:

$$\frac{V_m}{V_P} = \frac{\phi}{\phi_{eff}} = 1 + \frac{\Delta\phi}{\phi_{eff}}$$

Clearly V_m/V_p is greater than unity. Figure 4.12 shows the earliest observation of this effect documented by Dawson and Lantz (1972) where a solution of polyacrylamide

and tracer salt was injected; an earlier arrival of the large polymer molecules was observed in the effluent compared to the much smaller tracer atoms.

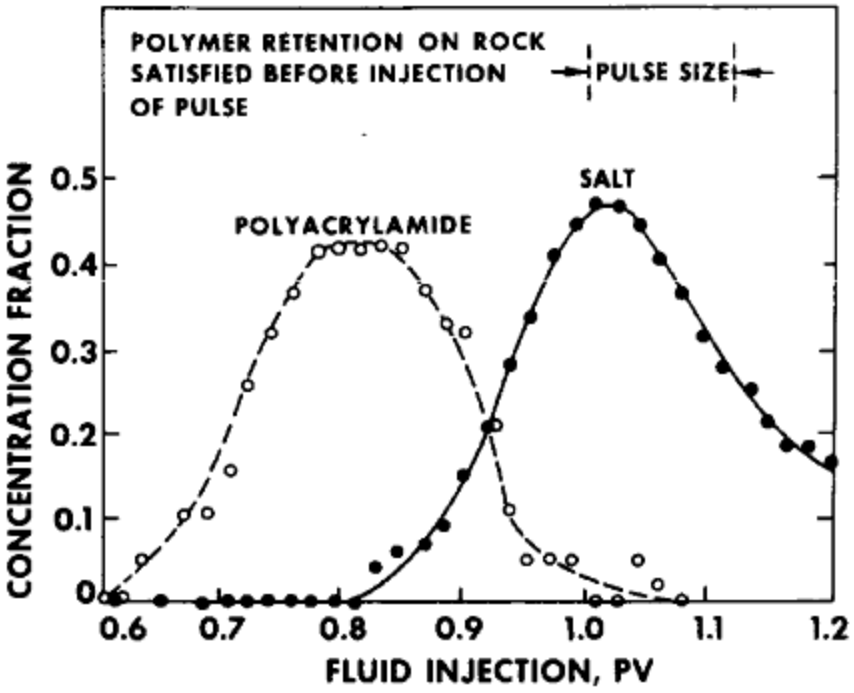

Figure 4.12: Measured effluent concentration as a function of time for polyacrylamide and salt demonstrates the early arrival of polymer by size exclusion (Dawson and Lantz, 1972).

Because size of nanoparticles is typically much smaller than pore throats in high permeability porous media, it is questionable whether the size exclusion mechanism responsible for polymer's accelerated transport is taking place with nanoparticles. But, the fact that saturation overshoot was observed with 27 nm nanoparticle but not with 5 nm nanoparticle supports the size exclusion theory. Evidently, some pore space was inaccessible to 27 nm nanoparticles but was accessible to 5 nm nanoparticles. Therefore, if more experiments are conducted with varying sizes of nanoparticles, there should be evident differences in the overshoot amount. The excluded pore volume effect described

here does not depend on the presence of a second, immiscible fluid phase, so the effect should also be observed during single-phase flow, which will be discussed in more detail in Chapter 5.

4.4. CONCLUSIONS

From the results obtained during imbibition displacement experiments, whether emulsions were generated or not, the presence of nanoparticles did not affect the dynamics of imbibition displacement; the pressure drop during imbibition displacement was essentially the same when corrected for the viscosity of the aqueous phase. Therefore, the residual phase, whether made up of emulsions or n-octane, obstructed the flow path of subsequent nanoparticle injection in the same fashion. Moreover, the residual oil saturation after aqueous phase injection was the same whether nanoparticles were present or not. This behavior, i.e. the absence of an effect of nanoparticles on an imbibition displacement, is strong support for the hypothesis advanced in Chapter 3, namely that the Roof snap-off events at the drainage displacement front are the only mechanism by which stabilized droplets are generated when one fluid phase displaces another.

Accumulation of nanoparticles at the saturation front of the imbibition displacement was inferred from an increased aqueous phase density at the front within the core (observed by the CT scanner) and an increased nanoparticle concentration at the front in the effluent measured by refractive index. This concentration overshoot phenomenon was observed with 20 nm silica nanoparticles but not with 5 nm silica nanoparticles. Therefore, it is hypothesized that this accumulation is due to accelerated transport of nanoparticles by size exclusion.

These results suggest that nanoparticle dispersions will not suffer from significant loss of injectivity during their injection into reservoir formations even in the presence of non-wetting phase, such as CO_2 or oil. Furthermore, we can take advantage of the same mechanism that accumulates nanoparticle at the displacement front to build up high

concentrations of nanoparticle in-situ while only requiring a lower concentration at the injection site.

Chapter 5

Accelerated Transport of Nanoparticles in Porous Media

5.1 MOTIVATION

Many applications of nanoparticles in the oil and gas industry require high transportability of nanoparticles through porous media. In a CO_2 sequestration project, nanoparticles have to travel long distances to target zones, e.g. the seal above the sequestration site. Therefore, the amount of retention directly affects the cost of operation. In addition, for applications in shallow formations or inadvertent discharges at the surface, there may be environmental concerns about the region affected by these small particles. Therefore, it is very important to understand the transport mechanism of nanoparticle dispersions in porous media.

This section will demonstrate the accelerated transport of nanoparticles in porous media that was invoked to explain observations during imbibition displacement experiment described in Chapter 4 and proposes mechanisms for accelerated transport. The current hypothesis is that the acceleration of nanoparticles is caused by inaccessible pore volume. If this is true, the acceleration should be observed regardless of the presence of a second immiscible phase, which was n-octane in the displacement experiments.

5.2 EXPERIMENTAL MATERIALS AND METHODS

During this experiment, nanoparticle dispersions and tracer are injected into Boise and Berea sandstone cores. The high-resolution effluent concentration histories for both species are captured by an in-line UV-Vis detector. This section describes the necessary materials and procedures for nanoparticle single-phase flow experiments.

5.2.1 Materials

Ultrapure Type 1 water with a resistivity of 18.2 MΩ-cm was prepared by Thermo Scientific Barnstead E-Pure system. Nanoparticles (Nyacol DP9711) used for these single-phase flow experiments were received from Nyacol Nano Technologies, Inc. These particles consist of silica cores and trade-secret coating for dispersion stability and the diameter is 27 nm. They were received as dispersions of 20.1 wt% nanoparticle concentration in tap water. Sodium chloride (NaCl), sodium iodide (NaI), isopropyl alcohol (IPA) were purchased from FisherScientific. The purity is 99% for NaCl and NaI and 99.9% for IPA. One one-inch-diameter and one-foot-length core was cut from a high-permeability, heterogeneous Boise sandstone block and another one-inch-diameter and one-foot-length core was cut from a less permeable, homogeneous Berea sandstone block.

5.2.3 Experiment Set-up and Procedure

Epoxy Core Preparation

One Boise and one Berea sandstone epoxy cores were prepared using the preparation steps detailed in Appendix A.1.

Vacuum Saturation

Before the core is used for an experiment, it has to be completely saturated with brine. The set-up used to vacuum saturate the core is shown in Figure 5.1. First, the core is vacuumed to remove any fluid or liquid present in the core. A vacuum pump (Emerson model C63CXGZP-4780) applies a pressure of -3.3 psi. It is connected to a jar full of desiccants that will prevent any moisture from going into the vacuum pump. This process should continue for at least 12 hours. Once the core is completely evacuated, its dry weight is measured. Second, 0.3 M NaCl brine is loaded into a glass column and the valve connection between the glass column and the core is opened to let brine imbibe into the vacuumed core. After the core is saturated, the wet weight of the core is measured. The dry and wet weight of the core can be used to calculate the porosity and pore volume (PV) of the core.

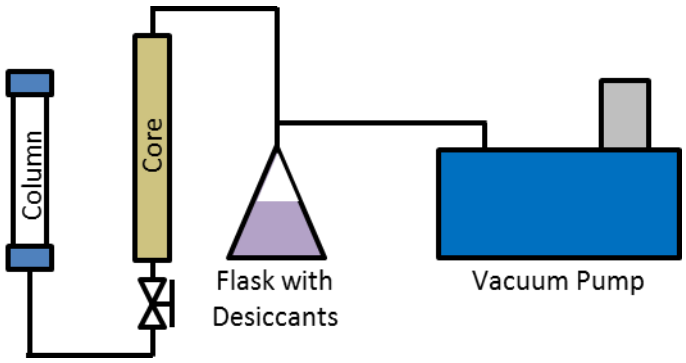

Figure 5.1: Schematics of the vacuum and saturation set-up.

Single-Phase Flow Experiment

Figure 5.2 is a schematic of the coreflood system that was used to measure the permeability of the core and carry out the single-phase flow experiment. The set-up consists of a syringe pump (Teledyne ISCO model 1000D), two glass columns (Kontes

Chromaflex), a pressure transducer (Rosemount), a multi-wavelength-channel UV-Vis detector (ThermoScientific MWD-3000), and a fraction collector (Teledyne ISCO Retriever 500). The procedure to measure the permeability of the core and do the single-phase flow experiment is as follows:

1. Mount epoxy molded core horizontally. Pressure transducer connects to the two ends of the core.
2. Mount three glass columns (Column A, Column B, and Column C) vertically.
3. Fill the pump with 0.3 M NaCl brine.
4. Fill Column A with mineral oil.
5. Fill Column B with sample to be injected into the core. In one experiment, 1 wt% nanoparticle dispersed in 0.3 M NaI was loaded. In another experiment, 0.5 wt% nanoparticle dispersed in 0.3 M NaCl was loaded.
6. Fill Column C with 1 wt% nanoparticle dispersed in 0.3 M NaI to be injected into the core.
7. Set up tubing connections as shown in Figure 5.2.
8. Turn Valve 1 (V1) toward the filter element. Set the flow rate for 1 mL/min and start the syringe pump. Water from the pump will enter the column, go through the UV-Vis detector, and end up at the fraction collector.
9. Start Chromeleon program for UV-Vis detector. The sampling frequency is 1 Hz. Set autozero time to be between one and two hours. Autozero feature sets the absorbance unit for steady-state 0.3 M NaCl flow as the baseline measurement.
10. After autozero is finished, turn V1 toward column A and V2 toward Column B to start injecting sample in Column B into the core. Water from the pump enters Column A from the bottom and displaces oil. The displaced oil enters Column B from the top and displaces sample B into the core.

11. After injecting sample in Column A, turn V2 toward Column C to inject sample in Column C into the core. Water from the pump enters Column A from the bottom and displaces oil. The displaced oil enters Column B from the top and displaces sample B into the core.
12. After injection is finished, turn V1 toward filter to begin postflush.
13. Pressure drop across the core is measured by the pressure transducer and recorded using a LabVIEW program. This information can be used to obtain permeability of the core and apparent viscosity of nanoparticle dispersion.
14. Check the flow rate and collect effluent samples using fraction collector.
15. Post-process UV-Vis absorbance measurement to find concentrations. The detailed instructions for UV-Vis data processing can be found in Appendix A.4.
16. Measure refractive index of collected samples to confirm UV-Vis measurement.

In order to measure accurate effluent concentrations, UV-Vis machine has to be calibrated with known concentrations of tracer and nanoparticles beforehand. The calibration process is detailed in Appendix A.3.

A summary of experimental protocols are summarized in Table 5.1.

Exp. #	Slug in Sample A	Slug in Sample B	Core Permeability Porosity	Flow Rate
A1	2.1 PV of 0.3 M NaI, 1 wt% NP	1.7 PV of 0.3 M NaI, 1 wt% NP	Boise 1800 mD 23%	1 mL/min
A2	2.2 PV of 0.3 M NaCl, 0.5 wt% NP	2.2 PV of 0.3 M NaI, 1 wt% NP	Same core as A1	1 mL/min
A3	2.9 PV of 0.3 M NaCl, 0.7 wt% NP	4.4 PV of 0.3 M NaI, 1.4 wt% NP	Berea 280 mD 17%	1 mL/min
A4	5.1 PV of 0.3 M NaCl, 1 wt% NP	4.8 PV of 0.3 M NaCl, 1 wt% NP	Same core as A3	1 mL/min

Table 5.1: Experimental protocols for single-phase flow experiments.

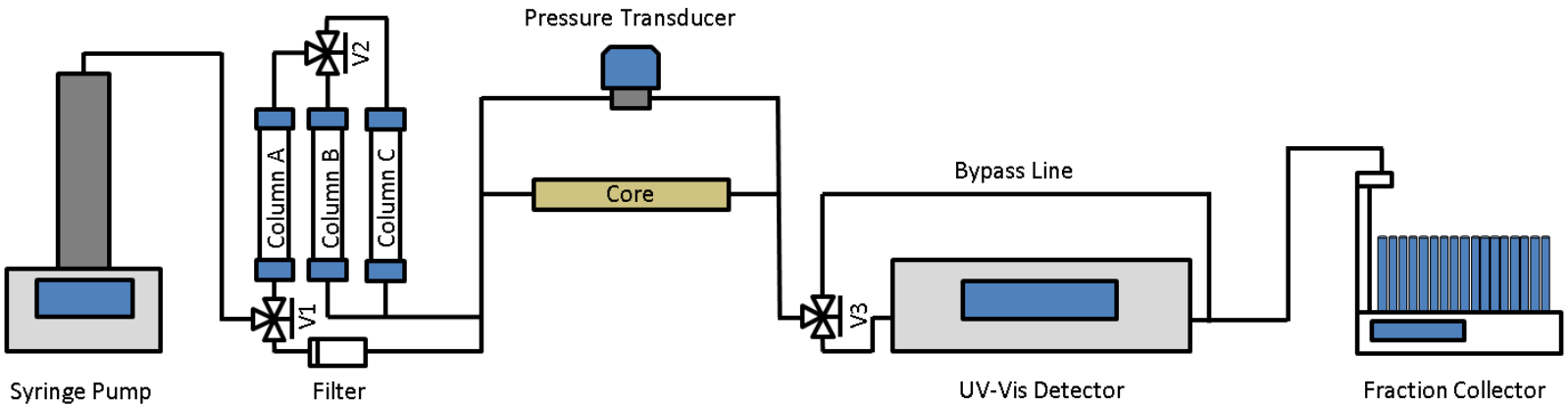

Figure 5.2: Schematic of the coreflood system for single-phase flow experiment.

5.3 RESULTS AND DISCUSSION

This section presents four single-phase flow experiments. The first two experiments (Exp. A1 and Exp. A2) were carried out using a Boise sandstone core and the other two experiments (Exp. A3 and Exp. A5) were carried out in a Berea sandstone core. These experiments were designed to measure whether the nanoparticles show accelerated transport of nanoparticles when compared to the tracer. Any experimentation is prone to errors sourcing from natural variations in measurements, uncertainty inherent in measurement devices, incomplete volume control, and so on. If the velocities of the tracer and the nanoparticles are inferred from two different transport experiments (one for tracer, one for nanoparticles), these errors would interfere with interpreting the relative difference in the velocities of the two components. That is, the errors may bias the results one way or the other, leading to a possible combined effect of augmenting or decimating the difference in the two velocities. These problems can be circumvented by injecting a volume of aqueous phase that contains both the nanoparticles and the tracer; the variations affect the nanoparticle and the tracer exactly the same way, so the relative speeds of the nanoparticles versus the tracer can be correctly inferred.

Boise Sandstone

The first sets of experiments (Exp. A1 and Exp. A2) were carried out using a Boise sandstone core. In Exp. A1, 3.8 PV of nanoparticle and tracer slug (0.3 M NaI, 1 wt% NP) was injected into the core, followed by post-flushing with 0.3 M NaCl brine. Molarities of the salts in the two solutions were kept the same to remove any chemical potential gradient between two different solutions.

Figure 5.3 shows the effluent concentration history of tracer and nanoparticle as a function of time. The dashed box indicates the size of the sample slug injected into the core and when the leading and trailing edges of the slug would arrive in the effluent if the injected components underwent no interaction with the porous medium. The data appear as a continuous curve because the inline measurement allows very high resolution in time, in this case 0.00048 PV (1 Hz). Both concentrations of the tracer and nanoparticles are normalized by the respective injected concentration. If the tracer had undergone only dispersion and no interaction with the porous media, the effluent concentration curve can be estimated by solving the convection-diffusion equation with an infinite-core boundary condition. The result is a superposition of a positive error function symmetric about (PV = 1, C_D = 0.5) and a negative error function symmetric about (PV = 4.8, C_D = 0.5). As can be seen in Figure 5.4, the measured tracer curve deviates from the infinite-core solution with a Peclet number of 20.7; the measured tracer is consistently below the classical curve at the initial front, and consistently above the classical curve at the final front. It is unclear exactly why this deviation occurs, but one possible explanation is the highly heterogeneous nature of the Boise sandstone core used for the experiment.

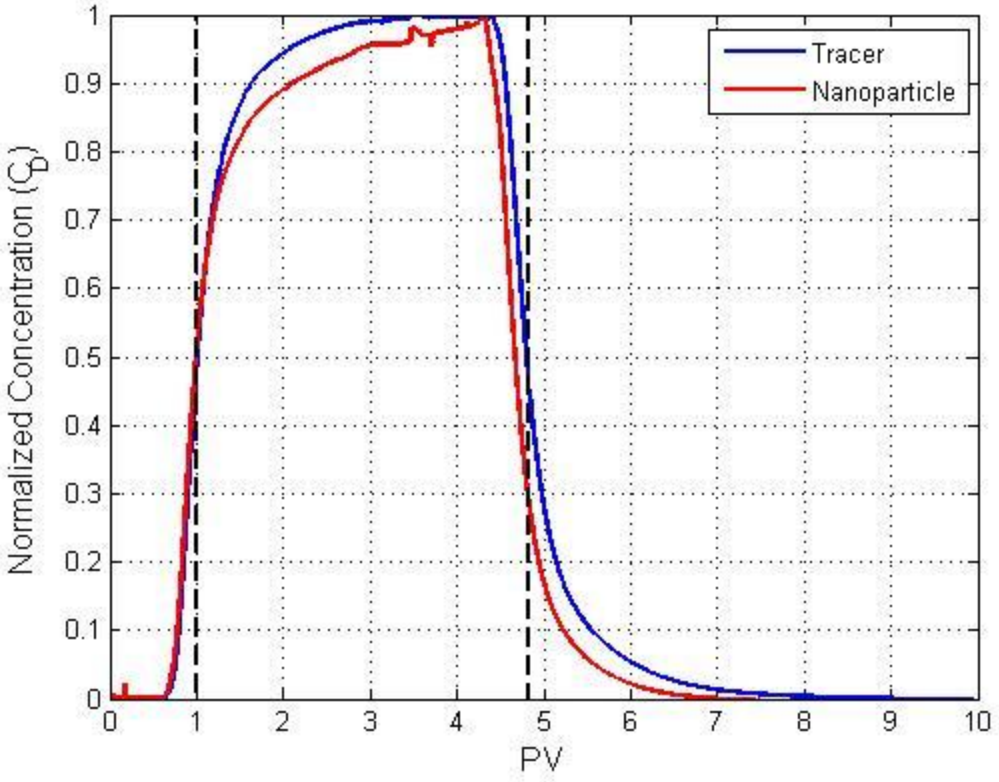

Figure 5.3: Measured concentration of tracer (blue) and nanoparticle (red) as a function of time for 3.81 PV injection of tracer and nanoparticle into Boise sandstone core for Exp. A1. Nanoparticle concentrations are normalized to the injected concentration of 1 wt%. Data appear as continuous lines because of very high frequency in-line acquisition. Dashed line indicates effluent concentration history for an ideal passive tracer that undergoes no dispersion.

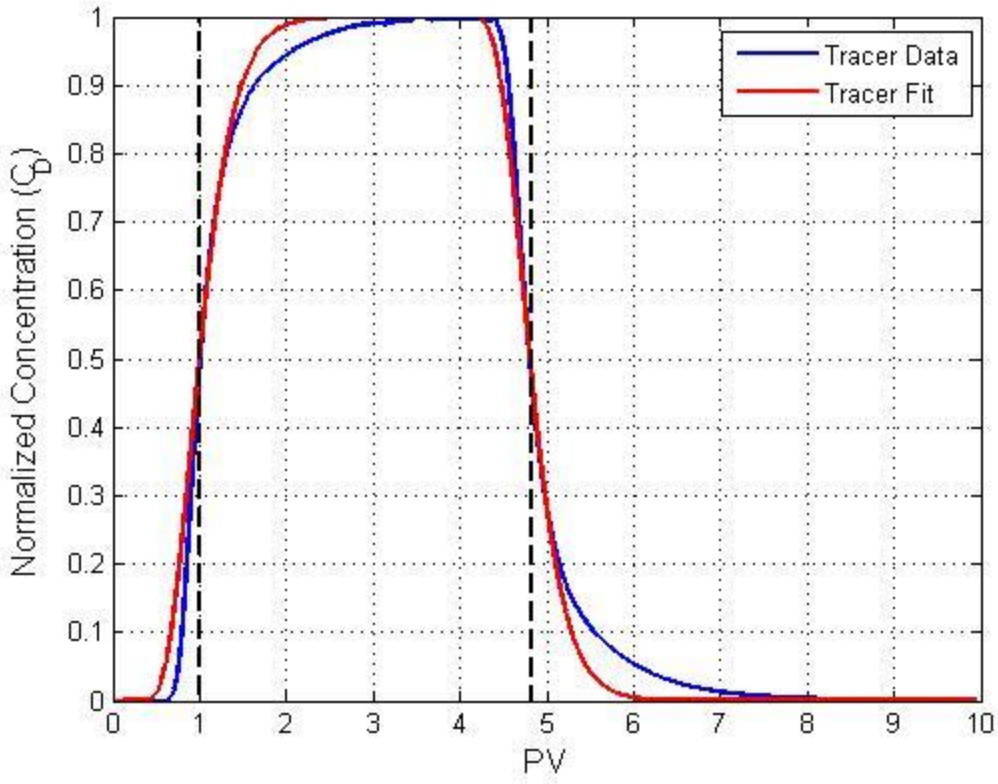

Figure 5.4: Measured concentration of tracer as a function of time (blue; same as Figure 5.3) and fitted infinite-core solution with $N_P = 20.7$ (red) for 3.81 PV injection of tracer and nanoparticle into Boise sandstone core for Exp. A1. Data appear as continuous lines because of very high frequency in-line acquisition. Dashed line indicates effluent concentration history for an ideal passive tracer that undergoes no dispersion.

The area under each curve gives the total PVs of nanoparticle or tracer that was recovered in the effluent after postflush. By comparing these recovered volumes to the injected volume, the retention of nanoparticle in the core can be calculated. For Exp. A1, the retention of nanoparticle was about 7% and tracer 2%. The nanoparticle retention is consistent with values that Zhang (2012) reported for Nyacol DP nanoparticle flow experiments. The 'retention' of the tracer suggests that the experiment had errors in

volume control. There may also have been dead-end pores in the core and not all of the tracer ions were recovered from these dead-end pores.

Figure 5.5 is a magnified view of the leading edge of the slug in Figure 5.3 and shows that nanoparticles arrived at the detector earlier than the tracer. However, the nanoparticle concentration is surpassed by the tracer concentration at 1.1 PV because nanoparticles undergo retention in the porous media.

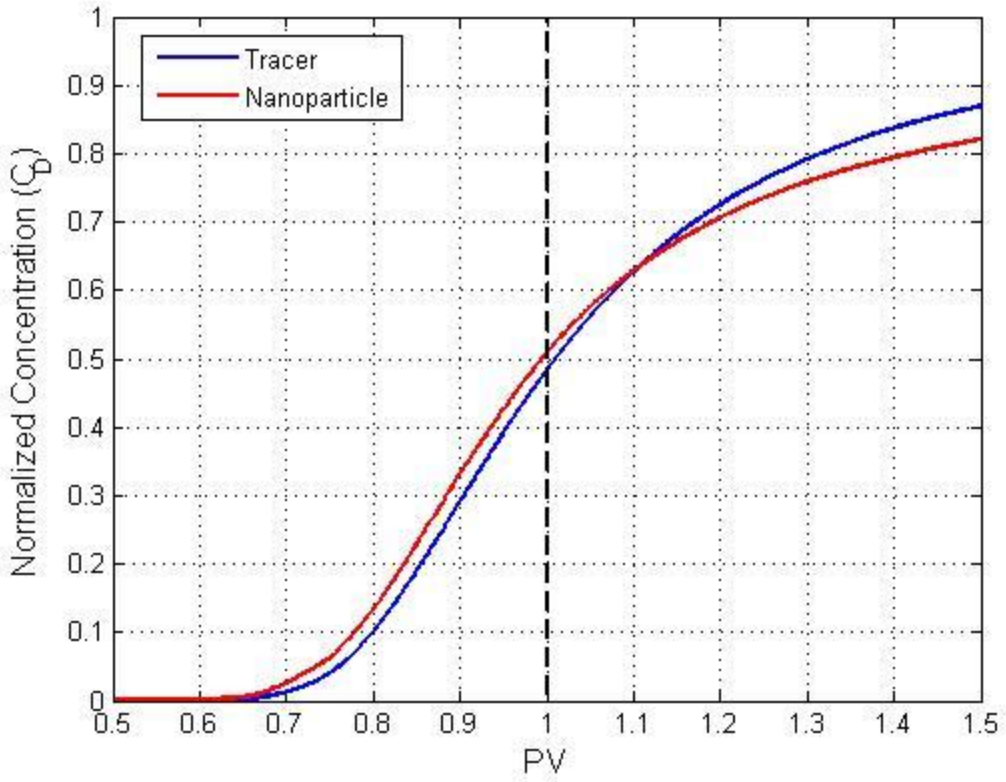

Figure 5.5: Leading edge of measured concentration of tracer (blue) and nanoparticle (red) as a function of time for 3.81 PV injection of tracer and nanoparticle into Boise sandstone core for Exp. A1. Nanoparticle concentrations are normalized to the injected concentration of 1 wt%. Data appear as continuous lines because of very high frequency in-line acquisition. Dashed line indicates effluent concentration history for an ideal passive tracer that undergoes no dispersion.

Figure 5.6 shows the magnified view of the trailing edge of the measured concentration history in Figure 5.3.

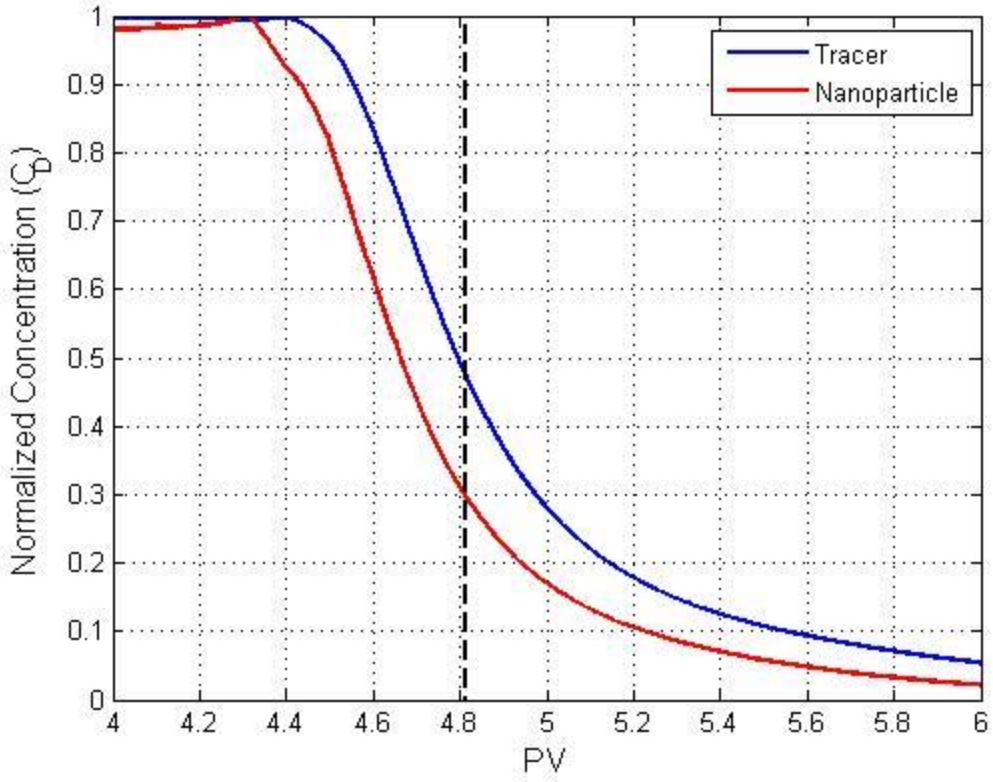

Figure 5.6: Trailing edge of measured concentration of tracer (blue) and nanoparticle (red) as a function of time for 3.81 PV injection of tracer and nanoparticle into Boise sandstone core for Exp. A1. Nanoparticle concentrations are normalized to the injected concentration of 1 wt%. Data appear as continuous lines because of very high frequency in-line acquisition. Dashed line indicates effluent concentration history for an ideal passive tracer that undergoes no dispersion.

At the trailing edge, the gap between the tracer and nanoparticle is wider than observed in the leading edge. One explanation is that by the time the trailing edge arrives, the nanoparticles have filled all available adsorption sites in the core and their transport

now shows the full extent of acceleration with no hindrance from retention in porous media.

If we apply the same idea to the imbibition displacement experiment discussed in Chapter 4, nanoparticles would accumulate at the two-phase displacement front because nanoparticles travel at a higher velocity than the aqueous phase in which they are dispersed. To a CT scanner, the accumulation would be seen as a higher density fluid. Moreover, as adsorption sites get filled, nanoparticles travel even faster, unhindered by delay due to adsorption. As a result, the density (concentration of particles) at the front should increase with distance traveled. If we took effluent samples and measured their concentrations, we would see higher concentrations of nanoparticles than the injected concentration at the displacement front. These are precisely the observations we made during imbibition displacement in Chapter 4.

Figure 5.7 shows the overall pressure drop as a function of time for the experiment. The dashed line indicates the start of post-flushing procedure. Because the UV-Vis detector imposes a high pressure resistance, the flow system must maintain a pressure greater than about 30 psi for fluid flow through the detector. As detailed in Appendix A5, after a baseline is set to autozero the UV-Vis measurement for steady-state brine flow, sample slug in the glass column is injected into the core (refer to experimental procedures in Chapter 5.2.3 and Figure 5.2) and this time is set as PV = 0 shown in Figure 5.7. Since the pressure in the glass columns is smaller than the required pressure, Figure 5.7 shows the pressure drop across the core building up to reach steady-state during the first PV of injection. The pressure drop eventually reaches the steady-state value for nanoparticle dispersion (1 psi) after about 2.3 PV of injection. After post-flushing begins at 3.81 PV, the pressure drop comes back down to that for a steady-state brine flow of 0.9 psi. The ratio between the pressure drop during nanoparticle dispersion

injection and brine injection (1/0.9 = 1.11) is smaller than one observed during drainage and imbibition displacement experiments in Chapter 3 and Chapter 4 because the nanoparticle concentration in displacement experiments was 5 wt% compared to 1 wt% in this single-phase flow experiment. The viscosity of 1 wt% nanoparticle dispersions was not measured. But, assuming that the viscosity of nanoparticle dispersions varies linearly with the concentration between 1 cP (0 wt% nanoparticle) and 1.5 cP (5 wt% nanoparticle), the viscosity of 1 wt% nanoparticle dispersion can be interpolated as 1.1 cP.

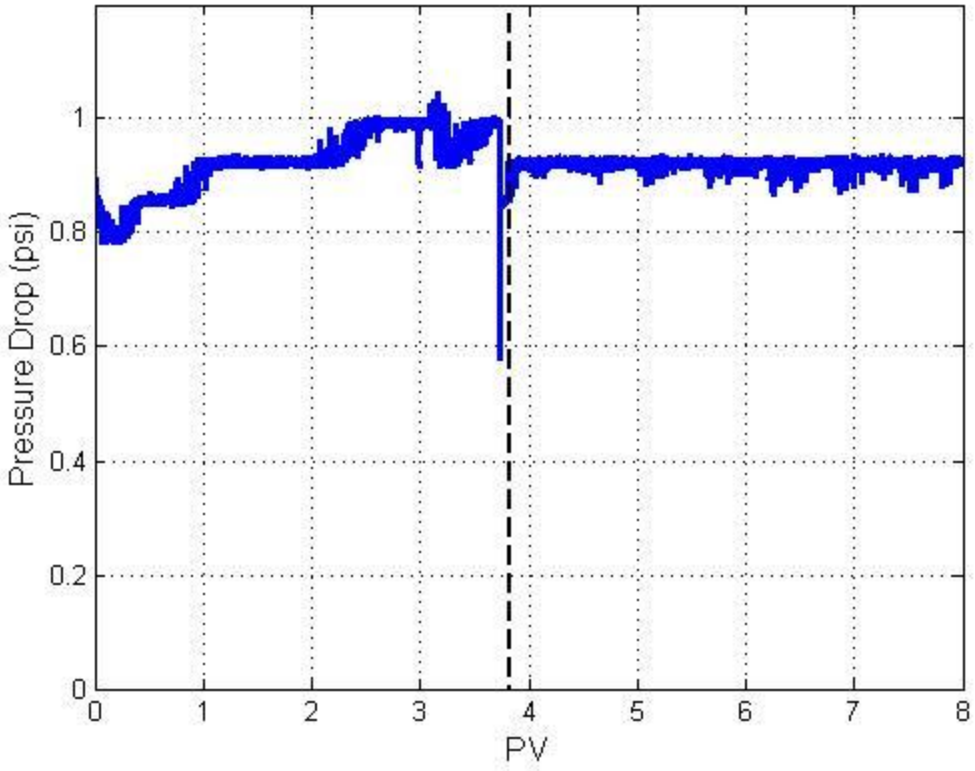

Figure 5.7: Measured pressure drop as a function of time for 3.81 PV injection of tracer and nanoparticle into Boise sandstone core for Exp. A1. Dashed line indicates the time when postflushing began.

After Exp. A1 is finished, the core was flushed with more than 10 PV's of 0.3 M NaCl solution to be used for the next experiment, Exp. A2. Conducting another experiment in the same core will allow us to test the transportability of nanoparticles in a porous medium whose irreversible adsorption capacities are already filled. Exp. A2 was carried out as a two-stage injection scheme. The first 2.2 PV slug contained 0.3 M NaCl and 0.4 wt% nanoparticle. The second 2.23 PV slug consisted of 0.3 M NaI and 1 wt% nanoparticle. This stage injection ensures the accuracy of calibration curve used for Exp. A1 and Exp. A2; if everything is calibrated correctly, the first slug should show no sign of tracer and the second slug should show both signals of tracer and nanoparticle.

Figure 5.8 shows the measured concentration history for the step injection experiment. The dashed line indicates arrival times of leading and trailing edges of an ideal tracer in the slugs of samples injected into the core. Effluent history during the first three PVs of injection shows only response from 0.4 wt% nanoparticle slug and no signal from tracer, meaning that the calibrations have been done correctly.

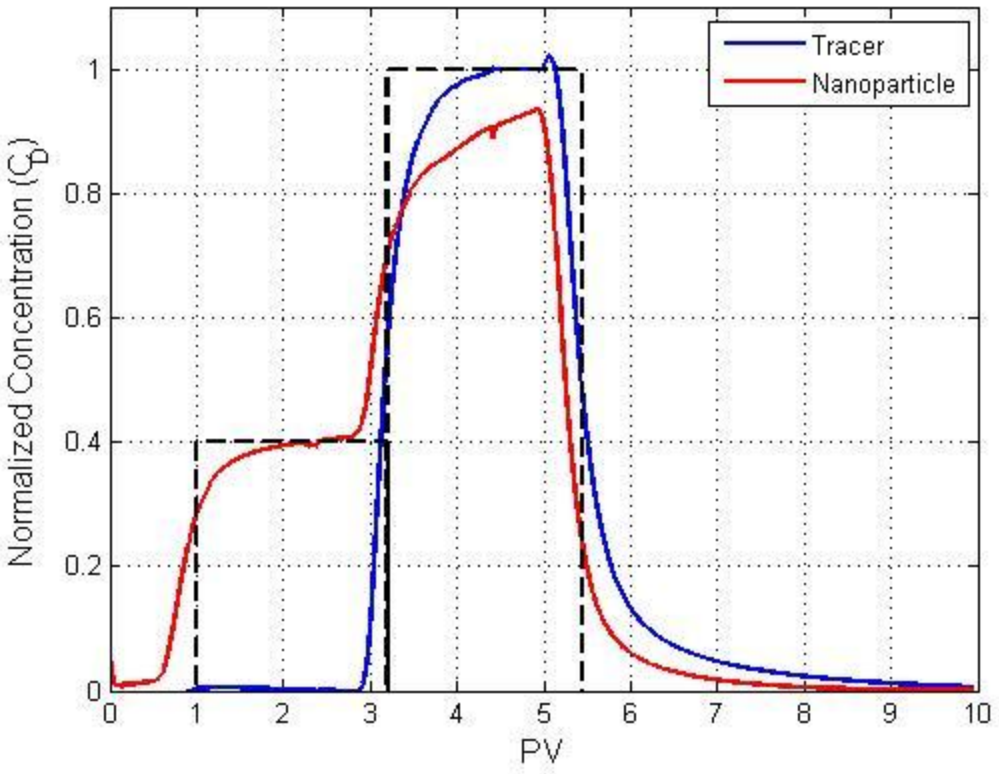

Figure 5.8: Measured concentration of tracer (blue) and nanoparticle (red) as a function of time for 2.2 PV injection of 0.3 M NaCl 0.4 wt% nanoparticle dispersion followed by 2.23 PV injection of 0.3 M NaI 1 wt% nanoparticle dispersion into Boise sandstone core for Exp. A2. Nanoparticle concentrations are normalized to the injected concentration of 1 wt%. Data appears as continuous lines because of very high frequency in-line acquisition. Dashed line indicates effluent concentration history for an ideal passive tracer that undergoes no dispersion.

Figure 5.9 shows the leading edge of the first slug injection of 0.3 M NaCl and 0.4 wt% nanoparticle. Nanoparticle reaches half of the injected concentration ($C_D = 0.2$) at 0.85 PV compared to 1 PV for a component that undergoes no interaction with the porous medium. This gap between the nanoparticle and the ideal tracer is greater than that observed in Exp. A1. Evidently in a porous medium whose irreversible capacity sites are already filled, injected nanoparticles underwent little interaction with the rock surface and the full extent of acceleration was apparent in the effluent concentration in the leading edge, whereas in Exp. A1, irreversible and reversible adsorptions counteracted the acceleration.

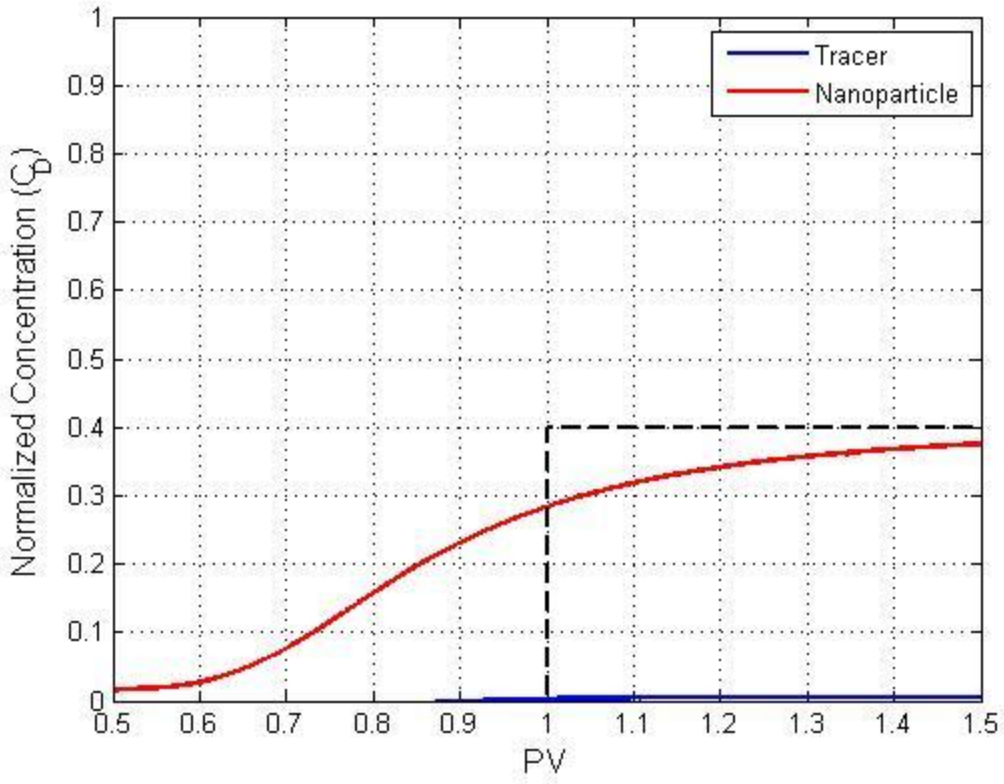

Figure 5.9: Leading edge of measured concentration of tracer (blue) and nanoparticle (red) as a function of time for 2.2 PV injection of 0.3 M NaCl 0.4 wt% nanoparticle dispersion followed by 2.23 PV injection of 0.3 M NaI 1 wt% nanoparticle dispersion into Boise sandstone core for Exp. A2. Nanoparticle concentrations are normalized to the injected concentration of 1 wt%. Data appear as continuous lines because of very high frequency in-line acquisition. Dashed line indicates effluent concentration history for an ideal passive tracer that undergoes no dispersion.

Figure 5.10 shows the leading edge of the second slug injection. For ease of comparison, a slight modification was made to the plot of the concentration profile of the nanoparticle. First, the time scale is adjusted to represent PV injection of the second slug; that is, PV^* is set to zero when the second slug enters the core. Second, the nanoparticle concentration axis was scaled to represent the concentration change from 0.4 wt% to 1

wt% as from C_D^* = 0 to C_D^* = 1 while the tracer concentration remained unchanged. The modification equation used was:

$$PV^* = PV - PV_{Slug2}$$

$$c^*_{D,nano} = \frac{1-0}{c_{D,nano,slug2} - c_{D,nano,slug1}}\left(c_D - c_{D,nano,slug1}\right)$$

$$c^*_{D,tracer} = c_{D,tracer}$$

where PV_{Slug2} is the PV when slug 2 was injected, $c_{D,nano,slug2}$ *i*s the dimensionless nanoparticle concentration in slug 2, $c_{D,nano,slug1}$ is the dimensionless nanoparticle concentration in slug 1, and $c_{D,tracer}$ is the dimensionless tracer concentration in slug 2.

Figure 5.10 shows a similar pattern as in Figure 5.5 in that nanoparticles arrive at the outlet of the core faster but the nanoparticle curve gets surpassed by the tracer curve due to adsorption of nanoparticles on rock surfaces.

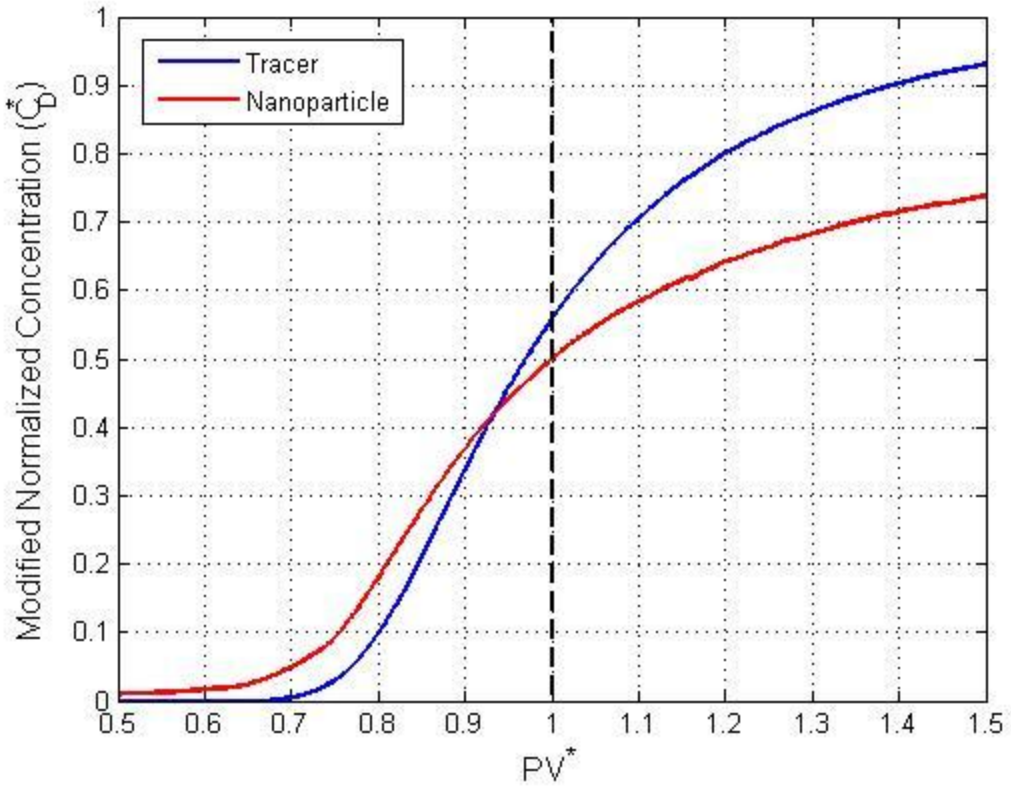

Figure 5.10: Leading edge of the modified concentration history of tracer (blue) and nanoparticle (red) for the second 2.23 PV slug injection of 0.3 M NaI, 1 wt% nanoparticle for Exp. A2. Nanoparticle concentrations are normalized to the injected concentration of 1 wt%. See text for definition of PV^* and C_D^* axis. Data appear as continuous lines because of very high frequency in-line acquisition. Dashed line indicates effluent concentration history for an ideal passive tracer that undergoes no dispersion.

Figure 5.11 shows the trailing edge of the unmodified concentration history curve. As seen before, the gap between tracer and nanoparticle curves is wider than for the leading edge. As discussed earlier, this widening is a manifestation of nanoparticles' full extent of enhanced transport due to filled adsorption sites.

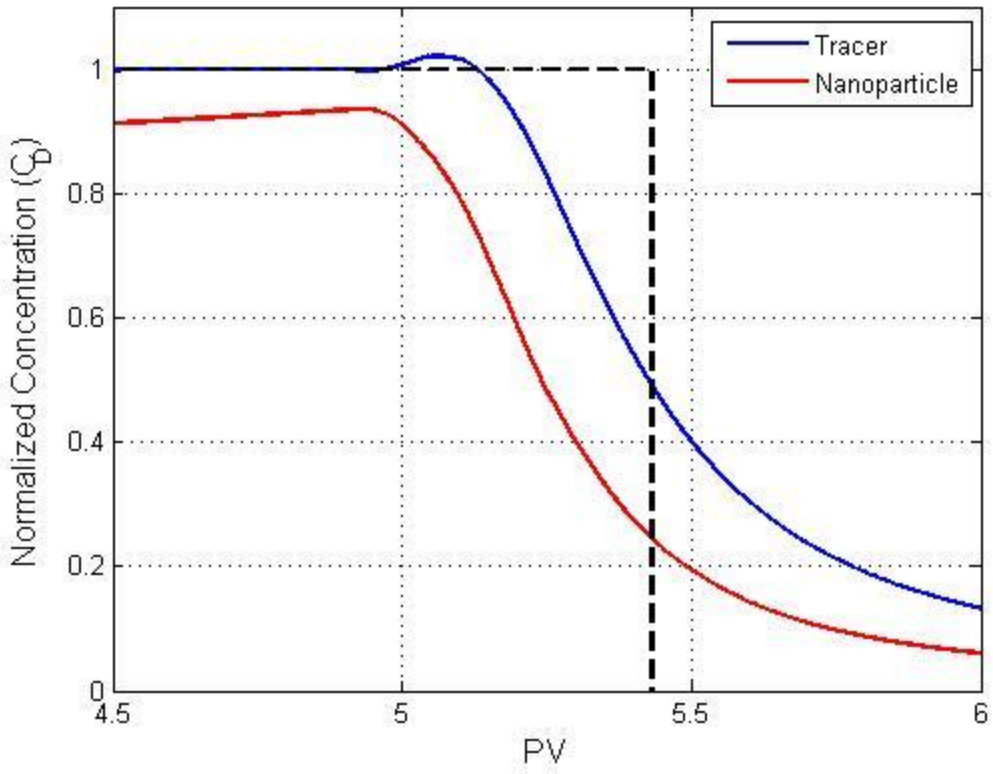

Figure 5.11: Trailing edge of measured concentration of tracer (blue) and nanoparticle (blue) as a function of time for 2.2 PV injection of 0.3 M NaCl 0.4 wt% nanoparticle dispersion followed by 2.23 PV injection of 0.3 M NaI 1 wt% nanoparticle dispersion into Boise sandstone core for Exp. A2. Nanoparticle concentrations are normalized to the injected concentration of 1 wt%. Data appear as continuous lines because of very high frequency in-line acquisition. Dashed line indicates effluent concentration history for an ideal passive tracer that undergoes no dispersion.

Berea Sandstone

Exp. A3 and Exp. A4 were carried out in a Berea sandstone core. Compared to the Boise core, Berea core was less permeable and looked more homogeneous from visual comparisons. Exp. A3 was a step injection experiment where the first 2.9 PV slug contained 0.3 M NaCl and 0.7 wt% nanoparticles and the second 4.4 PV slug contained 0.3 M NaI and 1.4 wt% nanoparticles.

Figure 5.12 shows the measured concentration history for the step injection into a Berea sandstone core. The dashed line indicates arrival times of leading and trailing edges of an ideal tracer in the slugs of samples injected into the core. It can be seen that the calibrations were correctly done as the curve confirms that the tracer concentration is zero for the first slug of injection. The shape of the leading edge tracer curve resembles an ideal classical advection-dispersion curve. The shape of the curve, as measured by UV-Vis detector, seems to be strongly influenced by heterogeneity of the core. That is, this experiment indicates that the Berea behaves like a classical homogeneous material, while the Boise core in Exp. A1 and Exp. A2 has internal heterogeneities that caused the tracer to deviate from classical error-function symmetry.

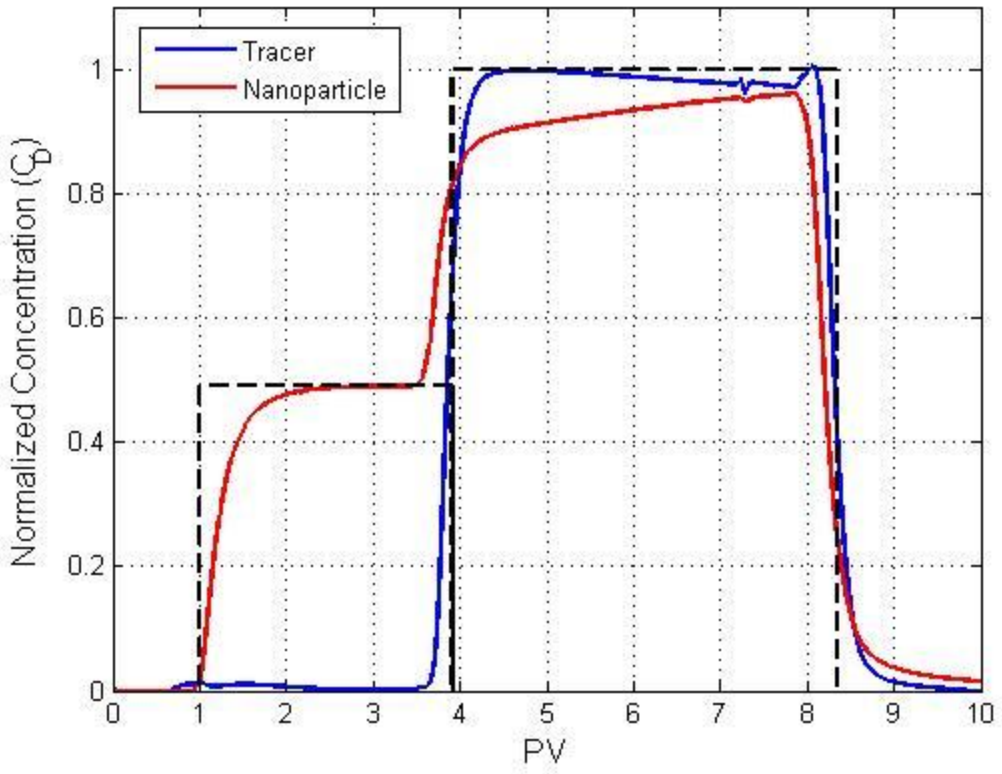

Figure 5.12: Measured concentration of tracer (blue) and nanoparticle (red) as a function of time for 2.9 PV injection of 0.3 M NaCl 0.7 wt% nanoparticle dispersion followed by 4.4 PV injection of 0.3 M NaI 1.4 wt% nanoparticle dispersion into Berea sandstone core for Exp. A3. Nanoparticle concentrations are normalized to the injected concentration of 1.4 wt%. Data appear as continuous lines because of very high frequency in-line acquisition. Dashed line indicates effluent concentration history for an ideal passive tracer that undergoes no dispersion.

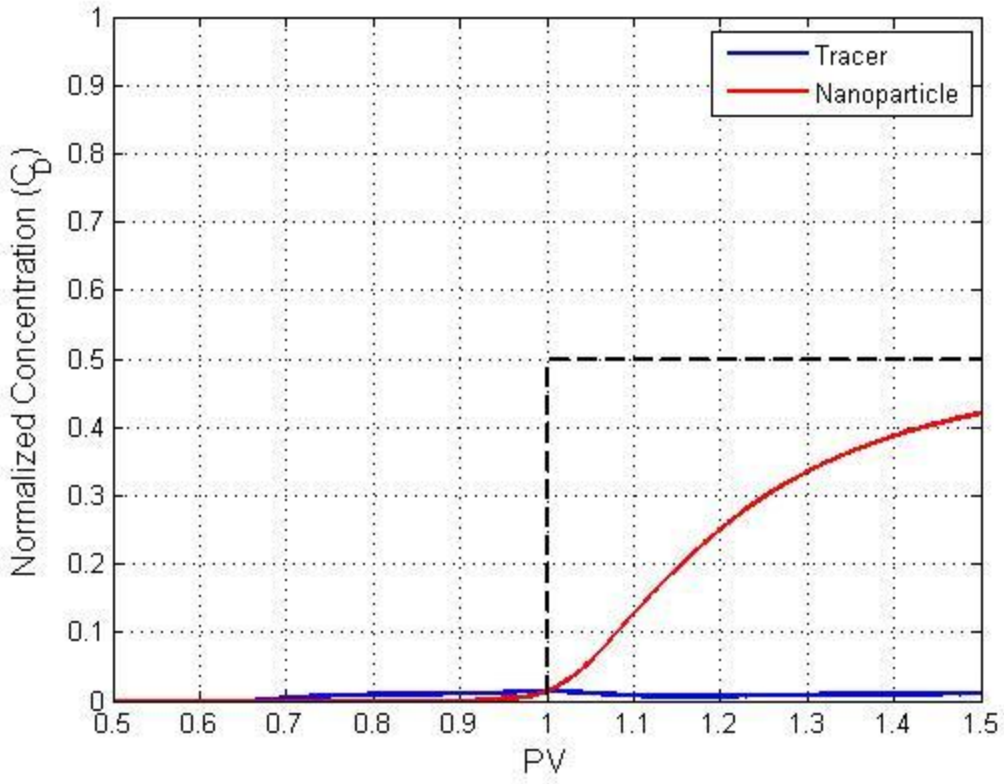

Figure 5.13: Leading edge of measured concentration of tracer (blue) and nanoparticle (red) as a function of time for 2.9 PV injection of 0.3 M NaCl 0.7 wt% nanoparticle dispersion followed by 4.4 PV injection of 0.3 M NaI 1.4 wt% nanoparticle dispersion into Berea sandstone core for Exp. A3. Nanoparticle concentrations are normalized to the injected concentration of 1.4 wt%. Data appear as continuous lines because of very high frequency in-line acquisition. Dashed line indicates effluent concentration history for an ideal passive tracer that undergoes no dispersion.

Figure 5.13 shows the leading edge of the first slug injection of 0.3 M NaCl and 0.7 wt% nanoparticle. Nanoparticle reaches half of the injected concentration (C_D = 0.25) at 1.2 PV compared to 1 PV for classical tracer. This delayed arrival of nanoparticle strongly attests to high adsorption of nanoparticles on Berea rock surface. Although the leading edge of the second slug injection shown in Figure 5.14 suggests that the

experiment was prone to inaccurate volume control, this should have been manifested as an early arrival of nanoparticles in Figure 5.13 to be consistent with the early arrival of the tracer during the second slug injection as shown in Figure 5.14. The nanoparticle concentration never reaches the injected concentration throughout the injection, indicating that there was ongoing nanoparticle adsorption on rock surfaces.

Figure 5.14 shows the leading edge of the second slug injection. For ease of comparison, the same modification was made to the concentration profile of the nanoparticle as in the Boise sandstone step-injection experiment. Figure 5.14 reveals that the additional concentration of nanoparticle introduced in the second slug sample broke through faster than the tracer. The fact that the second leading edge in Figure 5.14 shows an acceleration of nanoparticles while the first leading edge in Figure 5.13 does not is consistent with most of the adsorption sites having been filled during the first slug injection so that accelerated transport of nanoparticles becomes a more dominant mechanism than adsorption. However, the decrease in the shoulder curvature suggests that nanoparticles still underwent adsorption; slug of higher nanoparticle concentration leads to higher nanoparticle retention because adsorption rate is proportional to the nanoparticle concentration (Murphy, 2012; Zhang, 2012). The tracer also arrives earlier than an ideal passive tracer indicated by the dashed line. The early arrival of the tracer (C_D = 0.5 arriving at PV = 0.94) suggests that the volume control during the experiment was not accurate. The procedural step of estimating the pore volume based on the difference between the dry weight and the wet weight leads to an approximate error of ± 0.04 PV, calculated by dividing the sensitivity of the scale (1 g) by the difference between the wet weight and the dry weight (27 g). In addition, this method does not allow us to distinguish the difference between the effective pore volume and dead-end pore

volume. However these volume control errors do not affect the relative velocities of the tracer and the nanoparticles.

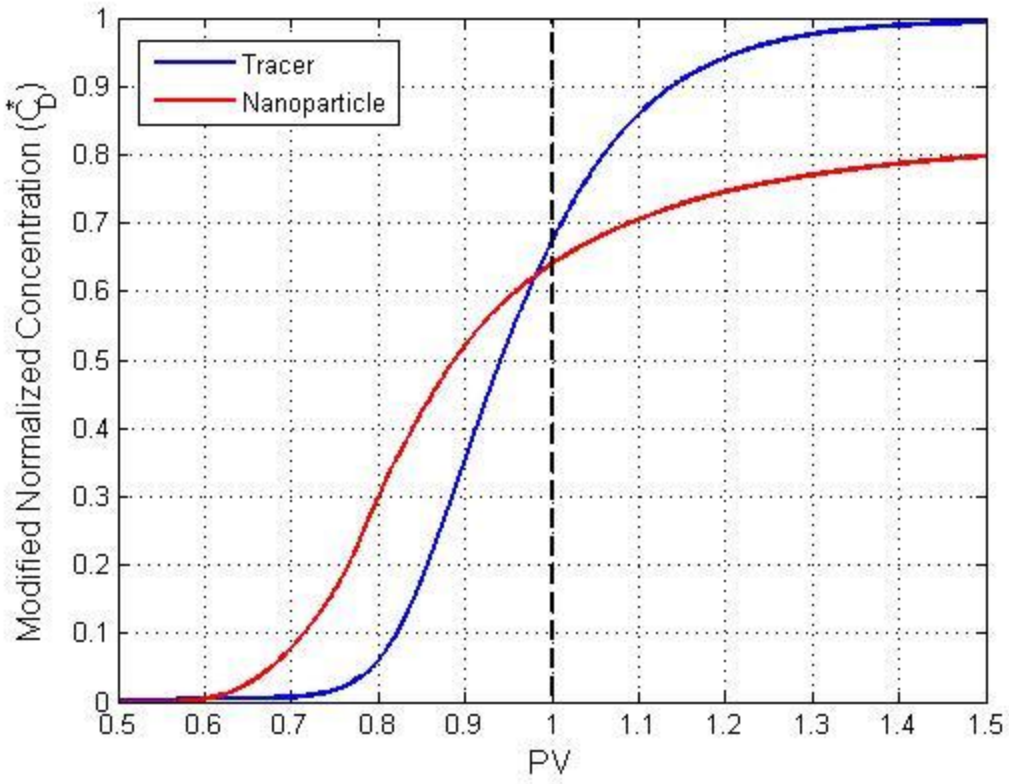

Figure 5.14: Leading edge of the modified concentration history of tracer (blue) and nanoparticle (red) for the second 2.9 PV slug injection of 0.3 M NaI, 1.4 wt% nanoparticles for Exp. A3. Nanoparticle concentrations are normalized to the injected concentration of 1.4 wt%. See page 92 for definition of PV^* and C_D^* axis. Data appear as continuous lines because of very high frequency in-line acquisition. Dashed line indicates effluent concentration history for an ideal passive tracer that undergoes no dispersion.

Figure 5.15 shows the trailing edge of the unmodified concentration history curve. As seen before, the gap between the tracer and nanoparticle curves in the trailing edge is wider than the one in the leading edge. This widening, again, is due to adsorption sites being filled as the slug is injected, leading to the full extent of nanoparticles' accelerated transport being apparent in the trailing edge of the slug. Compared to the tracer, the nanoparticle curve exhibits a longer tail, which is characteristic of desorption process of nanoparticles reversibly attached to the rock surface (Murphy, 2012; Zhang, 2012).

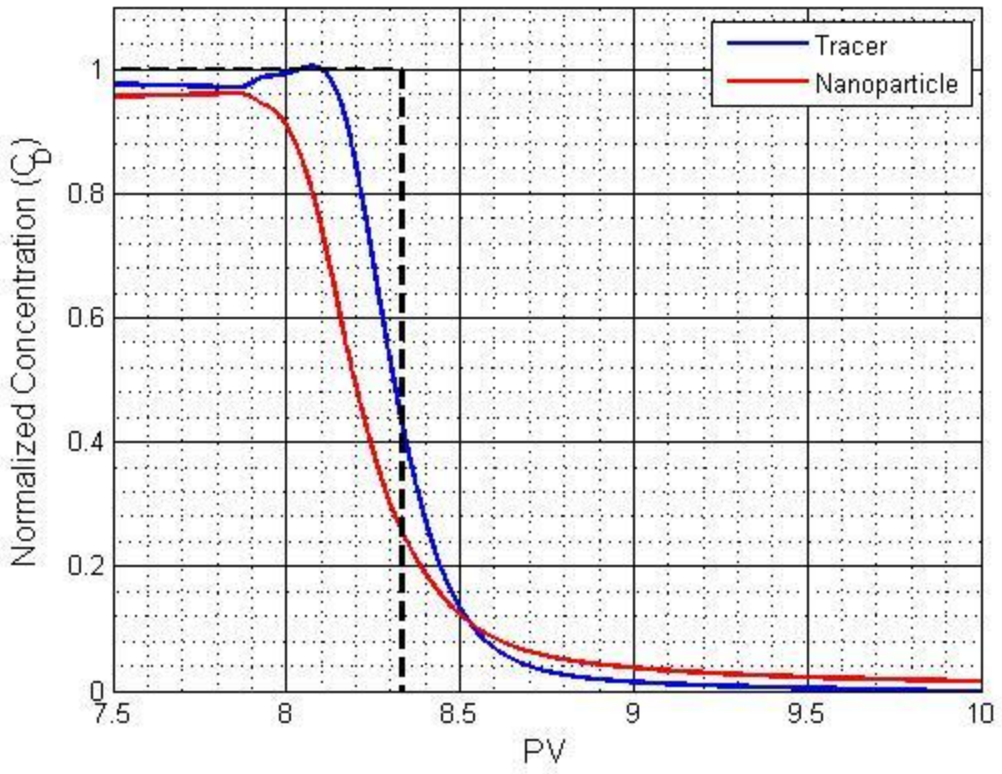

Figure 5.15: Trailing edge of measured concentration of tracer (blue) and nanoparticle (red) as a function of time for 2.9 PV injection of 0.3 M NaCl 0.7 wt% nanoparticle dispersion followed by 4.4 PV injection of 0.3 M NaI 1.4 wt% nanoparticle dispersion into Berea sandstone core for Exp. A3. Nanoparticle concentrations are normalized to the injected concentration of 1.4 wt%. Data appear as continuous lines because of very high frequency in-line acquisition. Dashed line indicates effluent concentration history for an ideal passive tracer that undergoes no dispersion.

After Exp. A3 was finished, the core was flushed with more than 10 PV's of 0.3 M NaCl solution at 1 mL/min so the core can be used for the next experiment, Exp. A4. Conducting another experiment in the same core will allow us to test the transportability of nanoparticles in a porous media whose irreversible adsorption capacities are already filled. In Exp. A4, 9.88 PV of nanoparticle and tracer slug (0.3 M NaI, 1 wt% NP) was injected into the core, followed by post-flushing with 0.3 M NaCl brine.

Figure 5.16 shows the effluent concentration history of tracer and nanoparticle as a function of time. The dashed box indicates the size of the sample slug injected into the core and when the leading and trailing edges of the slug would arrive in the effluent if the injected components underwent no interaction with the porous medium. Both concentrations of the tracer and nanoparticles are normalized by the respective injected concentration. If the tracer had undergone only dispersion and no interaction with the porous media, the effluent concentration curve should be a superposition of a positive error function symmetric about (PV = 1, C_D = 0.5) and a negative error function symmetric about (PV = 10.9, C_D = 0.5). As can be seen in Figure 5.7, the measured tracer curve can be fitted with the infinite-core solution with a Peclet number of 66.1.

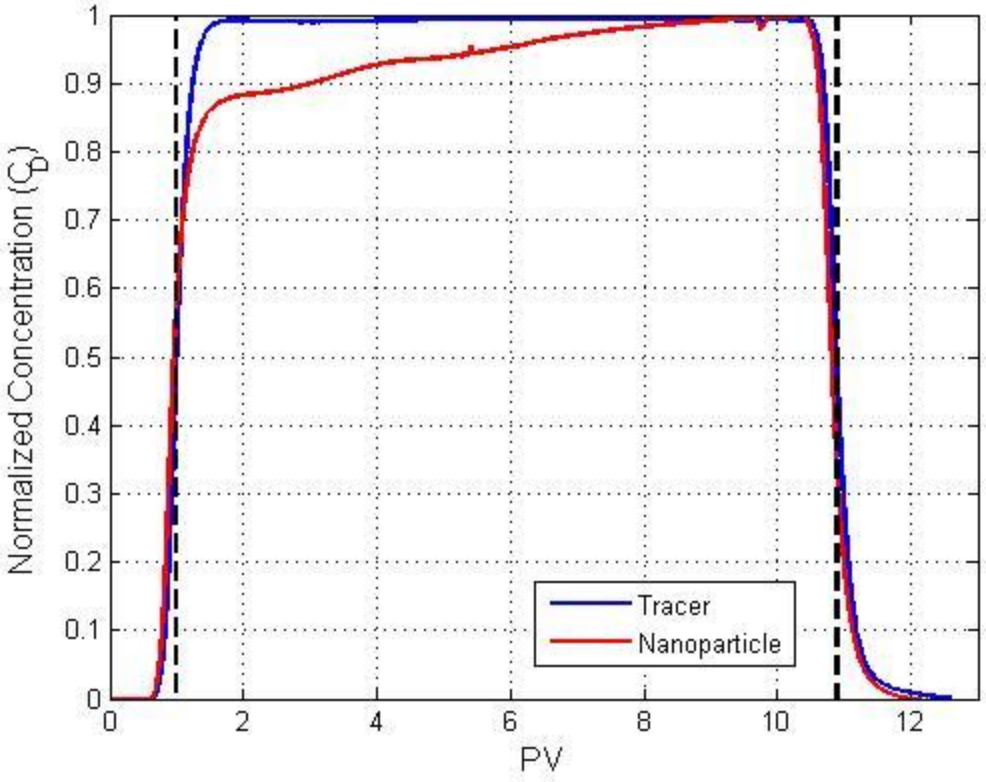

Figure 5.16: Measured concentration of tracer (blue) and nanoparticle (red) as a function of time for 9.88 PV injection of tracer and nanoparticle into Berea sandstone core for Exp. A4. Nanoparticle concentrations are normalized to the injected concentration of 1 wt%. Data appear as continuous lines because of very high frequency in-line acquisition. Dashed line indicates effluent concentration history for an ideal passive tracer that undergoes no dispersion.

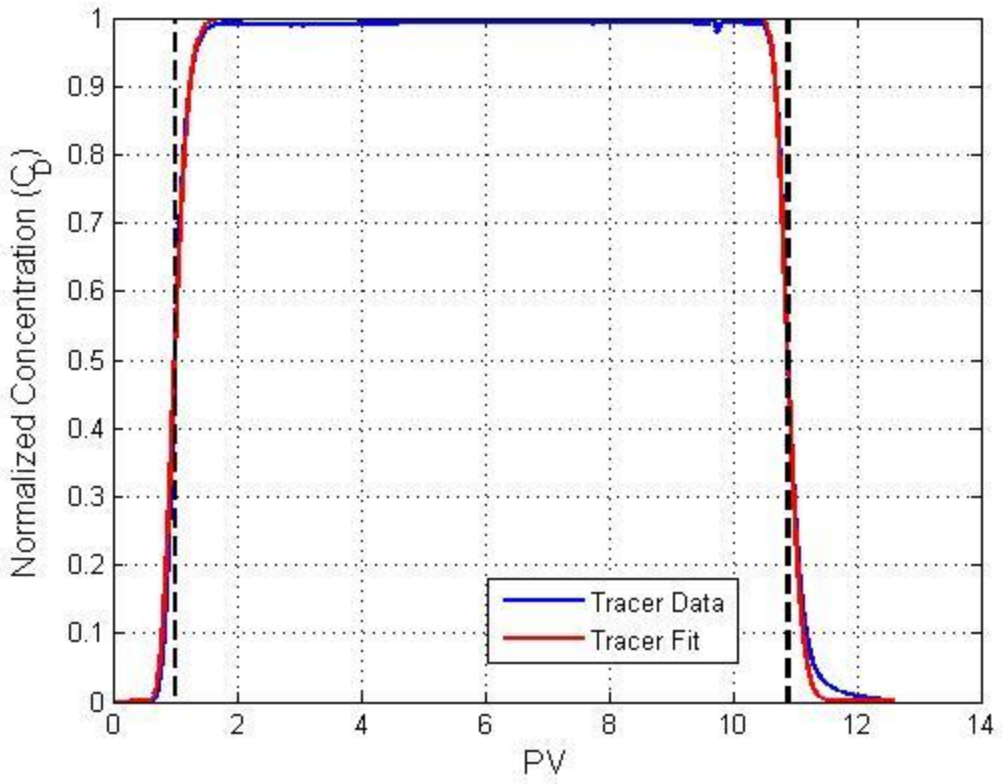

Figure 5.17: Measured concentration of tracer as a function of time (blue) and fitted classical tracer curve with N_P = 66.1 (red) for 9.88 PV injection of tracer and nanoparticle into Berea sandstone core for Exp. A4. Data appear as continuous lines because of very high frequency in-line acquisition. Dashed line indicates effluent concentration history for an ideal passive tracer that undergoes no dispersion.

Figure 5.18 is a magnified view of the leading edge of the curve and shows that nanoparticles arrived at the detector faster than the tracer did. However, the nanoparticle curve is surpassed by the tracer curve at 1.1 PV because nanoparticles undergo some retention in the porous media. As observed in experimental works by Yu (2012) and Murphy (2012), this slower increase in the effluent concentration at the shoulder is characteristics of fast adsorption and slow desorption of nanoparticles on rock surfaces (Zhang, 2012).

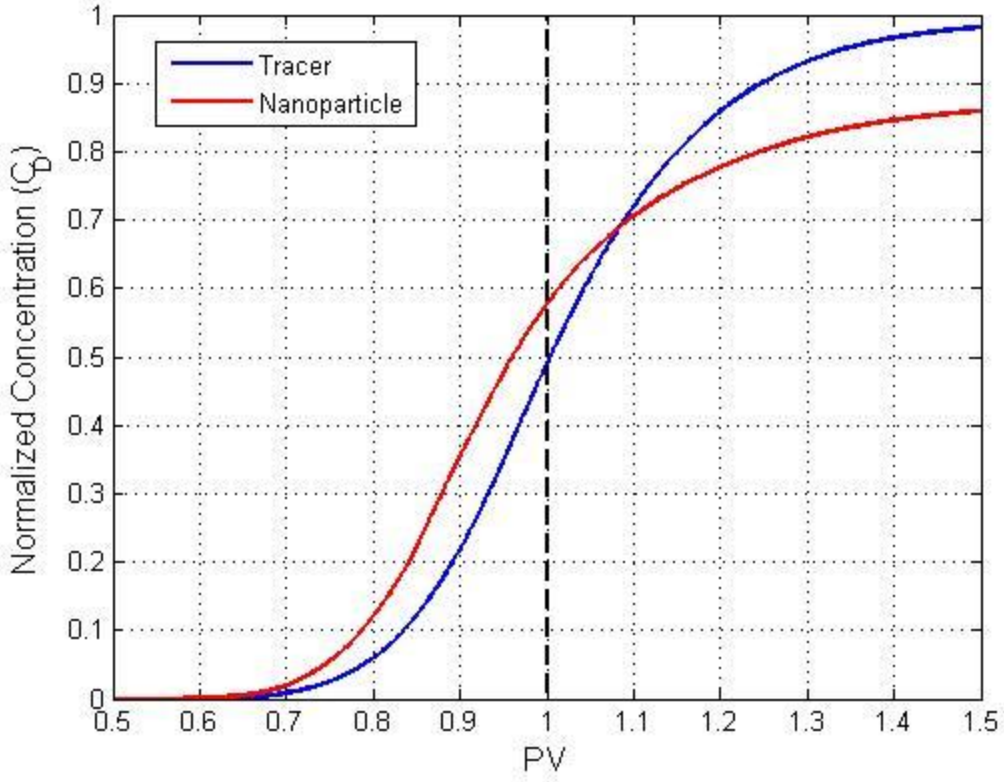

Figure 5.18: Leading edge of measured concentration of tracer (blue) and nanoparticle (red) as a function of time for 9.88 PV injection of tracer and nanoparticle into Berea sandstone core for Exp. A4. Nanoparticle concentrations are normalized to the injected concentration of 1 wt%. Data appear as continuous lines because of very high frequency in-line acquisition. Dashed line indicates effluent concentration history for an ideal passive tracer that undergoes no dispersion.

In Exp. A3 when a slug of nanoparticle was introduced in a fresh Berea sandstone core, the effluent history showed a delay in nanoparticle arrival at the end of the core. In Exp. A4, nanoparticles arrive faster than the tracer because the irreversible adsorption sites of the core had already been filled. Integrating the effluent concentration curves and comparing the recovered PV's suggest that the retention amount was 5.4% in Exp. A4.

Figure 5.19 shows the magnified view of the trailing edge of the measured concentration history. At the trailing edge, the gap between the tracer and nanoparticle is the same as the one observed in the leading edge.

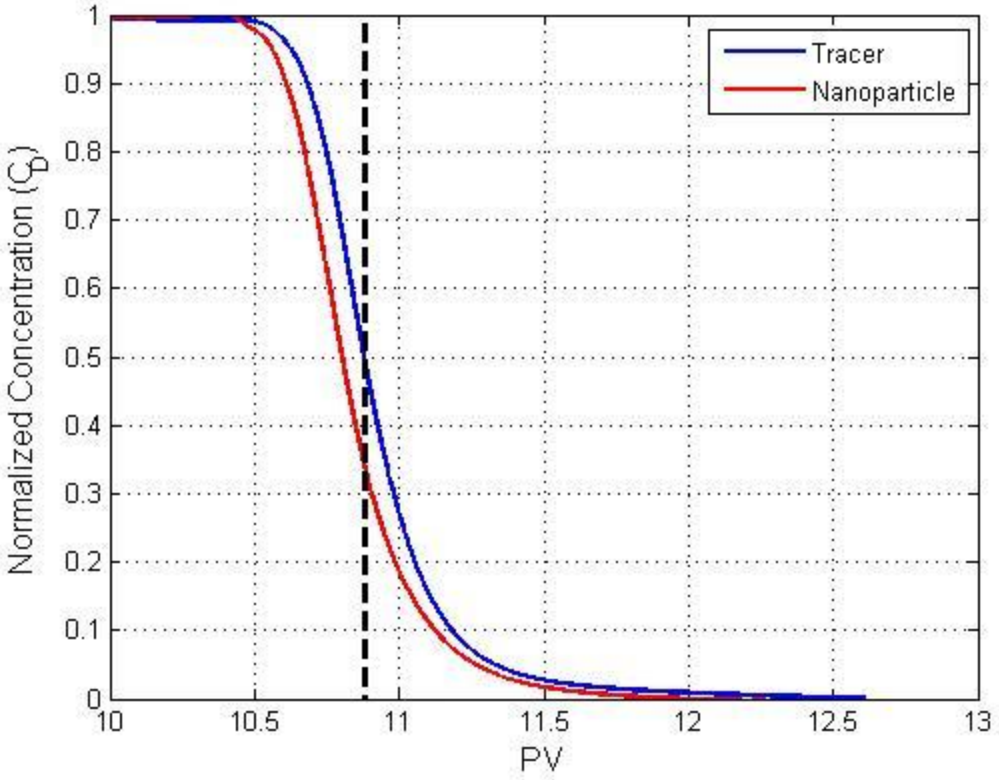

Figure 5.19: Trailing edge of measured concentration of tracer (blue) and nanoparticle (red) as a function of time for 9.88 PV injection of tracer and nanoparticle into Berea sandstone core for Exp. A4. Nanoparticle concentrations are normalized to the injected concentration of 1 wt%. Data appears as continuous lines because of very high frequency in-line acquisition. Dashed line indicates effluent concentration history for an ideal passive tracer that undergoes no dispersion.

Two-Site Model Fit

The two-site model, described in Chapter 2, represents nanoparticles' interactions with porous media as two separate sets of adsorption sites, one for irreversible adsorption and the other for reversible adsorption. However, the model does not account for the enhanced mobility of nanoparticles that was observed in the experimental studies presented in Chapter 4 and earlier in this chapter. By fitting the model to the data, we can evaluate what kind and how much adsorption was taking place during the experiment and the effects of the adsorption on the breakthrough curves predicted by the two-site model. Integrating all this information will lead us to either strengthen or refute the argument for accelerated transport of nanoparticles. In particular, we will test the alternative explanation that the earlier arrival of nanoparticles can be attributed to larger dispersivity for particles than for tracer ions.

Of the four experiments conducted, results of Exp. A4 are the most conducive to study with the two-site model; resemblance of Exp. A4's tracer effluent history to the classical shape of an non-interactive component suggests that the general flow pattern in the Berea sandstone core is the extensively studied and well-established advection with Fickian dispersion. Exp. A1's non-classical tracer curve may be an indication of internal heterogeneity of the core affecting the transport of both tracer and nanoparticle, and there are difficulties with modeling the step-changes in injected concentrations (Exp. A2 and Exp. A3); for example, experimental results by Murphy (2012) suggest that retention for Nyacol's DP9711 nanoparticles increases as the injected concentration increases while the two-site model by Zhang (2012) predicts just the opposite.

Before fitting the model to the experimental nanoparticle data, a fit to the tracer data was done to obtain a Peclet number. Tracer that undergoes no adsorption can be numerically modeled with a finite-core boundary condition by setting the adsorption rates

to zero ($M_3 = 0$, $M_4 = 0$, $M_5 = 0$) in the two-site model. Adsorption site capacities (M_1 and M_2) were arbitrarily set to 1×10^{-20}. It should be noted that the value of Peclet number obtained in this manner differs from the classical infinite-core model prediction shown in Figure 5.17. This is because the computational model assumes a finite-length core (Mennella et al., 1999). As a result, Peclet number in the model affects the tracer breakthrough curves differently than it does in the analytical solution, shown in Figure 5.20.

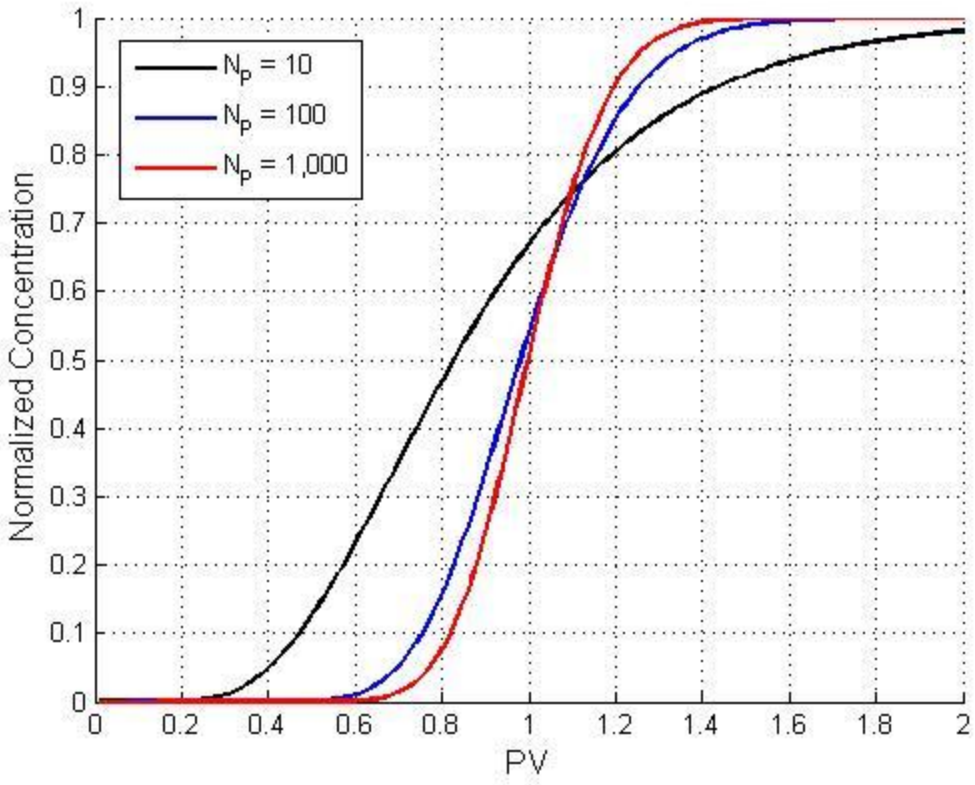

Figure 5.20: Simulated tracer effluent history curve for different Peclet numbers using finite-core boundary conditions. Behavior differs from the classical error function solution which assumes an infinite-length core (Mennella et al., 1999).

The model predicts that the tracer with a lower Peclet number breaks through earlier than the one with a higher Peclet number. There is also an absence of the symmetry point ($C_D = 0.5$ at PV = 1) that is found in analytical solutions of infinite-core convection-dispersion equation with different Peclet numbers. Therefore, it becomes imperative to do another fit for the tracer with the computational finite-core model because using a low Peclet number, i.e. obtained from the infinite-core solution, will result in an early breakthrough of the injected concentration, which can be misinterpreted as acceleration.

Optimization was done by minimizing the sum of the squares of the difference between each sampled data point and the model prediction. A Peclet number of 285 was necessary to fit the tracer data for Exp. A4. In order to show the experimental data as discrete points instead of a continuous curve (because of high-frequency data acquisition), the experimental data were sampled every 0.1 PV. Figure 5.21 through Figure 5.23 shows the effluent concentration history fitted by the two-site model to the dotted experimental data for the tracer.

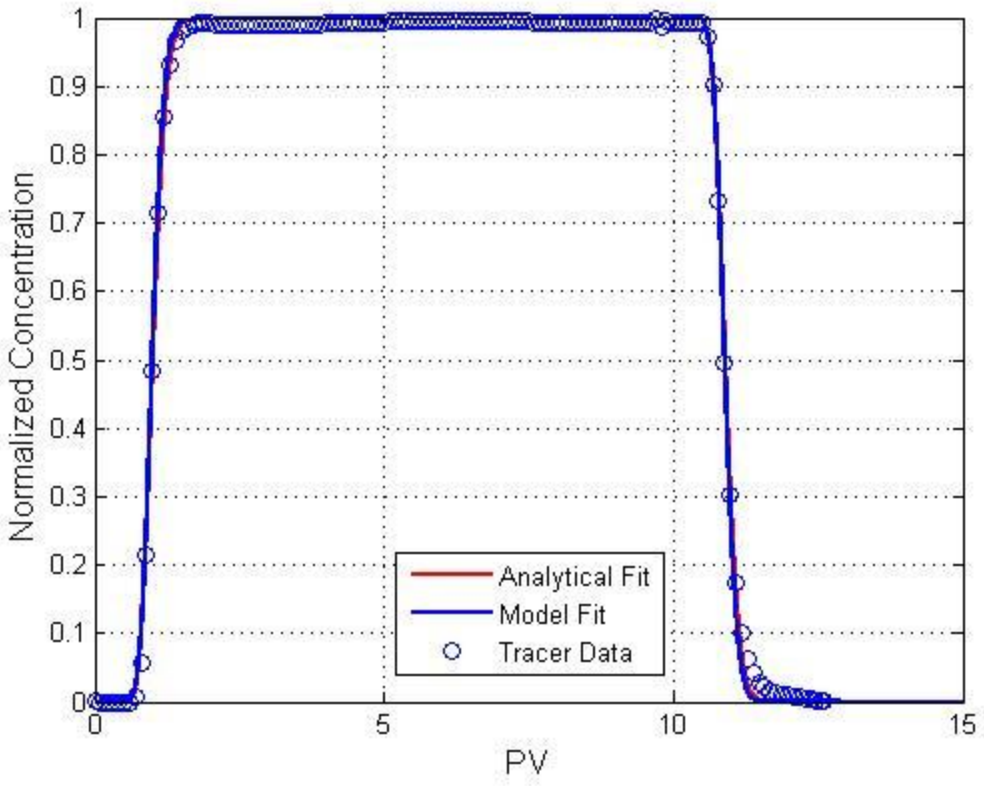

Figure 5.21: Experimental (circles), analytical error function solution (red curve), and finite-core model fitted (blue curve) effluent histories for 9.88 PV injection of tracer and nanoparticle into Berea sandstone core for Exp. A4. N_P for analytical fit is 66.1 and for the finite-core model 285.

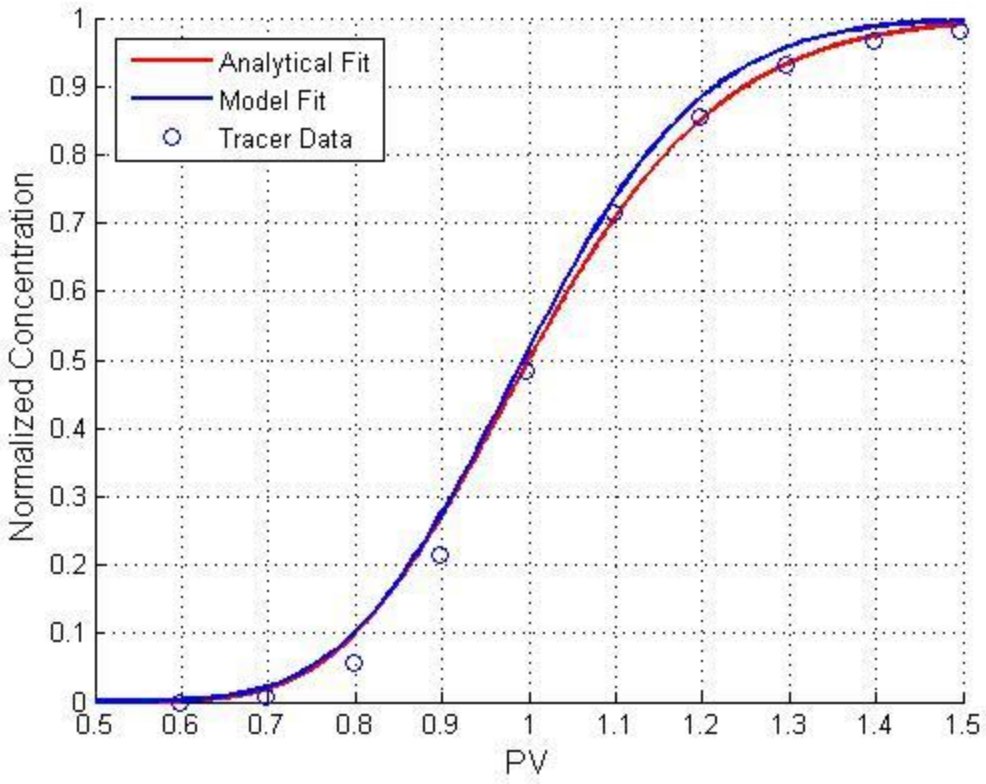

Figure 5.22: Leading edge of experimental (circles), analytical error function solution (red curve), and finite-core model fitted (blue curve) effluent histories for 9.88 PV injection of tracer and nanoparticle into Berea sandstone core for Exp. A4. N_P for analytical fit is 66.1 and for the finite-core model 285.

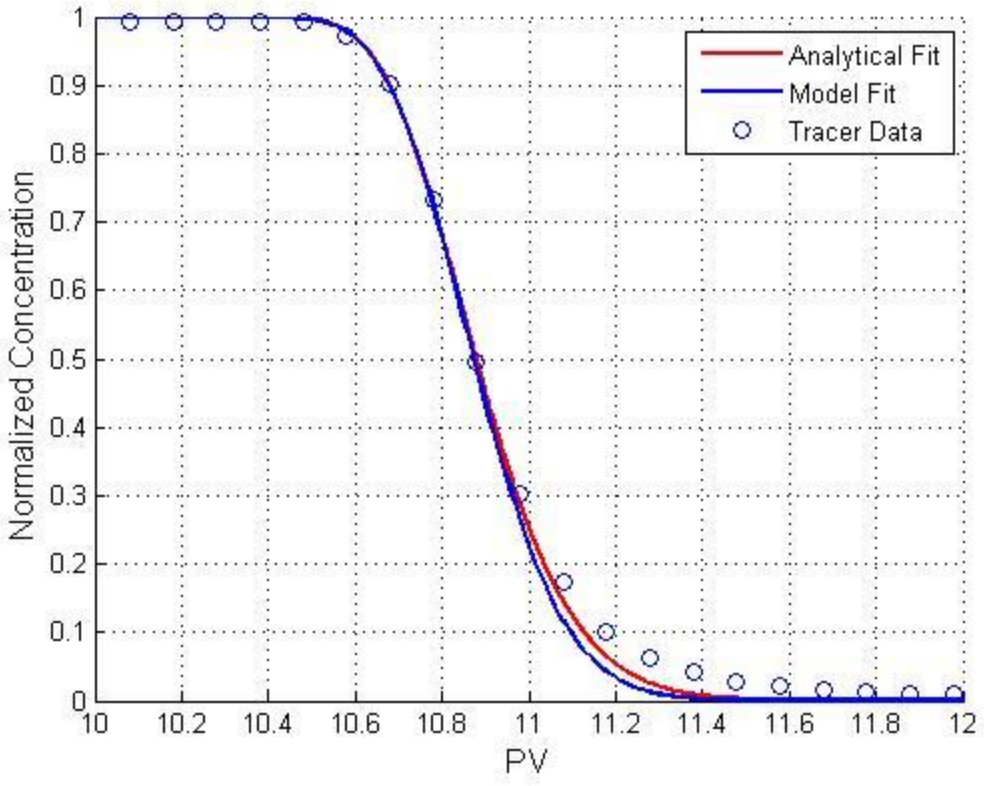

Figure 5.23: Trailing edge of experimental (circles), analytical error function solution (red curve), and two-site model fitted (blue curve) effluent histories for 9.88 PV injection of tracer and nanoparticle into Berea sandstone core for Exp. A4. N_P for analytical fit is 66.1 and for the two-site model 285.

The tracer fit by the finite-core model (obtained by setting $M_1 = 1\times10^{-20}$, $M_2 = 1\times10^{-20}$, $M_3 = 0$, $M_4 = 0$, $M_5 = 0$ in the two-site model) aligns well with the analytical solution and experimental data except for the first couple points in the leading edge and last several points in the trailing edge. The discrepancies indicate that other processes such as non-Fickian dispersion or dead-end pores are influencing the tracer transport, but those processes are ignored for the purpose of this study.

After the tracer fit, the two-site model was fitted to the nanoparticle concentration history data from Exp. A4. Because the information about the adsorption and desorption

processes are conveyed in the shoulder portion of the effluent history (Murphy, 2012; Zhang, 2012), the adsorption site capacities and rates (M_1, M_2, M_3, and M_4) were adjusted to generate a best-fitting curve to the shoulder portion of the experimental data. The Peclet number was held at 285, i.e. obtained from the tracer fit above. These fitted parameters are summarized in Table 5.2.

Dimensional		Dimensionless	
D, m^2/s	1.17×10^{-7}	N_P	285
S_{1max}, g/g	4.95×10^{-3}	M_1	0.60
S_{2max}, g/g	3.14×10^{-2}	M_2	3.81
k_{irr}, 1/s	5.81×10^{-5}	M_3	0.16
k_{ra}, 1/s	5.58×10^{-6}	M_4	0.016
k_{rd}, 1/s	1.91×10^{-2}	M_5	202

Table 5.2: Fitted parameters in the two-site model for the nanoparticle effluent history from Exp. A4, assuming same dispersion coefficient for nanoparticles as for tracer.

The values for the adsorption site capacities were not the same as those in Zhang (2012) for transport of Nyacol DP nanoparticles through a sand pack of crushed Boise sandstone at a velocity ranging from 100 ft/day to 1000 ft/day and an injected concentration of 1.5 to 5 wt%; the fitted S_{1max} in this work was 4.95×10^{-3} g/g and S_{2max} was 3.14×10^{-2} g/g while Zhang (20120 reported values of 1.65×10^{-3} g/g and 3.14×10^{-2} g/g. Considering that Zhang (2012) reported site capacities values ranging from 10^{-4} to 10^{-1} for experimentations done for flow of different nanoparticles through a pack of glass beads or crushed Boise sandstone, this difference is not considered to be significant.

Figure 5.24 through Figure 5.26 show experimental (circles) and simulated effluent histories (curves) for the tracer and nanoparticles as a function of time.

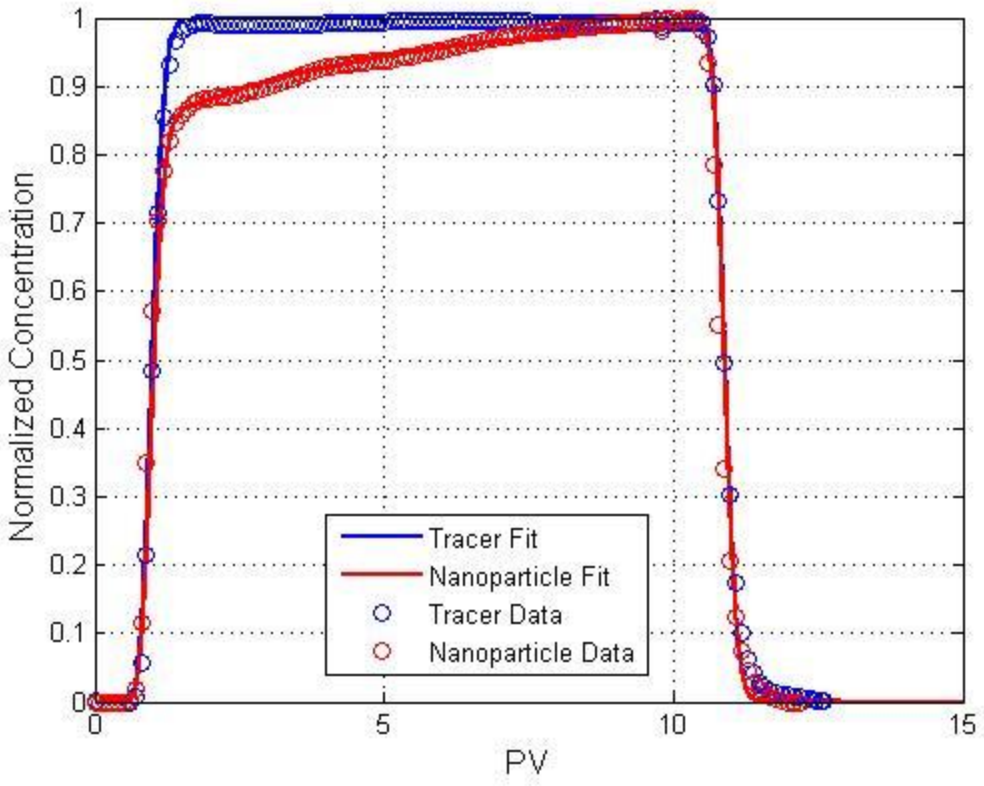

Figure 5.24: Experimental (circles) and simulated effluent histories (curves) by the two-site model for 9.88 PV injection of tracer and nanoparticle into Berea sandstone core for Exp. A4. The fitted parameters are summarized in Table 5.2.

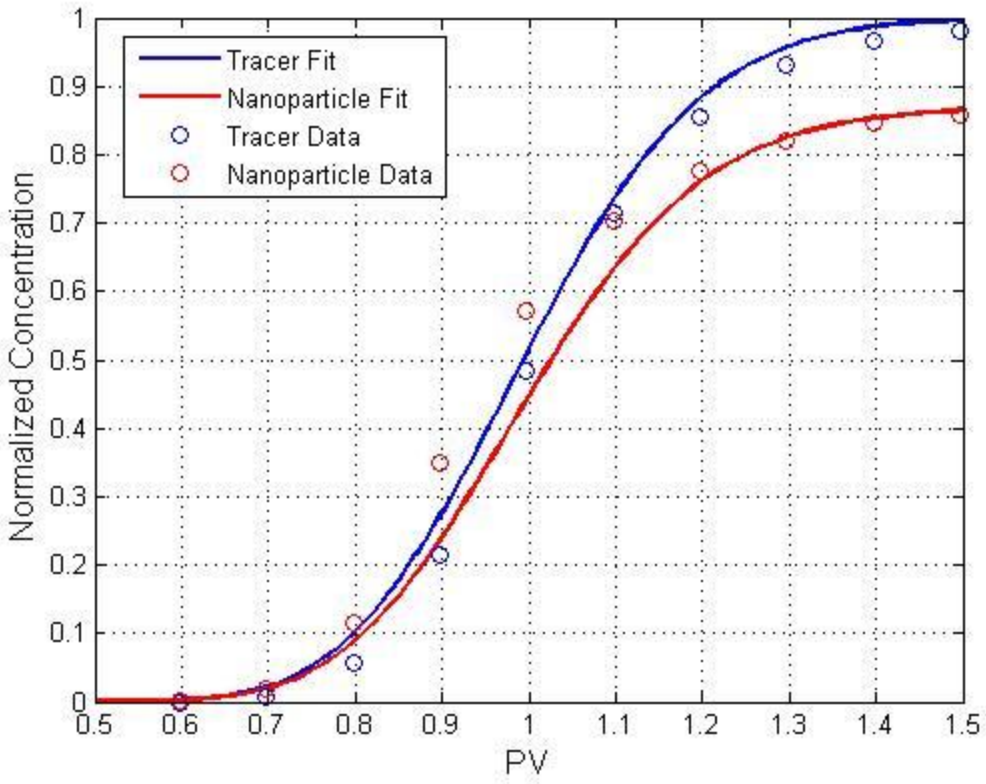

Figure 5.25: Leading edge of the experimental (circles) and simulated (curves) effluent histories by the two-site model for 9.88 PV injection of tracer and nanoparticle into Berea sandstone core for Exp. A4. The fitted parameters are summarized in Table 5.2.

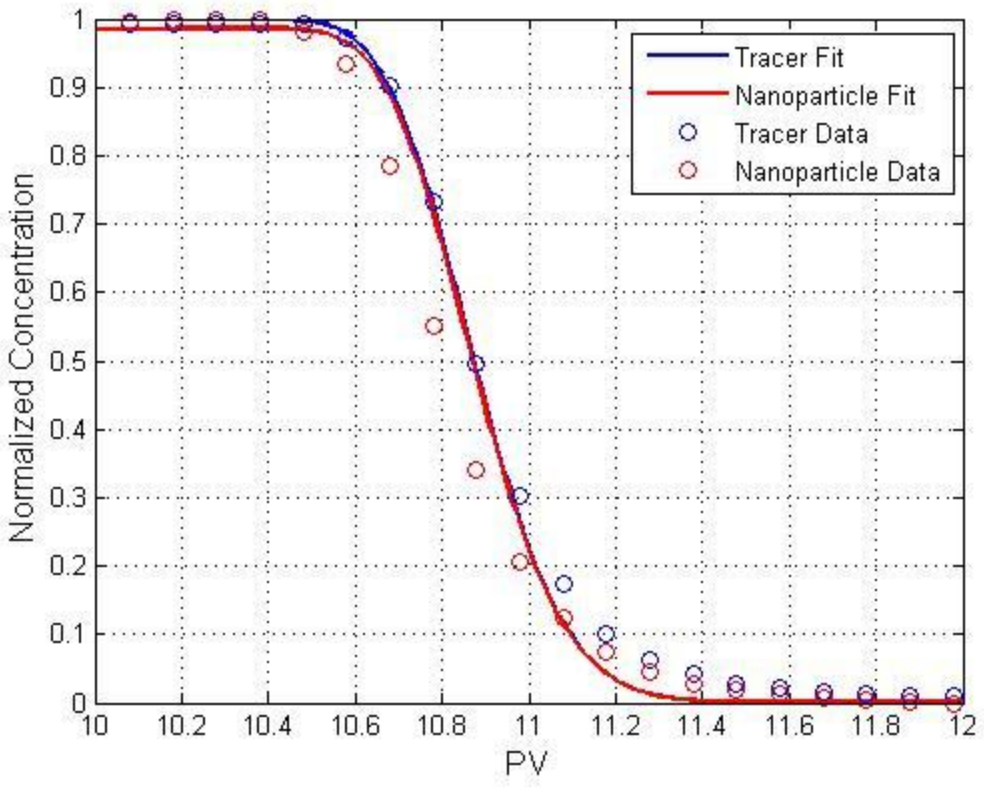

Figure 5.26: Trailing edge of the experimental (circles) and simulated (curves) effluent histories by the two-site model for 9.88 PV injection of tracer and nanoparticle into Berea sandstone core for Exp. A4. The fitted parameters are summarized in Table 5.2.

Figure 5.24 shows that although the two-site model prediction retains the overall shape close to the experimental effluent history, the model is not able to accurately predict all of the characteristic features of the curve, especially in the leading edge and the trailing edge. The irreversible adsorption rate was faster than the reversible adsorption rate by ten times (compared M_3 and M_4 in Table 5.2) and irreversible adsorption led to an overall nanoparticle retention of 5% in the core after postflushing finished. The low irreversible adsorption capacity is reasonable given that the irreversible sites are already

filled during the previous step-injection experiment (Exp. A3). The big contrast between the reversible adsorption rate and the desorption rate suggests that any nanoparticles that are reversibly adsorbed on the rock surface stay retained for only a very short period of time.

The fitted curves between the tracer and the nanoparticle also do not overlap in the leading edge; adsorption leads to an obvious delay in the simulated nanoparticle concentration in the leading edge. Most of the nanoparticle retention (irreversible adsorption) happens in the shoulder portion of the curve and once all the available sites are filled, the nanoparticle curve converges to the tracer curve. Consequently the model fit does not capture the early arrival of intermediate nanoparticle concentrations (between 0.2 and 0.8).

To the contrary, the trailing edge of the model fit does not show any difference in the simulated nanoparticle and tracer curves, because the fit drove the rate of reversible adsorption to nearly zero. Even so, the fit fails to capture the earlier arrival of intermediate nanoparticle concentrations (between 0.2 and 0.8). The absence of reversibly attached nanoparticles minimizes the long tail in the trailing edge of the slug. Such tails were commonly observed in experimental works by Murphy (2012).

Figure 5.25 and Figure 5.26 both show a gap between the observed and simulated effluent nanoparticle concentrations at the leading edge and the trailing edge. We attribute this difference to the accelerated transport of nanoparticles. Figure 5.25 shows the combined effect of adsorption and acceleration on the measured breakthrough curve of the nanoparticles. The two-site model accounts only for adsorption. The adsorption process delays the arrival of nanoparticles at the outlet; if nanoparticles had no interaction with porous media like the tracer, they would have appeared at the same time as the tracer, and no shoulder would have occurred after breakthrough. The adsorption process

results in the model nanoparticle curve arriving later than the model tracer curve. In contrast to the model, experimental data show that nanoparticles appeared even faster than the tracer. Therefore, the two processes—adsorption and acceleration—seem to work against each other in the leading edge; adsorption delays the breakthrough curve and acceleration advances the breakthrough curve. Despite the retardation that would be induced by adsorption, nanoparticles still arrive at the outlet of the core faster than the tracer, and this observation is strong evidence for the enhanced transport of nanoparticles.

In the trailing edge, the model predicts no difference between the tracer and the nanoparticle curves. Instead, the experiment showed that nanoparticles arrive earlier than the tracer and earlier than the two-site model's prediction.

However, considering the hypothesized mechanism for acceleration, viz. that nanoparticles have access to a smaller fractions of pore space in the core than the tracer, it may not be correct to assume the same Peclet number for the tracer and the nanoparticle, although doing so was a convenient starting point. Therefore, the two-site model fit to the nanoparticle effluent history was repeated, this time varying all parameters including the Peclet number. The optimization was initialized with the parameter values in Table 5.2. The new fitted parameters are shown in Table 5.3.

Dimensional		Dimensionless	
D, m^2/s	4.91×10^{-7}	N_P	68
S_{1max}, g/g	4.95×10^{-3}	M_1	0.60
S_{2max}, g/g	3.14×10^{-2}	M_2	3.81
k_{irr}, 1/s	3.96×10^{-5}	M_3	0.11
k_{ra}, 1/s	0	M_4	0
k_{rd}, 1/s	1.89×10^{-2}	M_5	201

Table 5.3: Fitted parameters including the Peclet number in the two-site model for the nanoparticle effluent history from Exp. A4, allowing different dispersion coefficients for nanoparticle and tracer.

The optimization scheme of minimizing the error between the experimental data and the corresponding model prediction led to a simulated effluent history shown in Figure 5.27 through Figure 5.29.

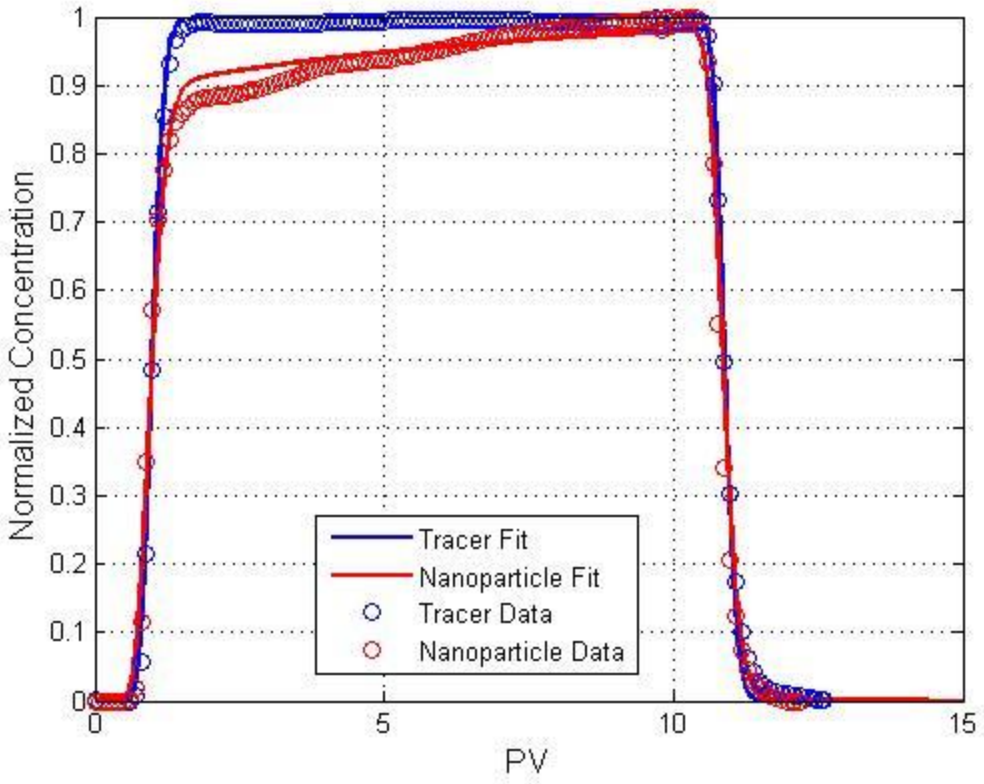

Figure 5.27: Experimental (circles) and simulated (curves) effluent histories by the two-site model for 9.88 PV injection of tracer and nanoparticle into Berea sandstone core for Exp. A4. The fitted parameters are summarized in Table 5.3.

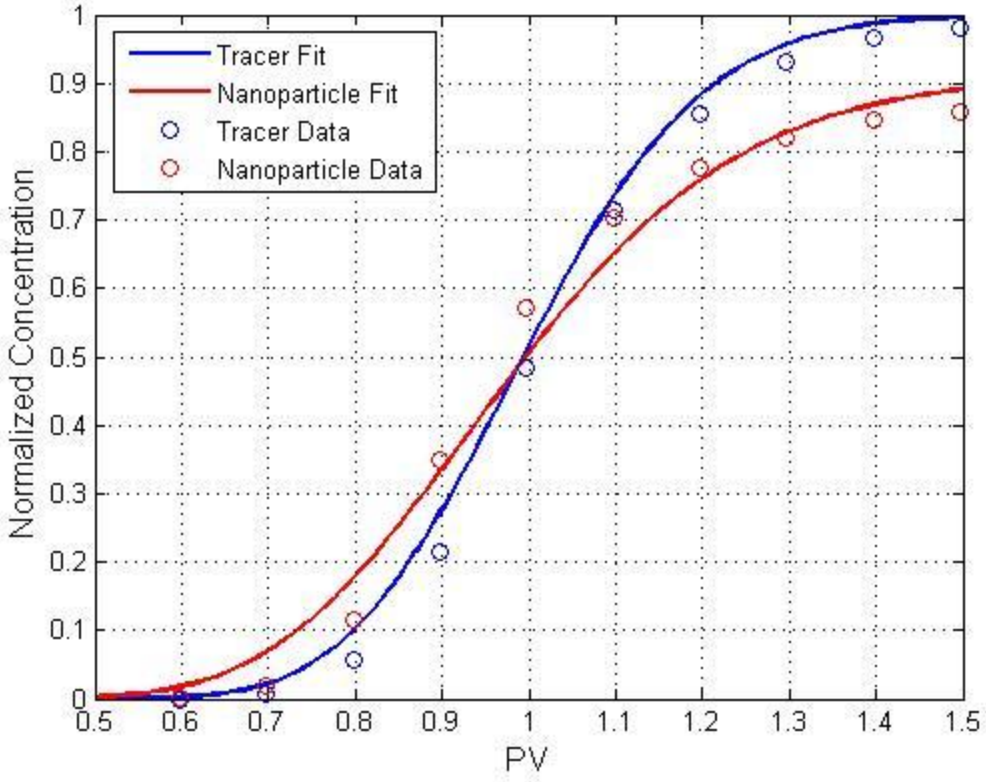

Figure 5.28: Leading edge of the experimental (circles) and simulated (curves) effluent histories by the two-site model for 9.88 PV injection of tracer and nanoparticle into Berea sandstone core for Exp. A4. The fitted parameters are summarized in Table 5.3.

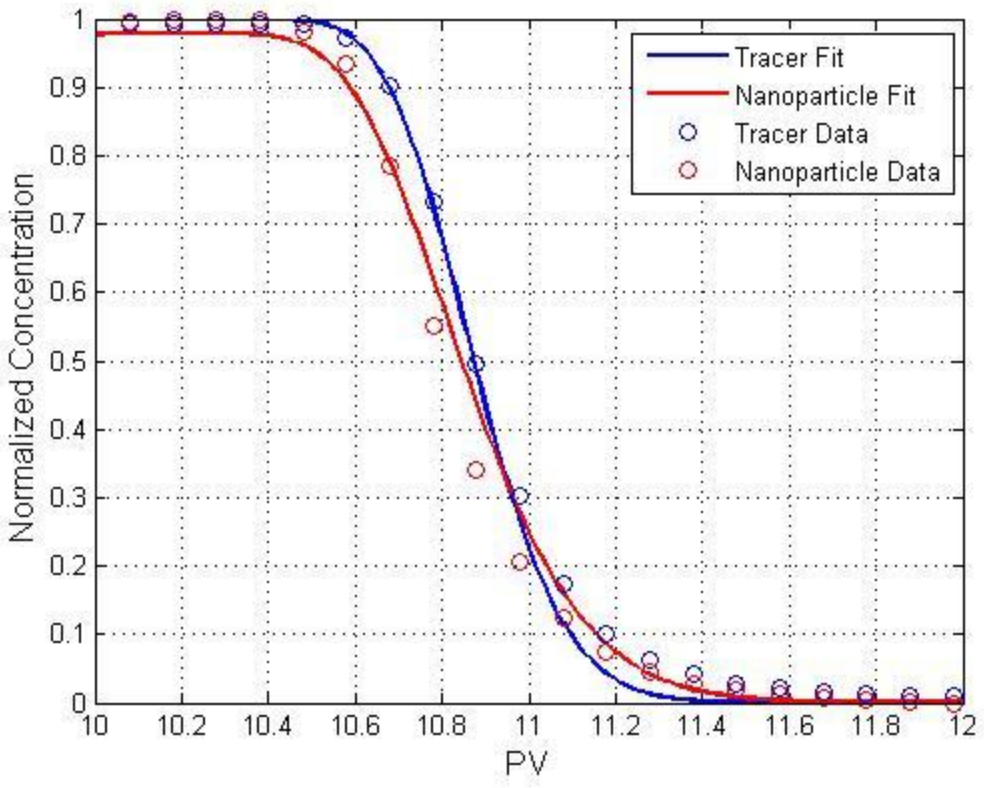

Figure 5.29: Trailing edge of the experimental (circles) and simulated (curves) effluent histories by the two-site model for 9.88 PV injection of tracer and nanoparticle into Berea sandstone core for Exp. A4. The fitted parameters are summarized in Table 5.3.

Previous fit in Figure 5.24 shows significant errors in the leading edge and the trailing edge, because nanoparticles arrived at the core outlet earlier than the model prediction. In order to minimize these discrepancies, the optimization scheme broadened the leading edge and the trailing edge by decreasing the Peclet number. As in the previous fitting exercise, the optimization protocol also minimized the extent of reversible adsorption, which tends to delay the whole curve as shown in the next section. On physical grounds, however, zero reversible adsorption is not likely, as previous studies by Murphy (2011), Yu (2011), and Zhang (2011) have all shown that these

nanoparticles are reversibly adsorbed on to rock surface and get released during postflush. In order to minimize the errors in the leading and trailing edges, the model sacrifices its accuracy in the shoulder portion of the curve. However, the rate and extent of the adsorption and desorption processes are most clearly reflected in this shoulder. Therefore, it can be concluded that the new optimization led to a less accurate model of the nanoparticle transport process (Figure 5.27) than the previous fit (Figure 5.24) which assumed the same Peclet number for both tracer and nanoparticles.

In conclusion, the two-site model does not seem fully competent to reflect all the key processes that happen during nanoparticle transport in porous media. The model's deviation from the experimental data, especially in the leading edge and the trailing edge, can be due to the fact that the model does not account for the accelerated transport of nanoparticles that was observed in the experimental results. However, the model is still a useful tool to visualize changes in the effluent history of a component that undergoes adsorption during its transport in porous media. In the next section, we will resort to this capability of the two-site model to help estimate the acceleration factor of the nanoparticles transported in a sedimentary rock from the experimental data.

Estimation of the Acceleration Factor, *E*

During discussions on Figure 5.26, we have shown that the trailing edges of the tracer and nanoparticle breakthrough curves obtained from the two-site model are overlaid on top of each other, because that the best-fit adsorption rates correspond to negligible extent of reversible adsorption. The observed breakthrough curves, in contrast, clearly show early arrival of the nanoparticles relative to the tracer. Therefore, the obvious choice to estimate the acceleration factor of the nanoparticles is the trailing edge, because nanoparticle retention processes are minimal in that part of the slug. Thus the difference between the observed arrival times of the nanoparticles and the tracer in the trailing edge would be a direct indication of how much faster nanoparticles traveled relative to the tracer. However, this claim has to be tested before this method is put to work by making sure that the location of the trailing edge is not sensitive to changes in the adsorption rates close to the fitted experimental values shown in Table 5.2. This test is carried out by increasing each of the irreversible and reversible Damköhler numbers (M_3 and M_4) in Table 5.2 by orders of magnitude. Figure 5.30 and Figure 5.31 show the results.

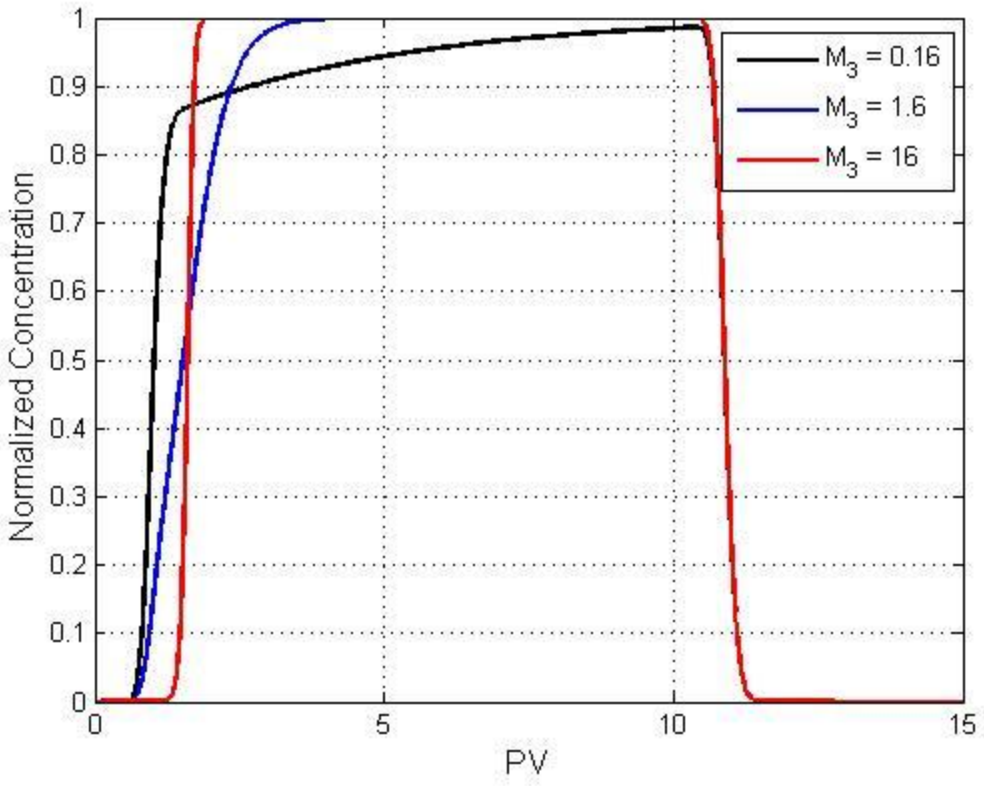

Figure 5.30: Nanoparticle breakthrough curves predicted by the two-site model for different irreversible Damköhler number (M_3); values of other parameters are as Table 5.2

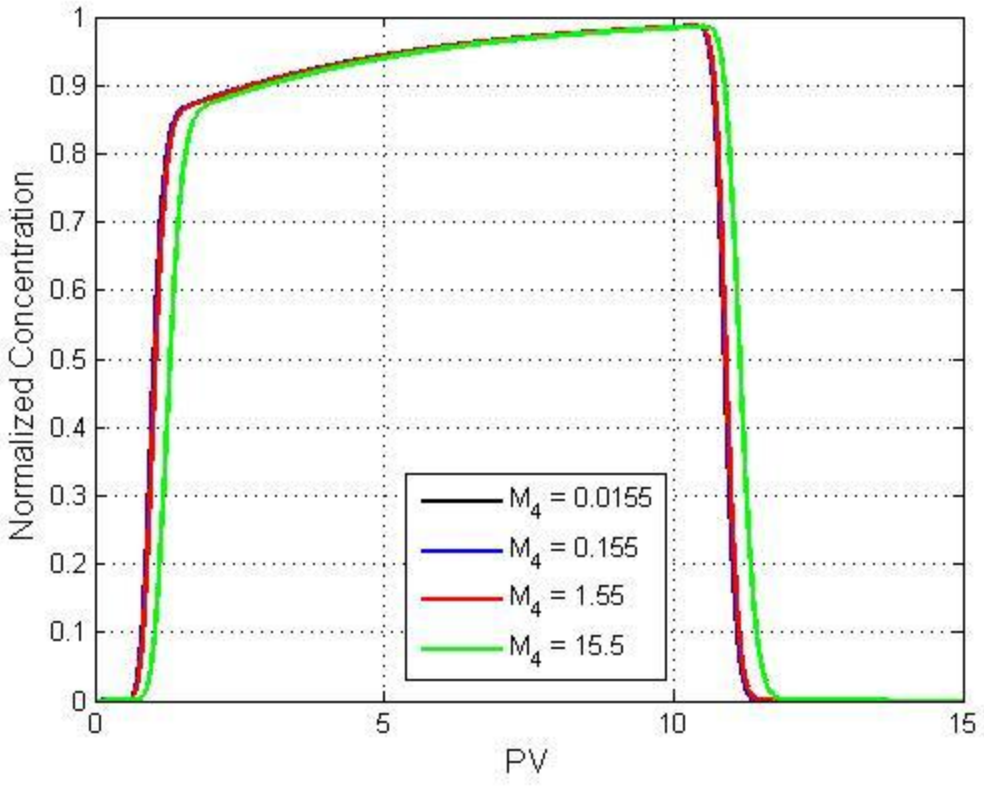

Figure 5.31: Nanoparticle breakthrough curves predicted by the two-site model for different reversible Damköhler number (M_4); values of other parameters are as Table 5.2.

Breakthrough curves in Figure 5.30 show that increases in the irreversible adsorption rate change the leading edge but not the trailing edge. Changes in the reversible adsorption rate, however, affect both the leading edge and the trailing edge by almost an equal amount. However, the effect is still minimal up to a two-orders-of-magnitude increase as shown in Figure 5.32. Irreversible and reversible adsorptions move the leading edge to later arrival time. Irreversible adsorption does not move the trailing edge but reversible adsorption moves the trailing edge later in time. Therefore, it is deemed acceptable to estimate the acceleration from the trailing edge because neither nanoparticle adsorption process moves the trailing edge earlier in time. Using this

analysis, the acceleration factor, which is defined as the ratio of the velocities of the tracer and the nanoparticle, can be calculated by the ratio of the arrival times at which equivalent concentrations of the two components are seen in the effluent:

$$E = \frac{PV_{tracer}@\ c_{Di} - PV_{postflush}}{PV_{nanoparticle}@c_{Di} - PV_{postflush}}$$

In this equation, $\mathrm{PV_{tracer}}@\ c_{Di}$ is the pore volume at which the tracer reached a normalized concentration, c_{Di}, $\mathrm{PV_{nanoparticle}}@c_{Di}$ is the pore volume at which the nanoparticles reached the same concentration c_{Di} and $\mathrm{PV_{postflush}}$ is the pore volume at which postflush began. A c_{Di} of 0.5 was chosen because the trailing edges are roughly symmetric about this point and therefore least affected by features such as an elongated tail. Thus, the acceleration factor for Exp. A4 is calculated as 1.077. This particular experiment presents a very convenient case where the tail of the nanoparticles is not elongated due to a fast desorption rate. A more meticulous analysis would be required to estimate the acceleration factor in other cases. In the same manner, the acceleration factor for the rest of the experiments is calculated and summarized in Table 5.4.

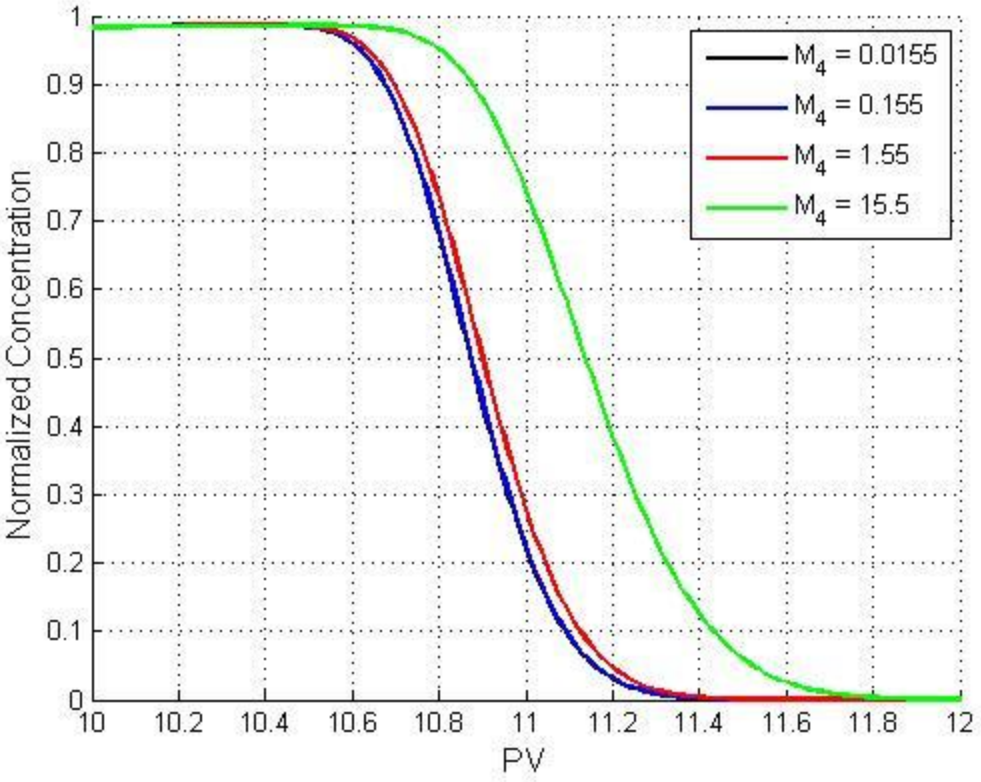

Figure 5.32: Trailing edges of the nanoparticle breakthrough curves predicted by the two-site model for different reversible Damköhler number (M_4).

Experiment #	Acceleration Factor, *E*
Exp. A1 3.8 PV injection of 1 wt% nanoparticle	1.153
Exp. A2 2.2 PV injection of 0.5 wt% nanoparticle 2.2 PV injection of 1 wt% nanoparticle	1.236
Exp. A3 2.9 PV injection of 0.7 wt% nanoparticle 4.4 PV injection of 1.4 wt% nanoparticle	1.125
Exp. A4 9.9 PV injection of 1 wt% nanoparticle	1.077

Table 5.4: Acceleration factor, *E*, estimated from the single-phase flow experimental data.

Table 5.4 shows that the acceleration factor for the Boise sandstone (Exp. A1 and Exp. A2) was higher than for the Berea sandstone (Exp. A3 and Exp. A4). It was hypothesized that the volume of inaccessible pore would depend on the relative size of the particle to that of the pore throat in the porous medium. The Berea sandstone core was five times less permeable than the Boise sandstone core. As a result, pore throat sizes in the Berea sandstone core are smaller than those in the Boise sandstone core, and therefore size exclusion effects should be greater in the Berea experiments. Although it was expected that the higher inaccessible pore volume in the Berea sandstone core would cause the nanoparticles to accelerate to a greater extent than in the Boise sandstone core, Table 5.4 suggests the opposite. This could be because heterogeneity, dead-end pores or non-Fickian dispersion, any of which could have caused the non-classical tracer behavior

in the Boise experiments, counteracts the acceleration. More experiments should be conducted to investigate the full effect of lithology on the acceleration factor.

Mechanism of Accelerated Transport

The accelerated transport of nanoparticles demonstrated here experimentally is not the first time an anomaly is observed during nanoparticle transport. Figure 5.33 shows observations from Rodriguez et al. (2010) where the apparent viscosities of nanoparticle dispersions flowing through sedimentary rocks were significantly smaller compared to viscosities measured as bulk dispersions.

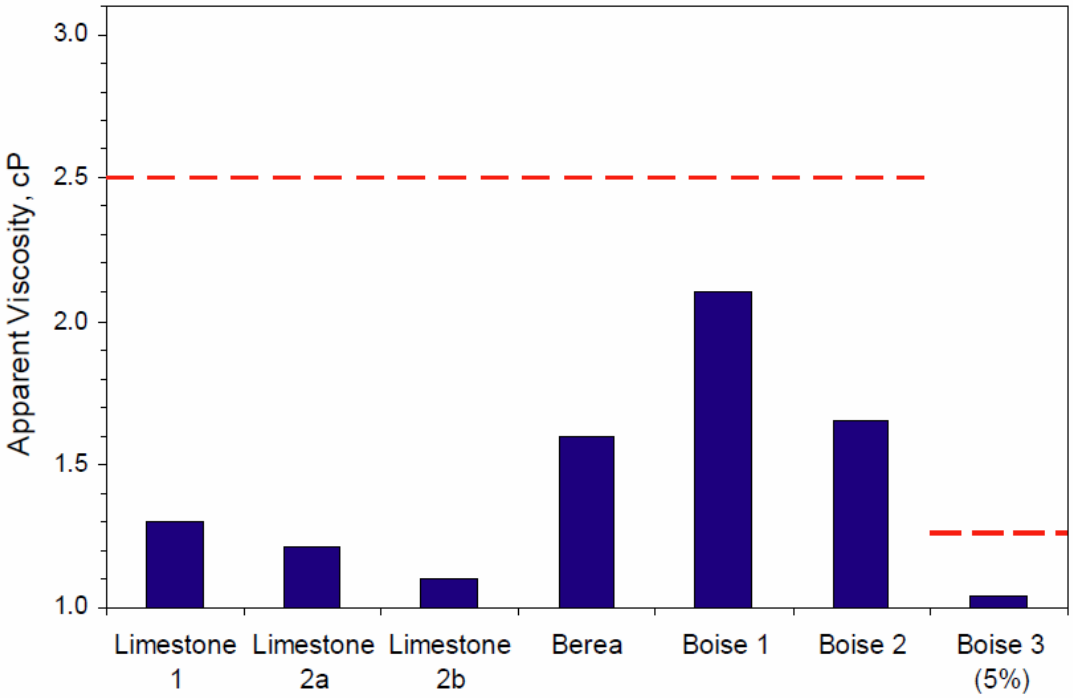

Figure 5.33: Apparent viscosities for the different core floods. The red line indicates the viscosity of the bulk solution injected into each core (Rodriguez et al., 2010).

In order to explain this form of "enhanced migration" of the nanoparticle dispersions, Rodriguez et al. (2010) proposed applying the depleted layer model. This model postulates an existence of a layer of fluid near the pore walls that is depleted of nanoparticles as shown in Figure 5.34. Because the fluid viscosity increases with increasing nanoparticle concentration, the depleted layer would have exhibit a lower viscosity than the bulk phase. Integration of the velocities over the respective area allows us to calculate the flow rate in the depleted layer and the bulk zone. Interpreted in terms of the Hagen-Poiseuille equation

$$q = \frac{\pi R^4}{8\mu L}\Delta P$$

this increase in velocity is equivalent to a reduction in apparent viscosity of the fluid moving in the capillary tube. According to Darcy's law, during flow through a porous medium with a given permeability k and cross-sectional area A and a pressure gradient ΔP, the fluid velocity will increase with a lower apparent viscosity of the fluid.

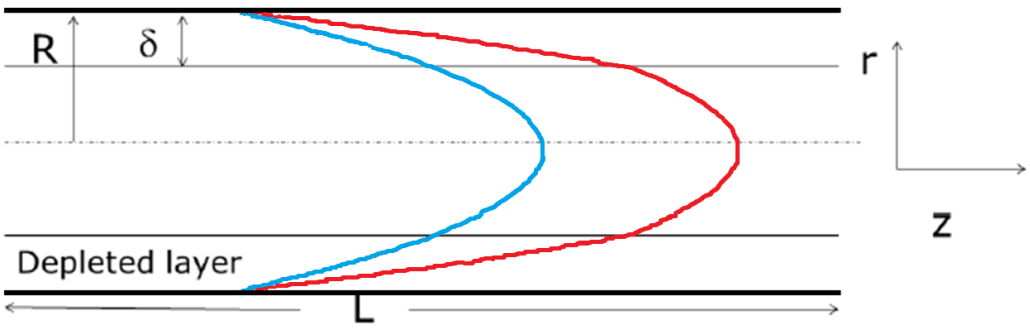

Figure 5.34: Sketch of velocity profile for nanoparticle dispersion flow in a capillary tube with (red) and without (blue) depleted layer. The nanoparticle concentration in the depleted layer (δ) is zero and the concentration in the middle portion is the injected concentration (Modified from Aminzadeh, 2013).

More recently, Aminzadeh (2013) made modifications to the depleted layer model by proposing that nanoparticle dispersions only travel outside of the slippage layer through the center of the tube in Figure 5.34. Since the flow velocity is higher nearer the center of a capillary tube, nanoparticles follow the faster streamlines, resulting in a higher transport velocity compared to the base fluid.

Because it is the size of the nanoparticles that prevents nanoparticles from traveling near the pore wall, the acceleration should increase with increasing size. In addition, Aminzadeh (2013) calculates the acceleration factors from the measured apparent viscosities in different porous media as summarized in Table 5.5.

Core Type	k mD	Φ -	Measured μ_{app} cP	Calculated μ_{app} cP	Calculated E -
Texas Cream LS	15	0.29	1.3	1.12	1.39
Texas Cream LS	10	0.22	1.15	1.08	1.43
Boise SS	900	0.28	2.10	2.10	1.04
Berea SS	130	0.22	1.7	1.66	1.12

Table 5.5: Measured and calculated apparent viscosity of 18 wt% nanoparticle dispersion flow in different porous media. The thickness of the depleted layer is 100 nm (Aminzadeh, 2013).

Table 5.5 predicts that the lower permeability core would lead to a larger acceleration factor. However, the opposite trend was observed from the experimental results presented in this chapter as summarized in Table 5.4. Another experiment with a low-permeability Texas Cream limestone should better reveal the effect of permeability on the acceleration factor.

Another proposed mechanism of the accelerated transportability of nanoparticles is caused by any potential interactions between nanoparticles and the rock surface that do not allow nanoparticles to come near the pore wall. Such nanoparticle transport can be modeled by relaxing no-slippage boundary condition. The slip length (λ) is defined as the extrapolated distance from the pore wall where the tangential component of the fluid velocity vanishes (Priezjev, 2007). This slip length has the equivalent effect of increasing the radius of the capillary tube by λ. For a constant pressure gradient, the increase in the tube radius will increase the flow velocity of the fluid. Such a hypothetical slippage case would be very similar to the depleted layer model in the respect that a small layer that is depleted of nanoparticles will form near the pore walls.

Buongiorno (2006) presents and analyzes seven slip mechanisms that could result in the difference between the absolute nanoparticle velocity and the base fluid velocity including inertia, Brownian diffusion, thermophoresis, diffusiophoresis, Magnus effect, fluid drainage, and gravity settling. Of seven mechanisms, Brownian diffusion and thermophoresis are identified as the most relevant mechanisms in the absence of turbulent eddies. The contribution of Brownian motion is negligible (Brownian diffusion coefficient is on the order of 10^{-11} m/s) and there is no temperature gradient in the experiments conducted in this study. Therefore, the slip mechanism would not be able to account for the obvious early arrival of nanoparticles compared to the tracer.

Another interesting proposition stems from Krishnamurthy et al. (2006). As nanoparticles get squeezed into pore throats, their dispersion stability is disrupted and nanoparticles coagulate to make up bigger particles. Wear-out of functional coatings during transport observed by Yu (2012) can also contribute this instability. The coagulated particles become too large to pass through some of the smaller pore throats,

leading to the inaccessible pore volume by size exclusion. However, no experimental verifications have been made on this hypothesis.

Two-Site Model with Acceleration Factor (*E*)

In order to account for the enhanced transportability of nanoparticles in porous media, the two-site model is modified by adding the acceleration factor, *E*, to the convection-dispersion equation:

$$\frac{1}{E}\frac{\partial c}{\partial t}+\frac{\rho_b}{\phi}\frac{\partial s}{\partial t}=D\frac{\partial^2 c}{\partial x^2}-v_p\frac{\partial c}{\partial x}$$

where *E* is greater than 1. In this equation, *E* works just like a retardation factor except *E* advances the effluent concentration history to earlier time whereas the retardation factor delays the curve to later time. In order to validate the model, the parameters from the finite-core model tracer fit (obtained by setting $M_1 = 1\times10^{-20}$, $M_2 = 1\times10^{-20}$, $M_3 = 0$, $M_4 = 0$, $M_5 = 0$ and $N_P = 285$ in the two-site model) for Exp. A4 (Figures 5.22 through Figure 5.23) were used with *E* values of 1 and 1.077. The resulting curves are shown in Figure 5.35 through Figure 5.37.

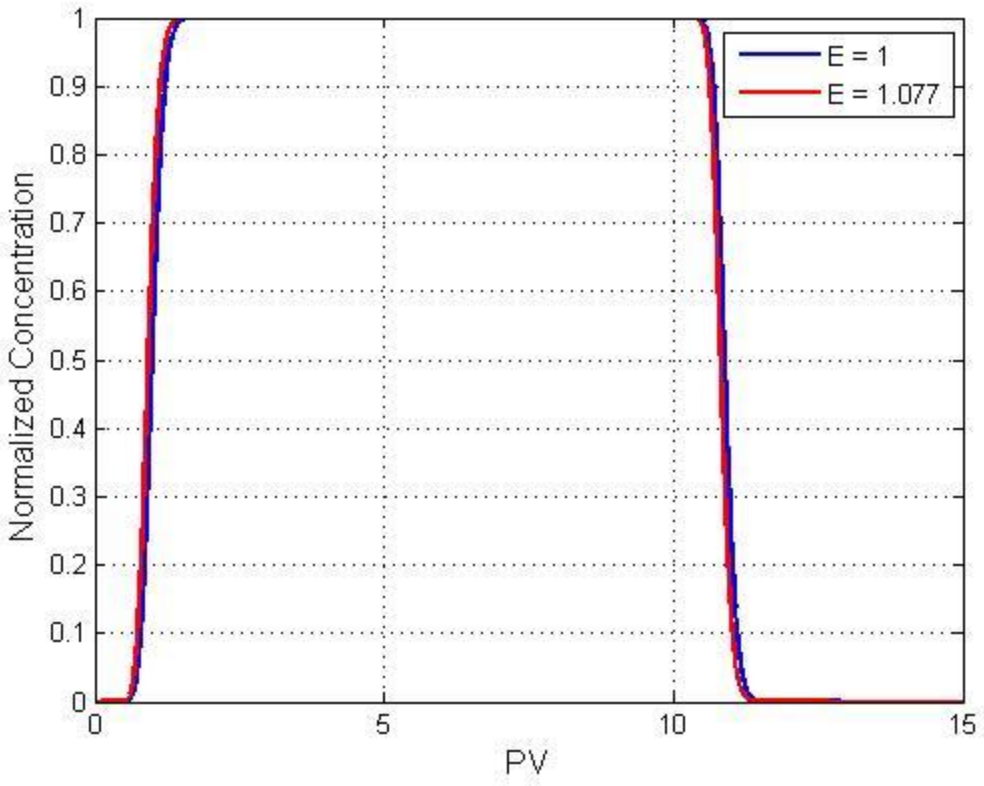

Figure 5.35: Simulated tracer effluent histories by the modified two-site model for 9.88 PV injection of tracer and nanoparticle into Berea sandstone core for Exp. A4. The blue curve is the original fit in Figure 5.21 and the red curve is a modified fit with E = 1.077. Other fitted parameters are summarized in Table 5.3.

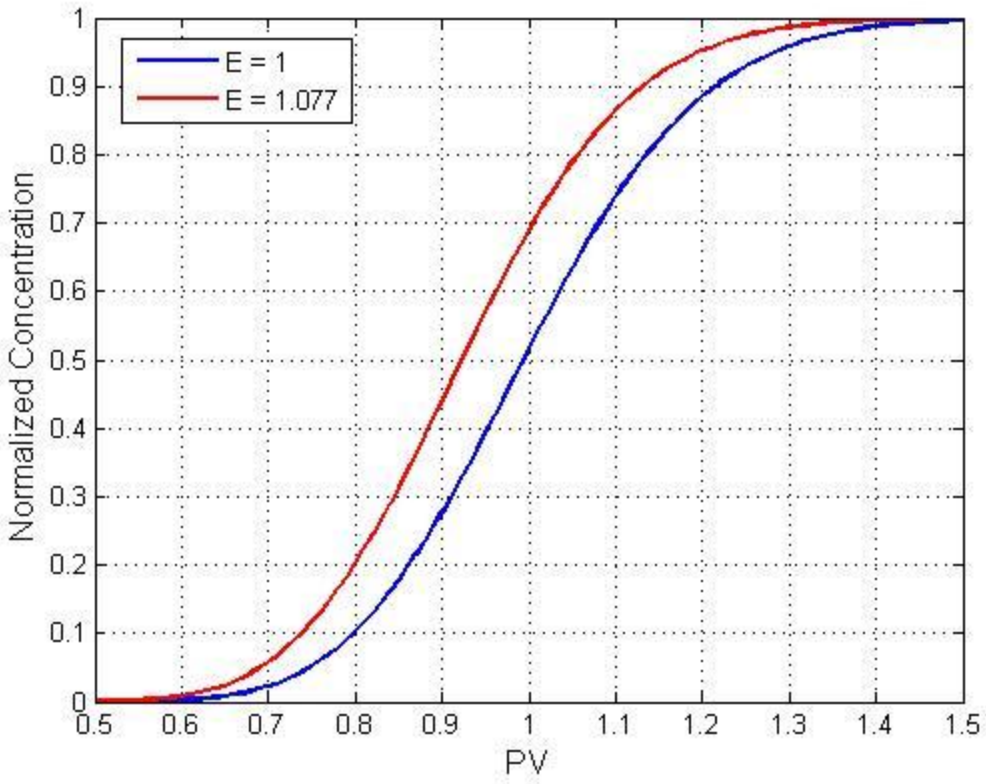

Figure 5.36: Leading edge of simulated tracer effluent histories by the modified two-site model for 9.88 PV injection of tracer and nanoparticle into Berea sandstone core for Exp. A4. The blue curve is the original fit in Figure 5.22 and the red curve is a modified fit with E = 1.077. Other fitted parameters are summarized in Table 5.3.

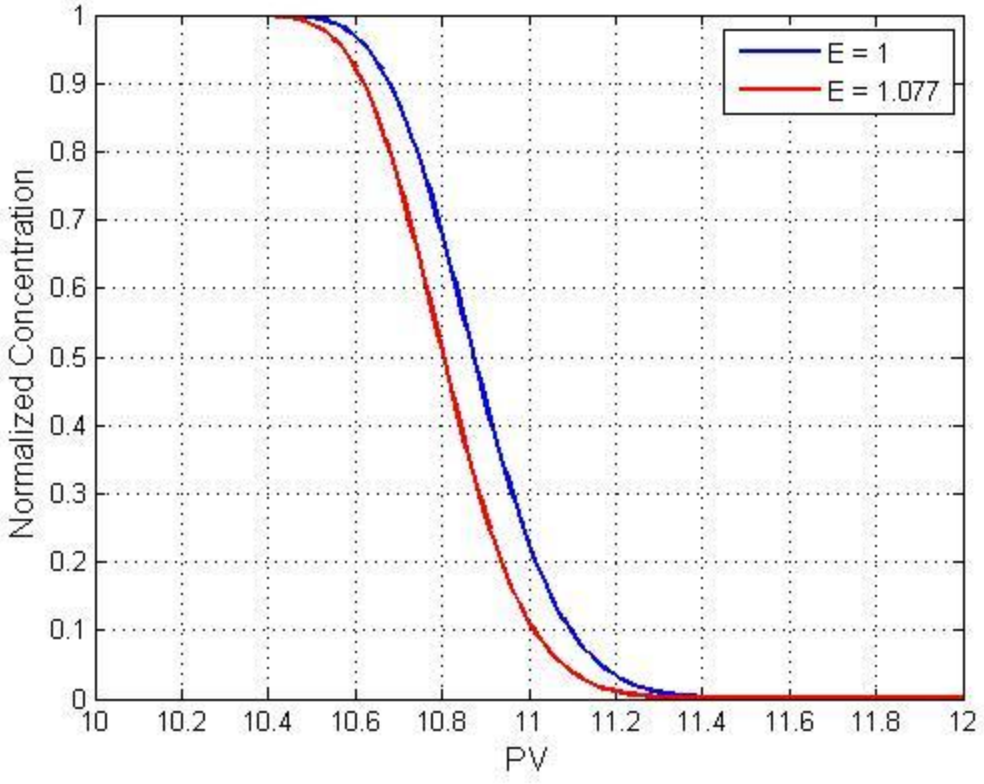

Figure 5.37: Trailing edge of simulated tracer effluent histories by the modified two-site model for 9.88 PV injection of tracer and nanoparticle into Berea sandstone core for Exp. A4. The blue curve is the original fit in Figure 5.23 and the red curve is a modified fit with E = 1.077. Other fitted parameters are summarized in Table 5.3.

As can be observed in the leading edge and the trailing edge in Figure 5.36 and Figure 5.37, the effluent history with E of 1.077 arrives approximately 0.08 PV earlier than the one with E of 1. In other words, E shifts the effluent history earlier in time by (E - 1) PV.

Using the modified two-site model, the fitting parameters except for the adsorption site capacities were optimized to generate a best-matching fit to the

nanoparticle effluent data from Exp. A4. The optimized parameters are shown in Table 5.6.

Dimensional		Dimensionless	
D, m^2/s	1.56×10^{-7}	N_P	214
S_{1max}, g/g	4.95×10^{-3}	M_1	0.60
S_{2max}, g/g	3.14×10^{-2}	M_2	3.81
k_{irr}, 1/s	5.81×10^{-5}	M_3	0.162
k_{ra}, 1/s	4.12×10^{-5}	M_4	0.116
k_{rd}, 1/s	1.91×10^{-2}	M_5	202

Table 5.6: Fitted parameters including the Peclet number in the modified two-site model with E = 1.077 for the nanoparticle effluent history from Exp. A4.

With E of 1.077, the reversible adsorption rate increased by an order of magnitude compared to the original fit in Table 5.2 where a negligible rate was necessary to minimize the delay caused by reversible adsorption. The experimental (circles) and modified simulated (curves) tracer and nanoparticle effluent histories are found in Figure 5.38 through Figure 5.40.

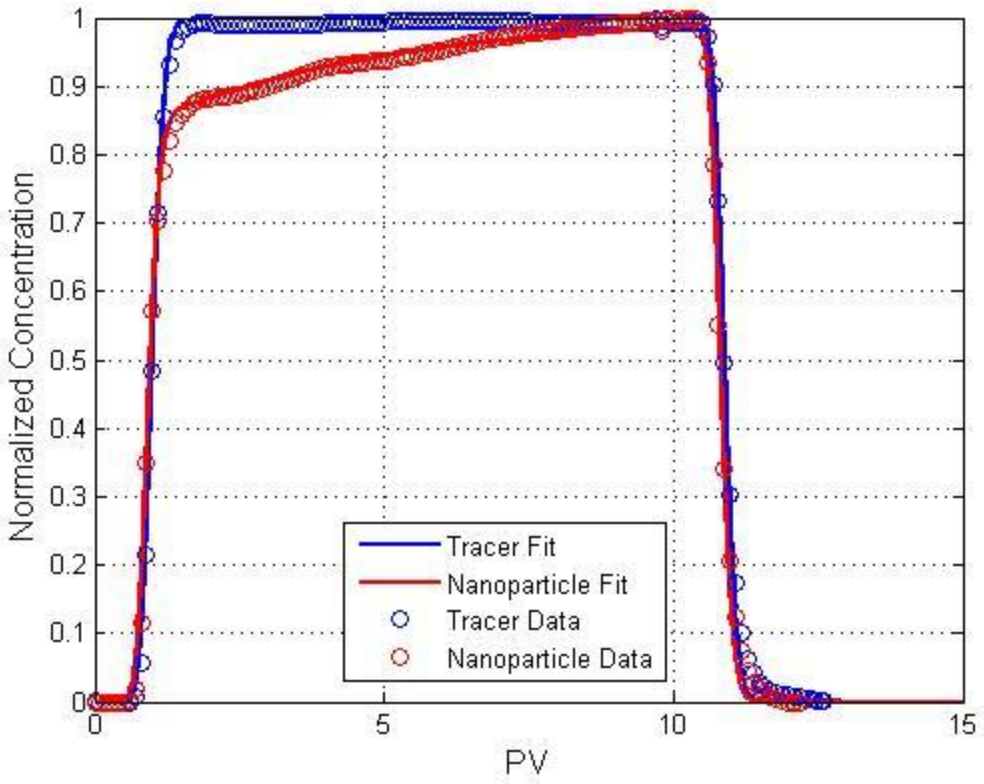

Figure 5.38: Experimental (circles) and simulated (curves) effluent histories by the modified two-site model for 9.88 PV injection of tracer and nanoparticle into Berea sandstone core for Exp. A4. *E* is 1 for tracer (blue) and 1.077 for nanoparticle (red).Other fitted parameters are summarized in Table 5.6.

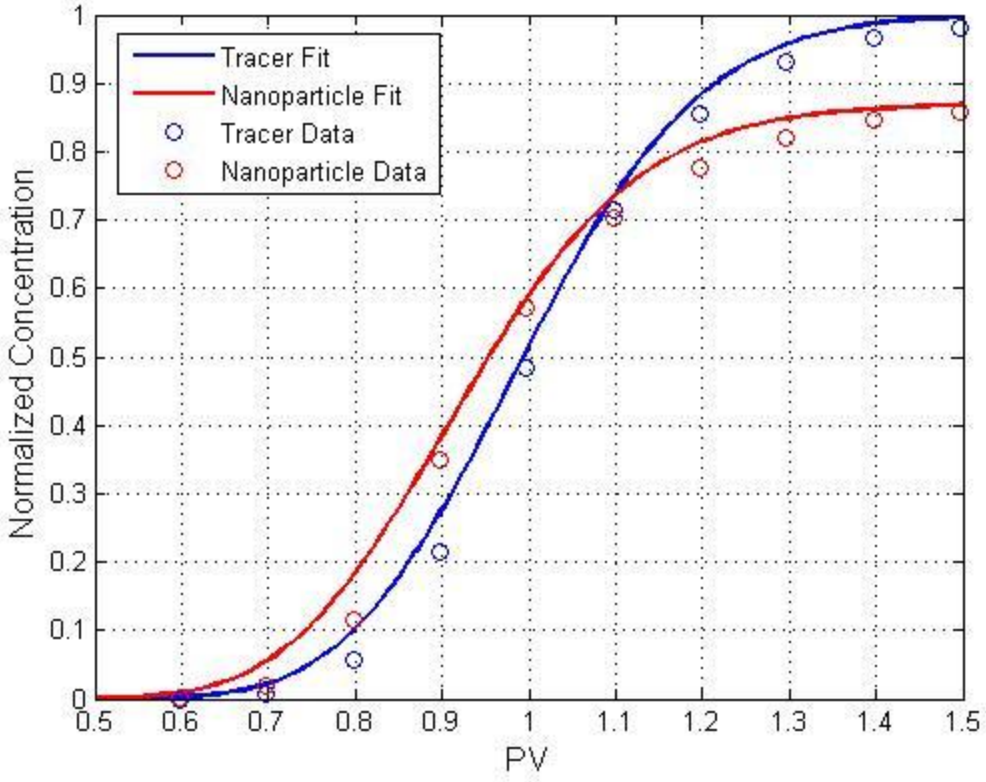

Figure 5.39: Leading edge of experimental (circles) and simulated (curves) effluent histories by the modified two-site model for 9.88 PV injection of tracer and nanoparticle into Berea sandstone core for Exp. A4. *E* is 1 for tracer (blue) and 1.077 for nanoparticle (red).Other fitted parameters are summarized in Table 5.6.

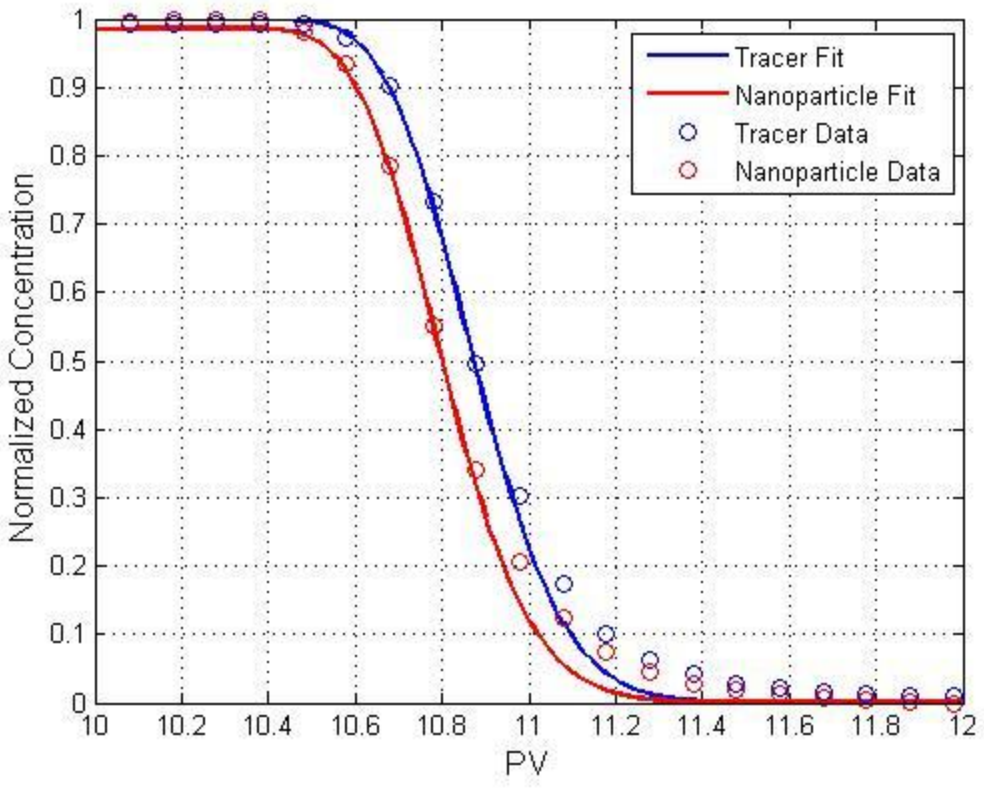

Figure 5.40: Trailing edge of experimental (circles) and simulated (curves) effluent histories by the modified two-site model for 9.88 PV injection of tracer and nanoparticle into Berea sandstone core for Exp. A4. *E* is 1 for tracer (blue) and 1.077 for nanoparticle (red).Other fitted parameters are summarized in Table 5.6.

Thus far, we have shown three different fits to the experimental data from Exp. A4. In the first fit (Figure 5.24 through Figure 5.26), the adsorption rates were adjusted to match the experimental data with a fixed Peclet number obtained from the passive tracer fit. In the second fit (Figure 5.27 through Figure 5.29), the Peclet number was adjusted along with the adsorption rates to match the experimental data. The third fit (Figure 5.38 through Figure 5.40) used the modified two-site model with $E = 1.077$, obtained from the experimental data, with adjustable adsorption rates and Peclet number. We have argued

earlier that the second fit gave reversible adsorption rate of nearly zero that was improbable on physical grounds and from earlier nanoparticle transport experiments in porous media. Both the first fit and the third fit well predict the shoulder portion of the curve that conveys most information about nanoparticle adsorption and desorption processes. However, the first fit shows a delay in the model prediction compared to the experimental data in the leading edge and in the trailing edge, while the third fit with the acceleration factor matches the experimental data more closely in the leading edge and the trailing edge. The misfit in the leading edge and the trailing edge was calculated by summing the squares of the difference between the entire experimental data (i.e. not restricted to the sampled data) and the simulated curve in the leading edge (0.5 PV to 1.5 PV) and the trailing edge (10.4 PV to 11.4 PV). The misfit is 2.04 with the modified model and 4.14 with the unmodified model. Therefore, a good method to model the nanoparticle transport in porous media is to quantify the acceleration factor in the trailing edges from the experimental data and fit the adsorption parameters and the Peclet number with the tracer-fit Peclet number as an initial guess. This systematic method using the modified two-site model captures all the characteristic features of the nanoparticle effluent curve, which are the leading edge, the trailing edge, and the shoulder, better than simply assuming no acceleration and fitting all the parameters with the original two-site model.

5.4 CONCLUSIONS

Single-phase flow experiment in porous media shows that nanoparticles travel faster than molecules of a conservative tracer in the base fluid, arriving earlier in the effluent than the tracer at both the leading and trailing edges of a slug. The faster transport is clearly evident at the leading edge only when the irreversible retention capacity of the rock for the nanoparticles has been satisfied. The two-site model developed by Zhang was fitted to experimental data, but the fits cannot explain the early arrival of nanoparticles relative to tracer. An acceleration factor E was estimated from the data to be 1.077 for Exp. A4. A modification was made to the two-site model by introducing E. The resulting model matched the experimental nanoparticle effluent history, especially the leading and trailing edges of the slug which are most sensitive to acceleration, better than the original model. This result suggests that nanoparticle transport in a porous medium involves a complex mechanism that not only includes adsorption and desorption on rock surfaces but also other processes that accelerate the particles compared to the aqueous phase in which they are dispersed.

One of the physical mechanisms that may be responsible for the enhanced transport of nanoparticles is the existence of a depleted layer near the pore walls where the nanoparticles concentration is zero. As a result, nanoparticles travel on the faster streamlines in the middle of the pore, leading to an earlier arrival than a tracer that undergoes no interaction with the porous media.

The observation of accelerated transport of nanoparticles in these single-phase experiments is consistent with the density "overshoot" and the larger-than-injected effluent nanoparticle concentration observed in imbibition displacements in Chapter 4.

Chapter 6

Conclusions

6.1 CONCLUSIONS

During drainage displacement experiments, the pressure drop across the core was 1.3 to 2 times higher when nanoparticles were present in the wetting phase, suggesting that the presence of nanoparticles led to pore blocking and formation of another phase that is more viscous than pure n-octane. The comparisons of the CT images of the control experiment and the nanoparticle experiment also hint at the formation of fluid with a density intermediate to that of brine and of n-octane. It can be inferred from these observations that nanoparticle-stabilized oil-in-water emulsions were formed in-situ during pore-scale displacement. As a result, the displacement was stabilized as evidenced by a reduction of viscous fingering in the CT images and the reduced mobility of n-octane, as inferred from the pressure drop data. However, an analog experiment with CO_2 showed that the presence of nanoparticles reduced the mobility of the CO_2 by a factor similar to the n-octane experiment, though this was not enough to stabilize the displacement. Formation of emulsions during drainage displacement supports the hypothesis that formation of droplets as a result of a temporary disruption of interface stability, a process known as Roof snap-off, followed by attachment of nanoparticles to the droplet surface, is the main mechanism for generating emulsions in porous media.

The Roof snap-off hypothesis was put to test during imbibition displacement experiments where Roof snap-off does not occur because the wetting phase is advancing. The difference in pressure drop across the core for the brine injection (control case) and the nanoparticle dispersion injection (nanoparticle case) were solely due to the contrast in the viscosities of the two fluids. Therefore, we concluded that the presence of

nanoparticles did not change the dynamics of the imbibition displacement. However, it was inferred from the saturation profile as well as the saturation profiles that nanoparticles were accumulating at the front of the displacement. This accumulation suggests that nanoparticles were traveling faster than the base fluid, but as they encountered n-octane, they could no longer move forward and started to accumulate at the displacement front. Inaccessible pore volume was proposed as the driving mechanism of this accelerated transport of nanoparticles.

In order to test the validity of the claim that inaccessible pore volume is the responsible mechanism for enhancing nanoparticle transport, single-phase flow experiments were conducted in which the tracer and the nanoparticles were injected simultaneously into porous media and the effluent concentration was monitored with a UV-Vis detector. The results showed that nanoparticles arrived in the effluent earlier than the tracer, especially when there was little adsorption of nanoparticles on the rock surface. The most consistent explanation of this observation is that the nanoparticles are transported faster than tracer.

In the context of CO_2 sequestration, the drainage displacement experimental results suggest that the use of nanoparticles may be a potential cure for stopping or at least slowing down the movement of buoyant CO_2 escaping a sequestration site. If nanoparticles are added in the chase water in between CO_2 injection, the same mechanism that accumulates nanoparticles at the displacement front during imbibition experiment can be exploited to build up a higher concentration of nanoparticles in-situ by injecting a lower concentration. Furthermore, placement of nanoparticles before CO_2 injection has the potential to increase the sweep efficiency of CO_2 injection and increase the total storage capacity of an aquifer and enhance capillary trapping for more secure CO_2 storage (Aminzadeh et al., 2013).

6.2 FUTURE WORKS

Experiments in Bead Packs

Over a span of two years, it was observed that core samples from different blocks, even if they are the same rock type (Boise sandstone), have vastly different properties such as homogeneity, permeability, and porosity. This inconsistency made it difficult to compare new experimental results to the old ones. By using bead packs, we can better control the nature of porous medium and this will potentially set up a better stage for identifying the governing physics and mechanisms at play.

Drainage Displacement with Beads of Alternating Size

It is hypothesized that Roof snap-off is most likely to occur in smoothly constricted pores that have a small throat to body ratio (Kovscek et al., 2007). A bead pack can be filled with alternating layers of small and large bead sizes (Figure 6.1).

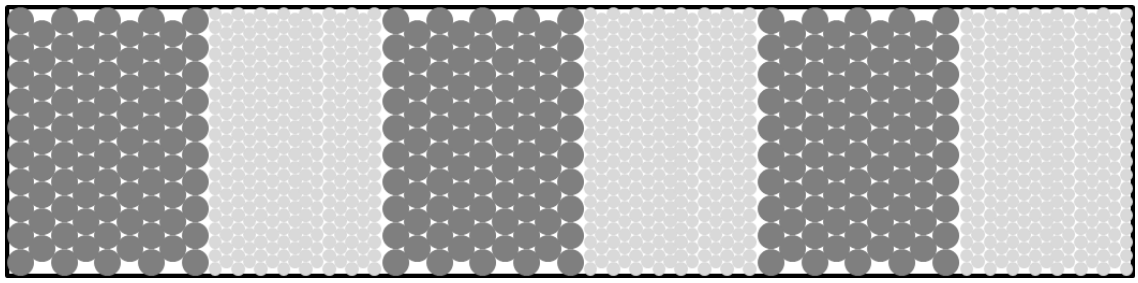

Figure 6.1: Schematics of a bead pack with layers of alternating bead sizes.

The CT scanner can be used to capture the location of the fluid with a density in between that of brine and of n-octane to see if the permeability contrast between one layer and another is more prone for in-situ emulsion formation during displacement.

Imbibition Displacement Experiments with Different Sizes of Nanoparticles

Imbibition displacement experiments can be done with different sizes of nanoparticles to investigate the effect of nanoparticle size on the amount of concentration overshoot. In accordance to the depleted layer model, the overshoot amount should increase with increasing nanoparticle size. Different sizes of surface-treated silica nanoparticles (5 nm, 12 nm, 25 nm, 50 nm and 80 nm) are available thanks to generous donation by Nissan Chemical America Corp.

Imbibition Displacement and Single-Phase Flow Experiments with Nanoparticles with Varying Coverage of External Coating

During Murphy (2012)'s experiments, Nyacol's 27-nm DP9711 nanoparticle consistently showed no delay in breakthrough while 3M's 10-nm salt-tolerant nanoparticles showed signs of delay. It is possible that besides the size of the nanoparticles, the amount of coverage and type of external coatings around the core influence how nanoparticles transport in porous medium. Since the coating type is trade-secret for most companies, the amount of coating coverage can be varied to investigate its effect on nanoparticle transport (Nissan Chemical America Corp. suggested they can manufacture nanoparticles with different levels of coating coverage).

Single-Phase Flow Experiment in Different Porous Media

Calculations by Aminzadeh (2013) suggest that the acceleration factor should increase with decreasing permeability of the porous media. This effect can be tested by conducting core floods in low-permeability limestones. However, experiments in limestones would require a regular core holder and accumulators instead of an epoxy core and glass columns used for experimentations presented in this study.

Single-Phase Flow Experiment with Different Sizes of Nanoparticles

Single-phase flow experiment can be done with different sizes of nanoparticles to investigate the effect of nanoparticle size on the nature of enhanced transport of nanoparticles in porous media.

Nanoparticle Dispersions Flow Experiment at Residual Oil Saturation

This experiment is similar to the single-phase flow experiments presented in Chapter 5, except the core is at residual n-octane saturation. This experiment investigates the effect of residual oil phase on the transport of nanoparticles. It is hypothesized that the oil-water interface will act as another adsorption site and counteract the accelerated transport of nanoparticles. We attempted this experiment once before, but the new Nyacol DP9711 batch gave a vastly different response compared to the old samples and the calibration curves could not be applied to analyze the data.

Appendices

A1 EPOXY CORE PREPARATION

Epoxy core is a cheap and fast alternative to using a regular core holder. However, its applications are limited to low-pressure experimental conditions (generally less than 100 psi). These preparation steps for making an epoxy core are applicable to cores that are 1-inch in diameter and 1-foot in length and are as follows:

1. Gather necessary materials: 1 core (1 inch in diameter and 1 foot in length), 1 polycarbonate tube (1.5 inch in diameter and 15 inches in length), 2 NPT endcaps (technical drawing in Figure A1.3), 5-minute epoxy (Devcon), epoxy resin (Miller-Stephenson EPON Resin 828), hardener (Miller Stephenson Versamid 125), rubber stopper, wax paper, tape, scissors.

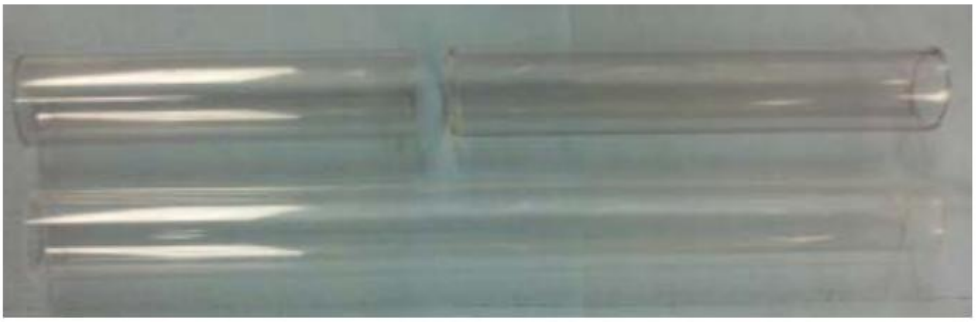

Figure A1.1: Polycarbonate tubes of different lengths (Roberts, 2011).

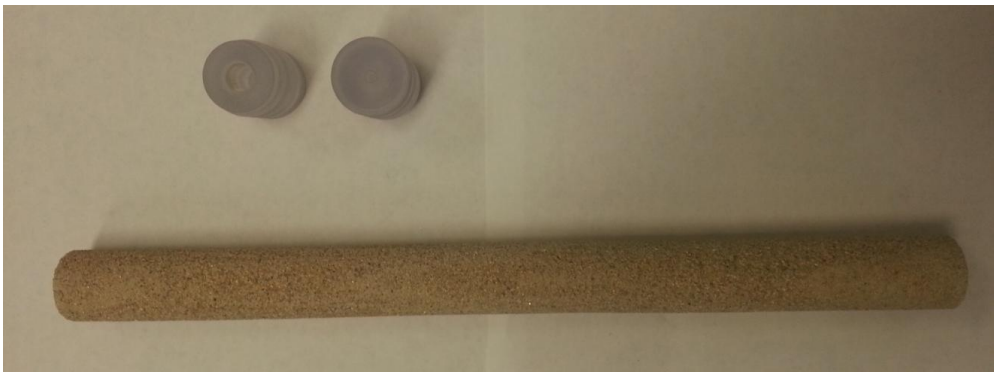

Figure A1.2: Endcaps and Boise sandstone core.

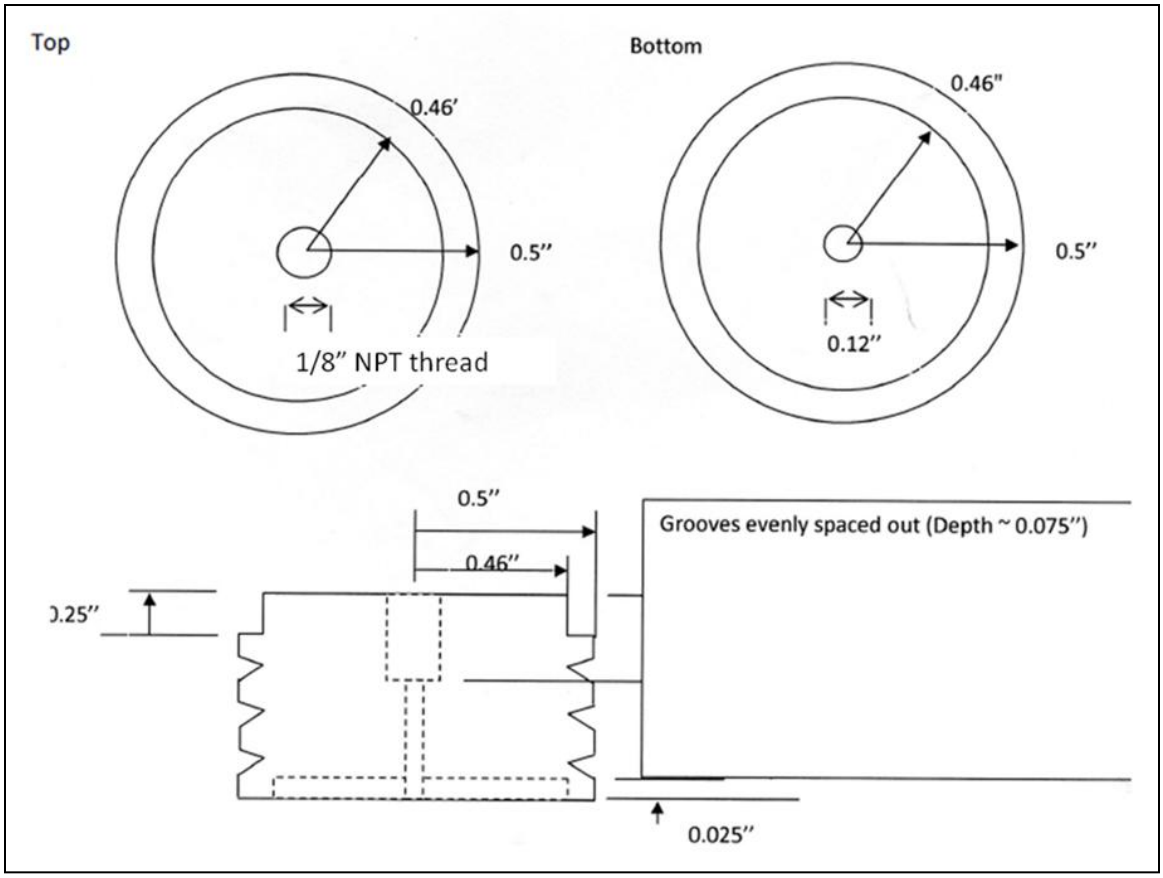

Figure A1.3: Technical drawing of the end-caps.

2. Seal the edge between endcaps and rock with 5-minute epoxy. Be sure not to get any epoxy underneath the endcaps.

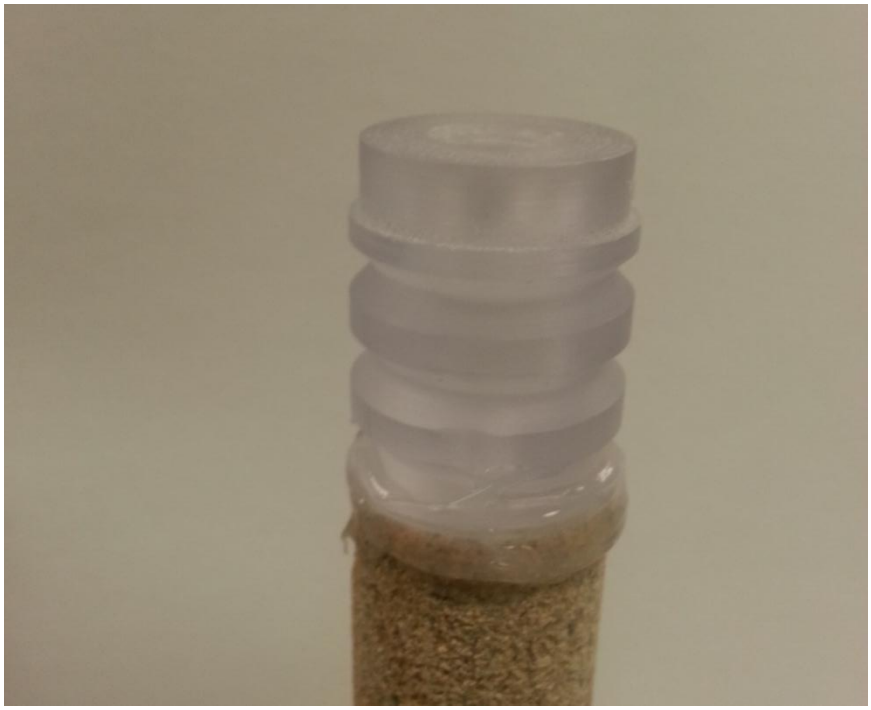

Figure A1.4: Sealing the edge between endcap and rock with 5-minute epoxy.

3. Block the holes of the endcaps with tape.

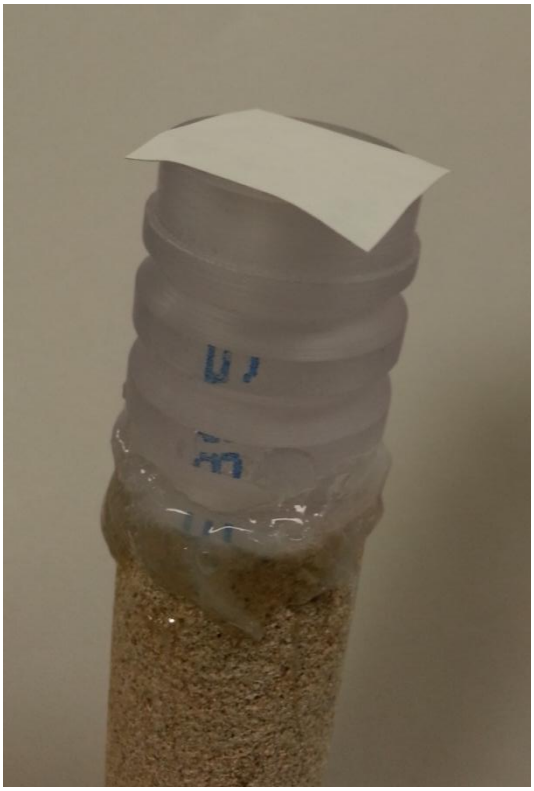

Figure A1.5: Blocking the hole of the endcap with a piece of tape.

4. Cover the rubber stopper with the wax paper and insert it into one end of the polycarbonate tube.

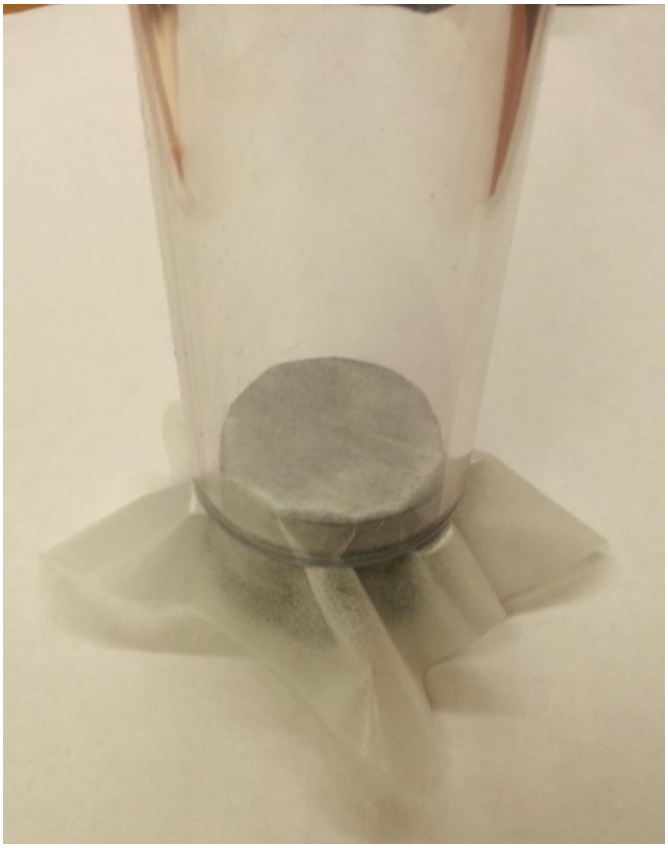

Figure A1.6: Rubber stopper covered with a wax paper inserted into the polycarbonate tube.

5. Place the core inside the polycarbonate tube on top of the rubber stopper.

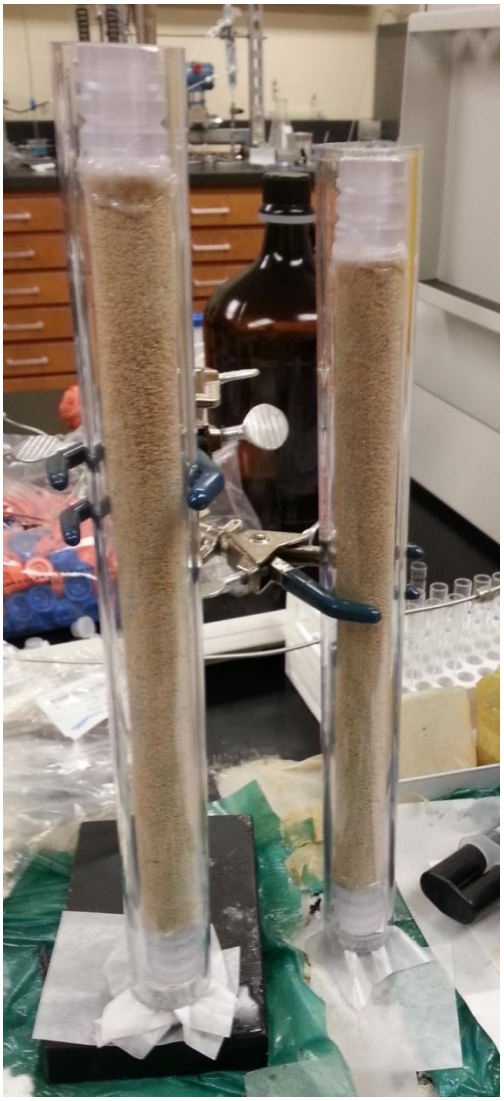

Figure A1.7: Boise sandstone cores placed inside the polycarbonate tubes.

6. Mix the epoxy and hardener until the mixture looks homogeneous.

Figure A1.8: Epoxy and hardener before mixing (left) and after mixing (right).

7. Slowly pour the epoxy resin by filling the polycarbonate tube from the bottom.

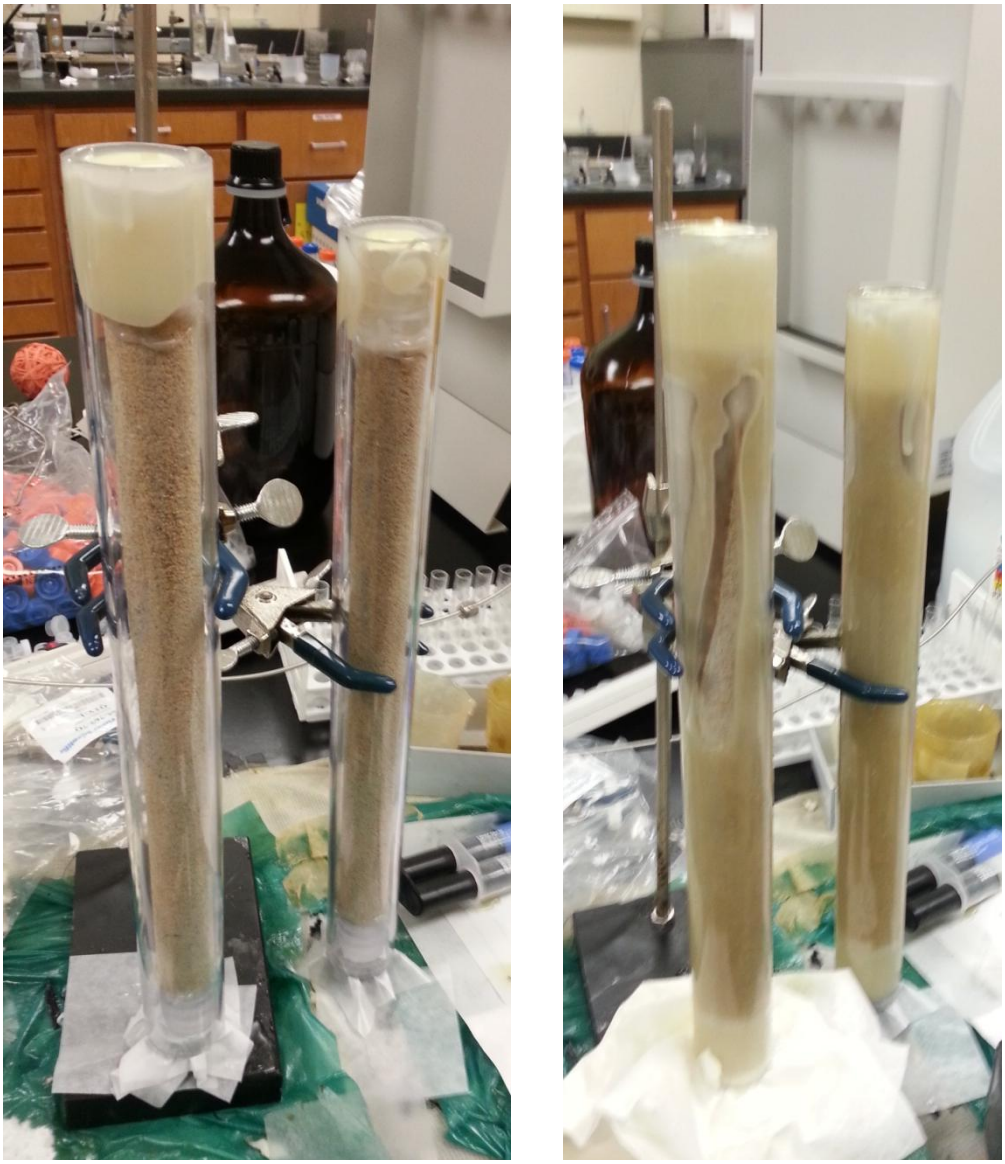

Figure A1.9: Epoxy resin filling the polycarbonate tubes.

8. Let the epoxy cure for overnight.
9. Remove the tape pieces on the endcaps.
10. Attach NPT fittings and Swagelok valves to the endcaps.

Figure A1.10: Core with NPT fittings attached to the endcap (left) and with Swagelok valve attached to the NPT fittings (right).

A2 VISCOSITY MEASUREMENT

Viscosities of nanoparticle dispersions and emulsions reported in this thesis are obtained from steady-rate sweep test using an ARES-LS1 rheometer (Figure A2.1) located in Dr. Pope's lab on the fourth floor of CPE. Steady-rate sweep test is conducted by varying magnitudes of steady shear rate at a constant temperature to measure steady viscosities. The following instructions were kindly provided by Dr. Do Hoon Kim, the lab manager in Dr. Pope's group, with additional annotations by the author:

Figure A2.1: Picture of a rheology test using an ARES-LS1 rheometer (Lee, 2009).

1. Turn on the machine by pressing the main power switch in the back.

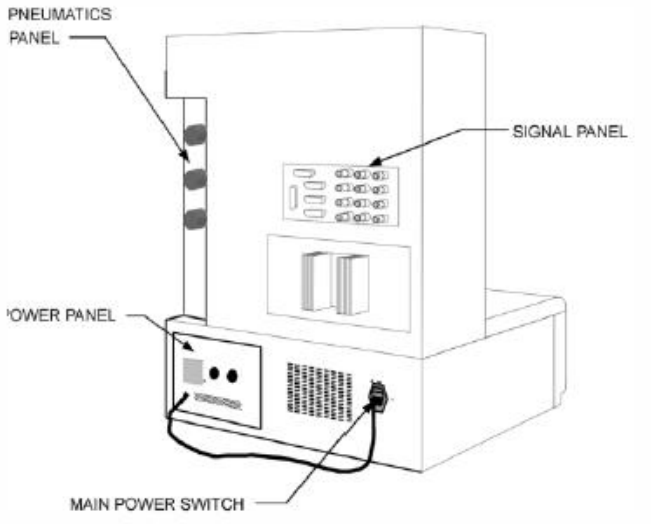

Figure A2.2: Turn on power by pressing the main power switch.

2. Turn on Fluid Bath.
3. Open TA Orchestrator Program. Select the temperature and turn on motor power on. At this point the lower fixture will not move.

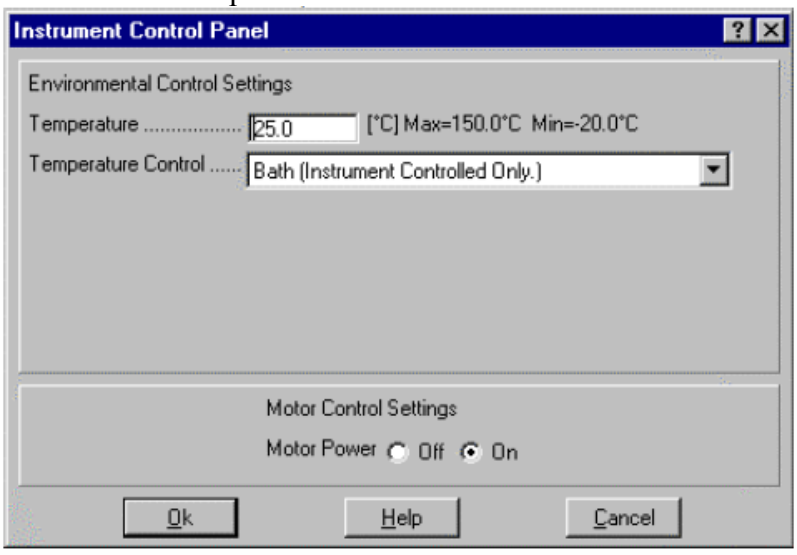

Figure A2.3: TA Orchestrator's Instrument Control Panel showing temperature and motor power options.

4. Attach the upper fixture gently. The fixture should be screwed on from both sides evenly. Do not tighten too hard; "hand-tight" should be enough. Double-wall fixture was used for nanoparticle dispersions and Couette fixture was used for emulsions.

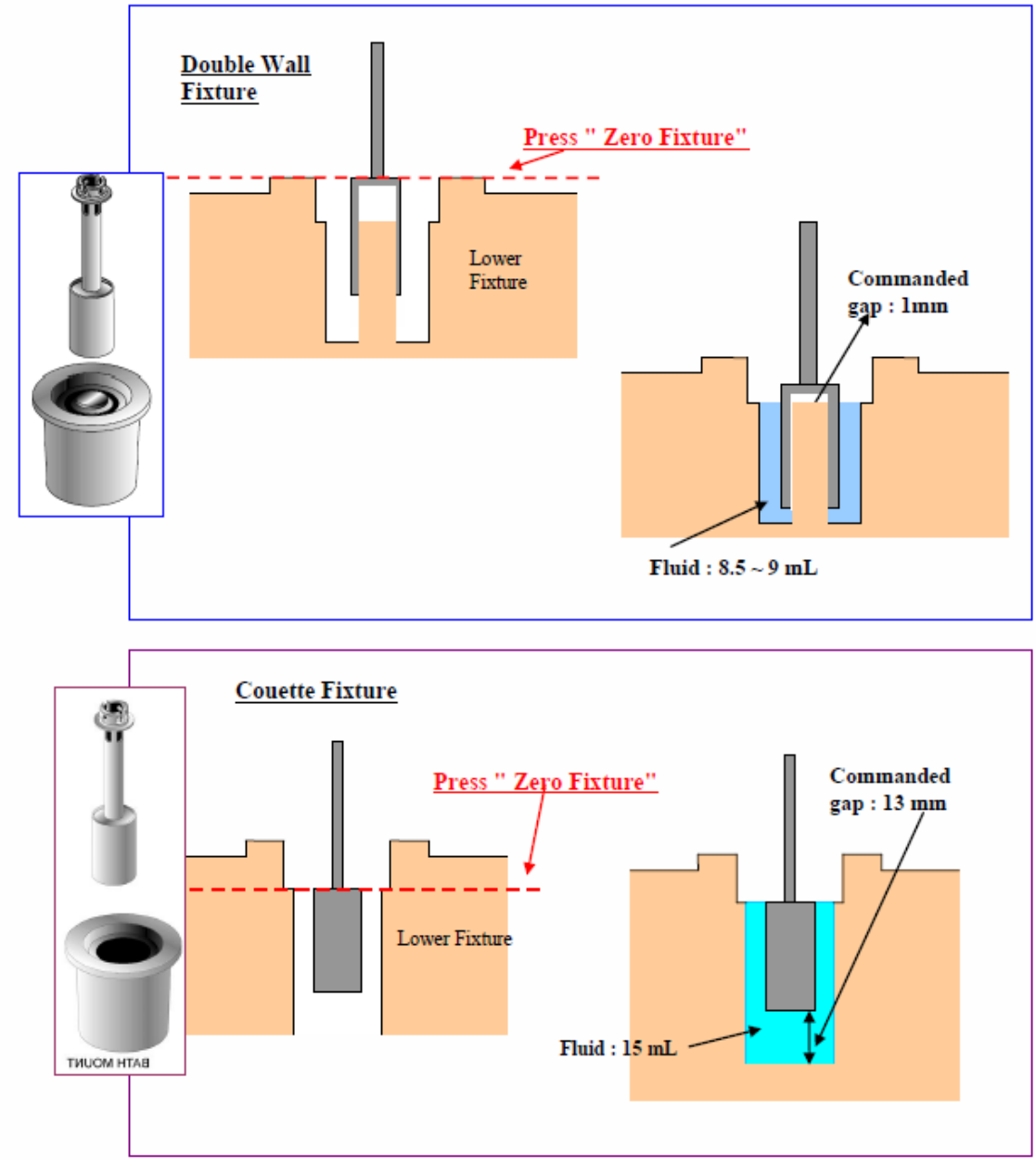

Figure A2.4: Illustrations of Double Wall Fixture and Couette Fixture.

5. Go to "Control" tab in TA Orchestrator and click on "Gap Control Panel." Offset the Torque and Force to zero. Under the Command Gap, enter 1 mm if using a double wall fixture, or 13 mm if using a Couette fixture.
6. Using the three buttons on the side of the machine, manually lower the upper fixture down until the top of the fixture is level with the top of the lower fixture. The top and bottom buttons brings the fixture up and down and the middle button is the accelerator.
7. After the fixture is lowered, press "Zero Fixture" in TA Orchestrator.
8. Use a syringe to inject fluid into the lower fixture. Double wall fixture requires 8.5 mL of sample while Couette requires 15 mL.
9. Press "Set Gap."
10. Wait for the temperature to go back down to the desired temperature. Then offset force to zero.
11. Under the "Control" tab, click on "Edit/Start Test." Save the test in the desired folder location. Under "Geometry," select Stored Geometries and choose double wall Couette or Couette. Then, go to Test Setup and select Steady and select Steady Rate Sweep Test. Finally, go to Edit Test and change the Initial Rate, Final Rate, Points per decay (usually 4), Delay before measure (usually 10), and Measure Time (usually 10). Directions per measurement should be always one.

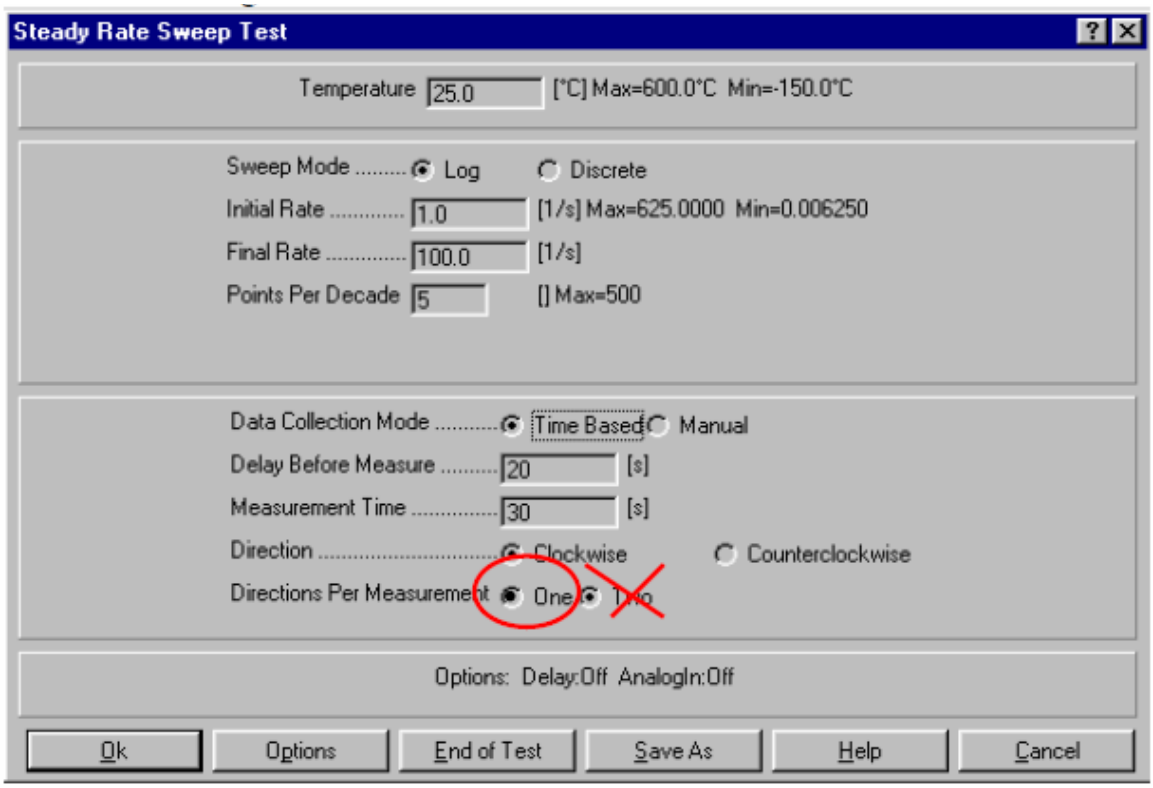

Figure A2.5: Setting up Steady Rate Sweep Test.

12. Select Begin Test.
13. After the test is complicated, click on the Gap icon and press Send to top.
14. Click on Control Panel and select Motor Power off.
15. Go to "Utilities" tab, under Service select Transducer 2.

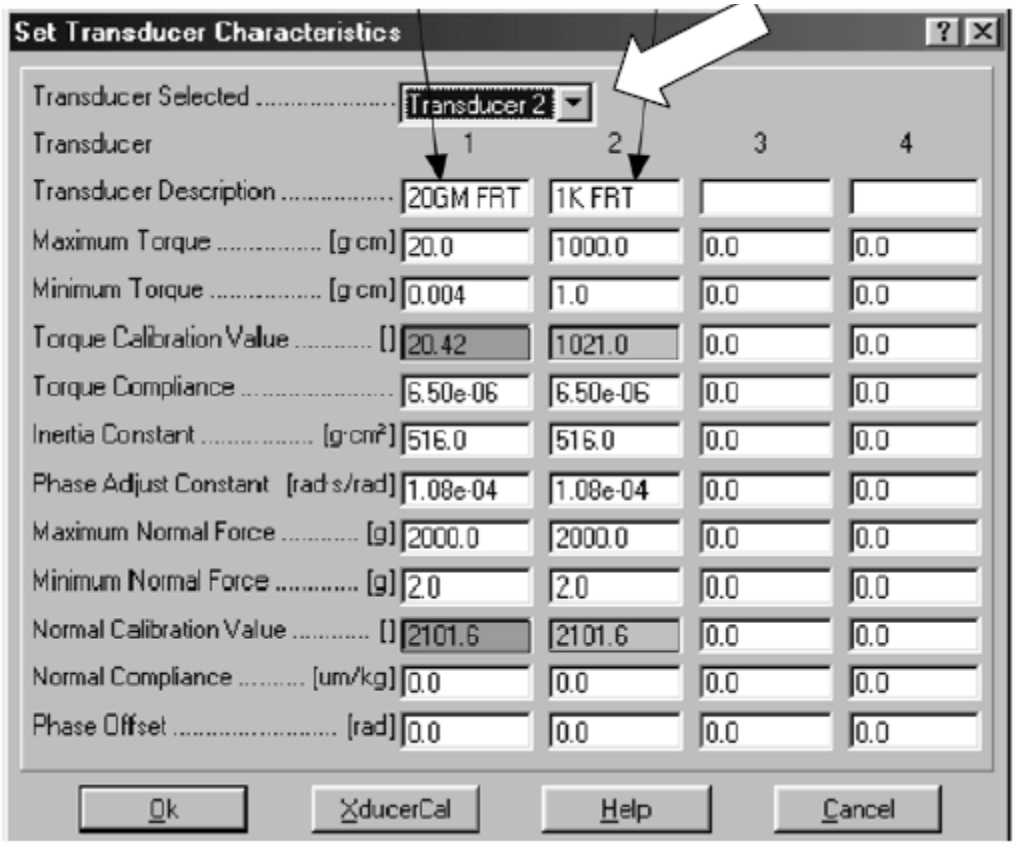

Figure A2.6: Selecting Transducer 2.

16. Remove upper and lower fixture for clean-up. Nanoparticle dispersions were cleaned with bleach and water and emulsions were cleaned using hexane, acetone and water.
17. Turn off first two switches of the Fluid Bath.
18. Turn off the main power on the rheometer machine.
19. Record the usage in the LOG file.

Any personnel outside of Dr. Pope's lab wishing to use this machine should receive training and make reservations with Dr. Do Hoon Kim.

A3 REFRACTIVE INDEX CALIBRATION

The presence of nanoparticles in water alters the refractive index (RI) of the aqueous phase, offering a simple method for measuring nanoparticle concentrations in effluent samples. In order to measure nanoparticle concentration, RI has to be calibrated with known concentrations of nanoparticles beforehand. The process is as follows:

1. Prepare different weight concentrations of nanoparticles dispersed in brine.
2. Measure RI of each sample using a refractometer (FisherScientific Model 334620) (Figure A3.1).
3. Prepare a graph of nanoparticle concentration as a function of RI.

The calibration curves can be used to find corresponding nanoparticle concentration for a measured RI. The calibration curves for each nanoparticle type used in this thesis are shown in Figure A3.2 through Figure A3.7.

Figure A3.1: FisherScientific Model 334620 Refractometer.

Nyacol DP9711

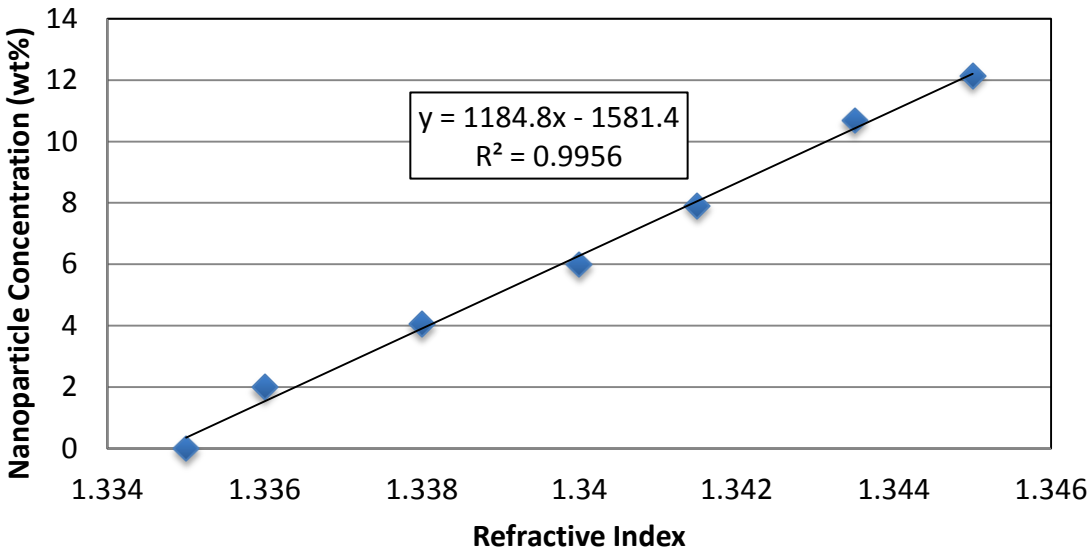

Figure A3.2: Nanoparticle concentration (wt%) as a function of refractive index for Nyacol DP9711 nanoparticle.

Nissan Chemical EOR-5XS

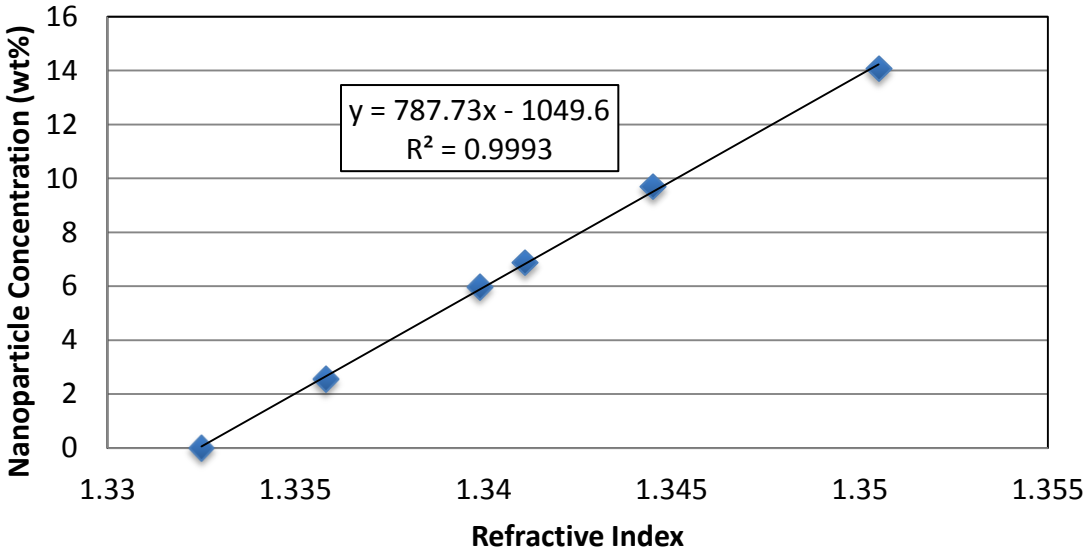

Figure A3.3: Nanoparticle concentration (wt%) as a function of refractive index for Nissan Chemical EOR-5XS nanoparticle.

Nissan Chemical EOR-12

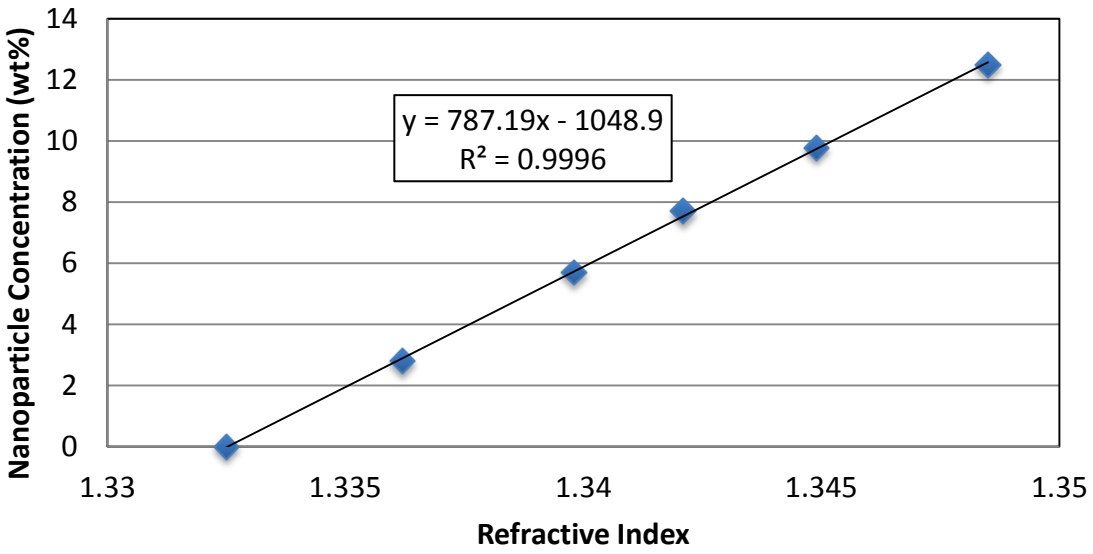

Figure A3.4: Nanoparticle concentration (wt%) as a function of refractive index for Nissan Chemical EOR-12 nanoparticle.

Nissan Chemical EOR-25

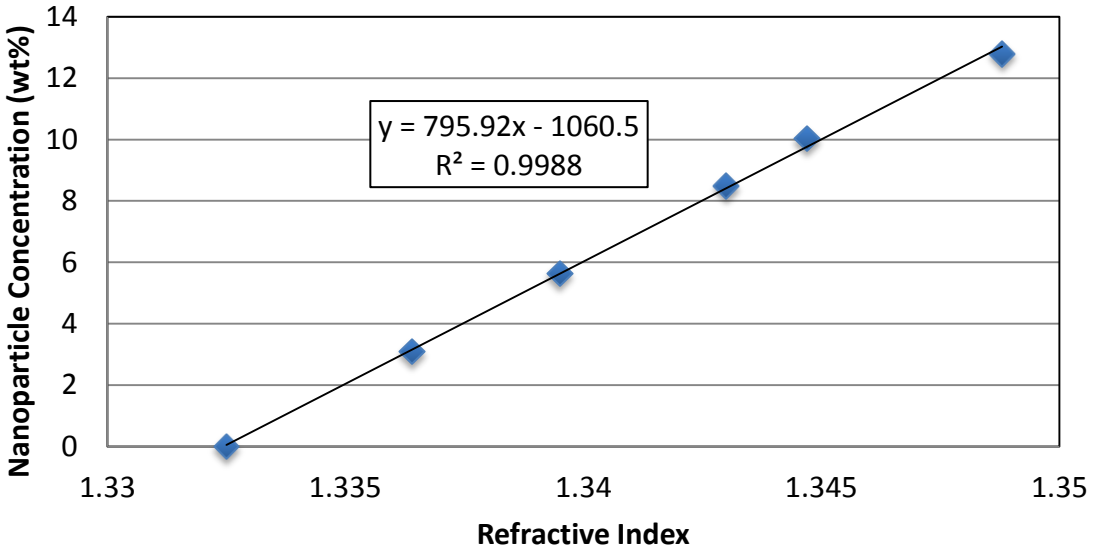

Figure A3.5: Nanoparticle concentration (wt%) as a function of refractive index for Nissan Chemical EOR-25 nanoparticle.

Nissan Chemical EOR-50

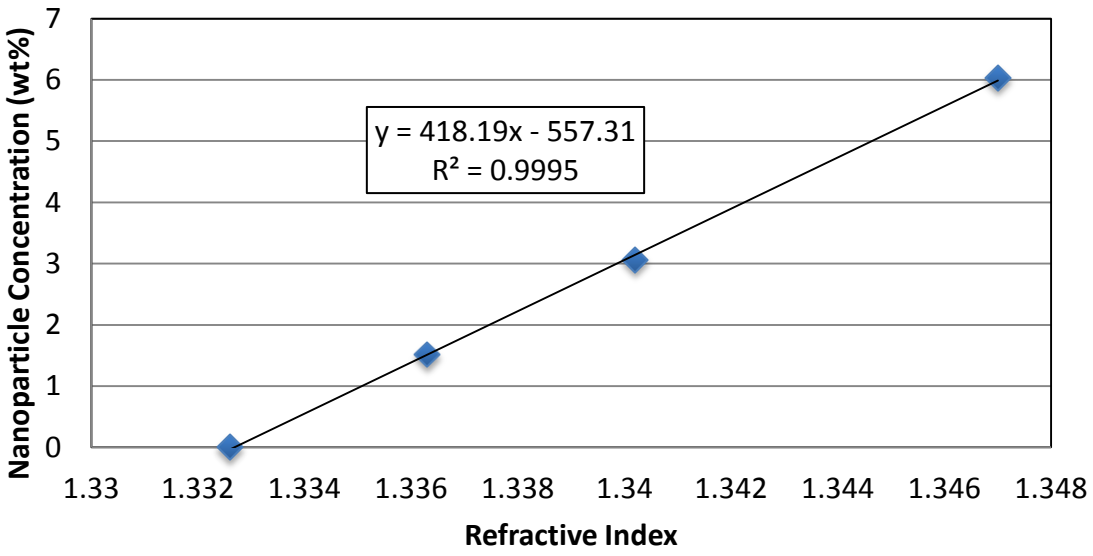

Figure A3.6: Nanoparticle concentration (wt%) as a function of refractive index for Nissan Chemical EOR-50 nanoparticle.

Nissan Chemical EOR-80

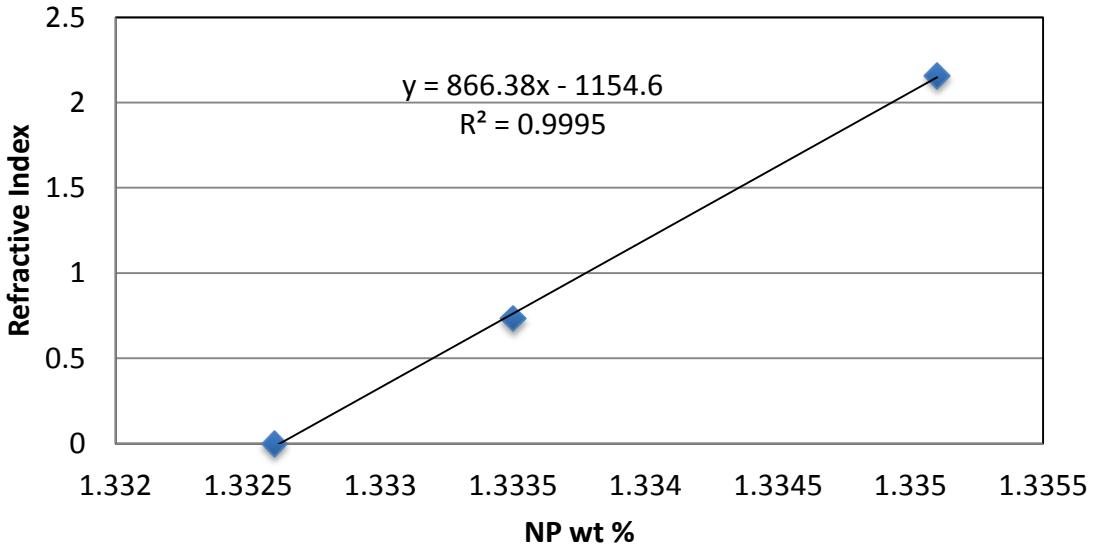

Figure A3.7: Nanoparticle concentration (wt%) as a function of refractive index for Nissan Chemical EOR-80 nanoparticle.

A4 UV-VIS CALIBRATION

In order to measure high-resolution effluent concentrations, UV-Vis machine has to be calibrated with known concentrations of tracer and nanoparticles beforehand. UV-Vis absorbance measurement of each sample requires a flow experiment where absorbance of the sample can be compared against absorbance of baseline fluid. The experimental set-up is shown in A4.1 and the procedure for the flow experiment is as follows:

17. Mount three glass columns (Column A and Column B) vertically.
18. Fill the pump with brine.
19. Fill Column A with mineral oil.
20. Fill Column B with sample to be injected into the core. Sample can be nanoparticle of varied concentrations, brine of varied concentration or a mixture of the two.
21. Set up tubing connections as shown in Figure A4.1.
22. Turn Valve 1 (V1) toward the filter element. Set the flow rate for 1 mL/min and start the syringe pump. Brine from the pump will enter the column, go through the UV-Vis detector, and end up at the fraction collector.
23. Start Chromeleon program for UV-Vis detector. Set autozero time to be between thirty minutes and an hour. Autozero feature sets the absorbance unit for steady-state brine flow as the baseline measurement.
24. After autozero is finished, turn V1 toward column A to start injecting sample in Column B into the core. Brine from the pump enters Column A from the bottom and displaces oil. The displaced oil enters Column B from the top and displaces sample into the core.
25. After injection is finished, turn V1 toward filter to begin postflush.

26. Correlate the peak absorbance unit to the sample concentration.

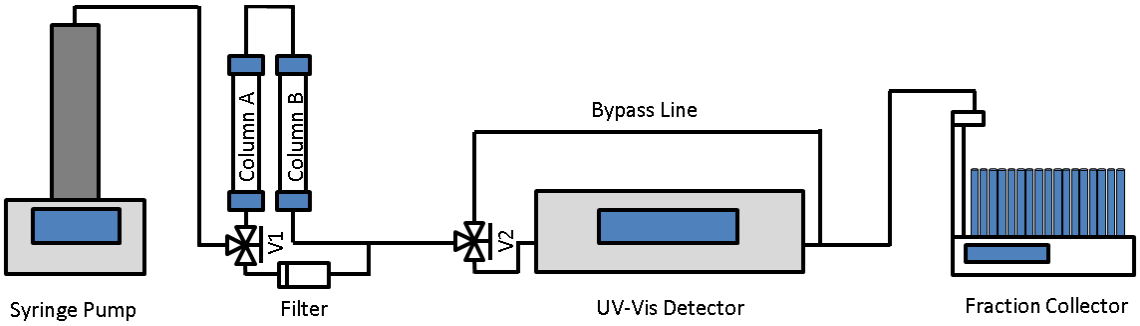

Figure A4.1: Schematic of flow experiment for calibration process.

Figure A4.2 shows the absorbance of 0.3 M NaI at a wavelength of 270 nm. During the first 30 minutes, the flow of 0.3 M NaCl reaches a steady state. At the 30-minute mark, the system was programmed to autozero the absorbance response. After making sure that the absorbance response is steady after autozero, the 0.3 M NaI sample was introduced at 36 minutes. The sample should be injected until the peak response is observed; in Figure A4.2 the peak response is about 700 mAU. Then, at about 45-minute mark, postflush began and the absorbance response drops back to 0. If absorbance response stays at 0 for about 5-10 minutes, the flow experiment is done and the pump is stopped.

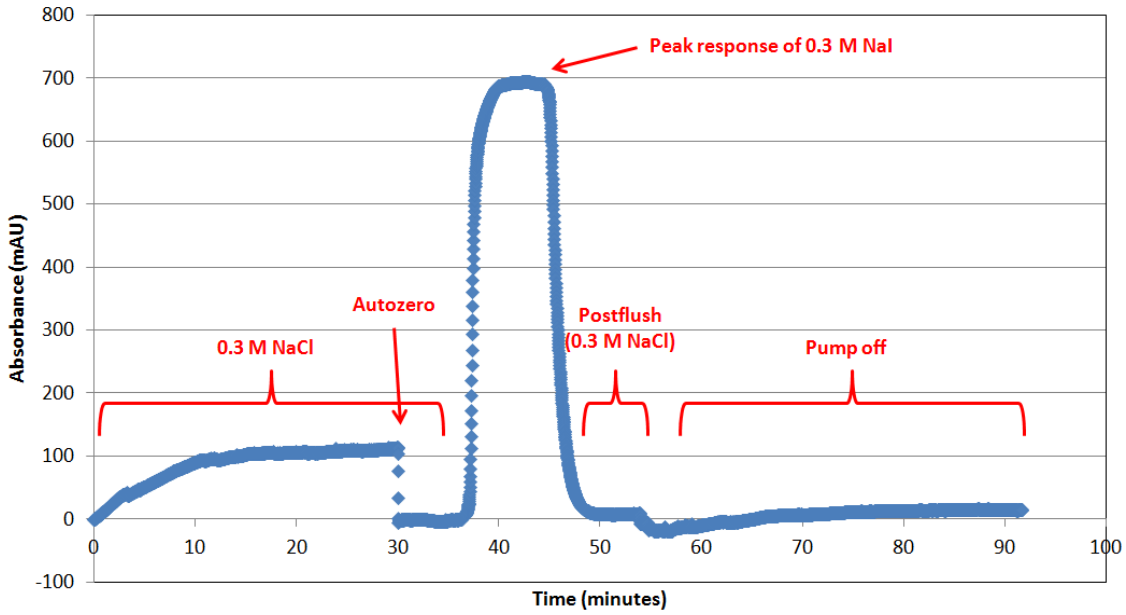

Figure A4.2: UV-Vis absorbance (mAU) as a function of time (minutes) for an injection of 0.3M NaCl, 0.3 M NaI, and 0.3 M NaCl.

In order to create a calibration curve, we have to determine which wavelengths the nanoparticles and the tracer are sensitive to. This wavelength scanning process was carried out by performing flow experiments with 0.3 M NaI or 5 wt% nanoparticle dispersion at different wavelengths. Figure A4.3 shows the result.

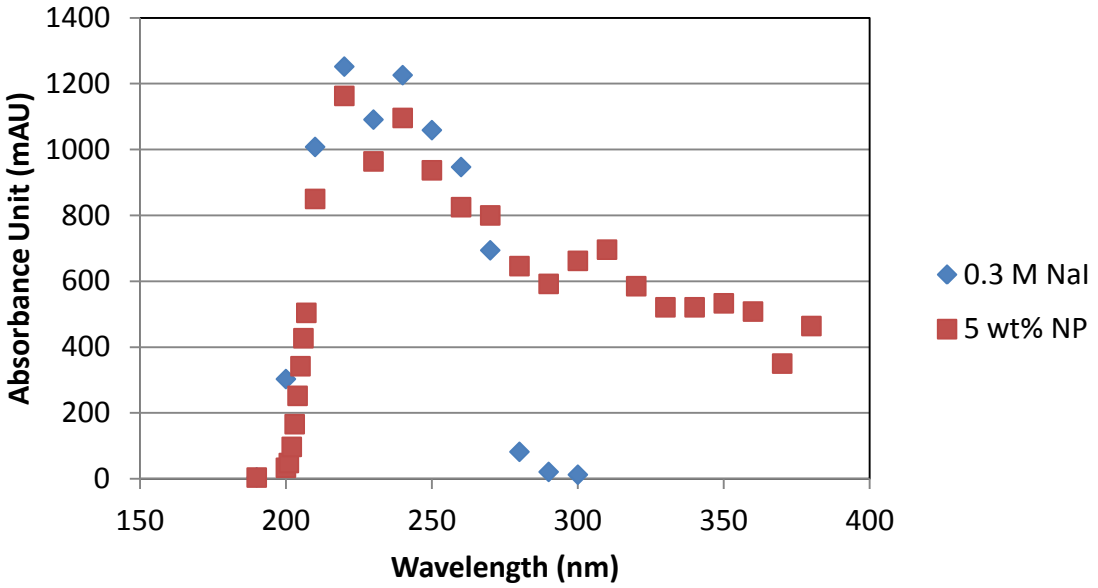

Figure A4.3: Absorbance of the tracer (blue) and nanoparticle (red) at different wavelengths.

It was easy to determine the wavelength channel for detecting nanoparticles as there is no absorbance response from the tracer past 300 nm. Therefore, the nanoparticle wavelength channel was determined to be 380 nm. Determining the wavelength channel for the tracer was more complicated as nanoparticles absorbance interfered with the tracer signal. The maximum absorbance unit that the machine can detect with no problem is around 1500 mAU; therefore, we chose a wavelength where the sum of absorbance responses from the tracer and the nanoparticle does not exceed 1500 mAU. The absorbance sum for 270 nm was smaller than 1500 nm, so 270 nm and 272 nm were both considered for the tracer channel.

After the wavelength channels are determined, calibration curves for the tracer and nanoparticle were created by doing flow experiments with varying concentrations of the tracer or the nanoparticles. Figure A4.4 and Figure A4.5 are the results.

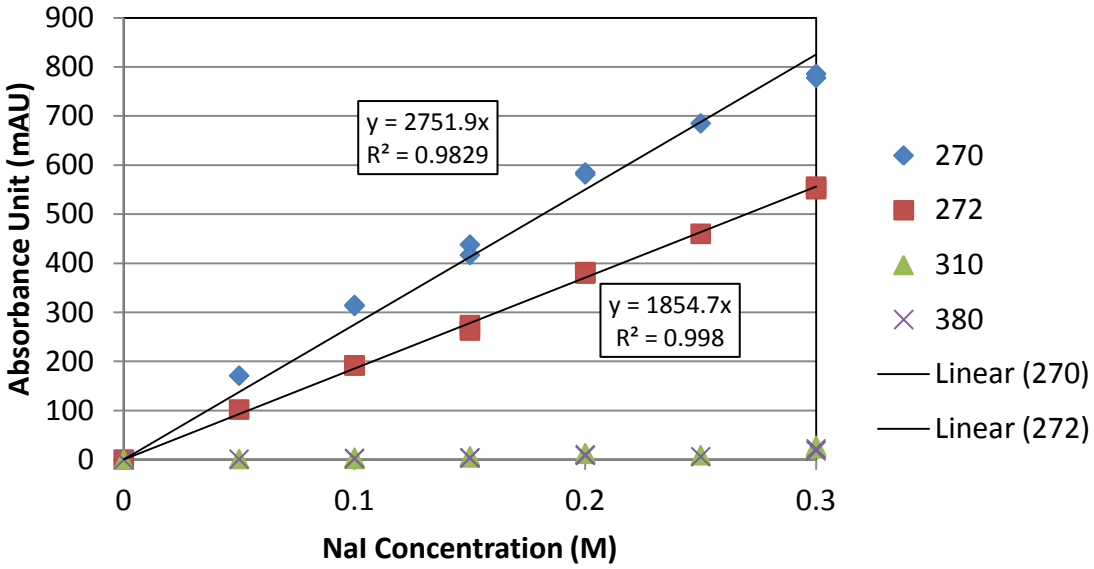

Figure A4.4: Absorbance response for different concentrations of the tracer (NaI) measured at different wavelengths.

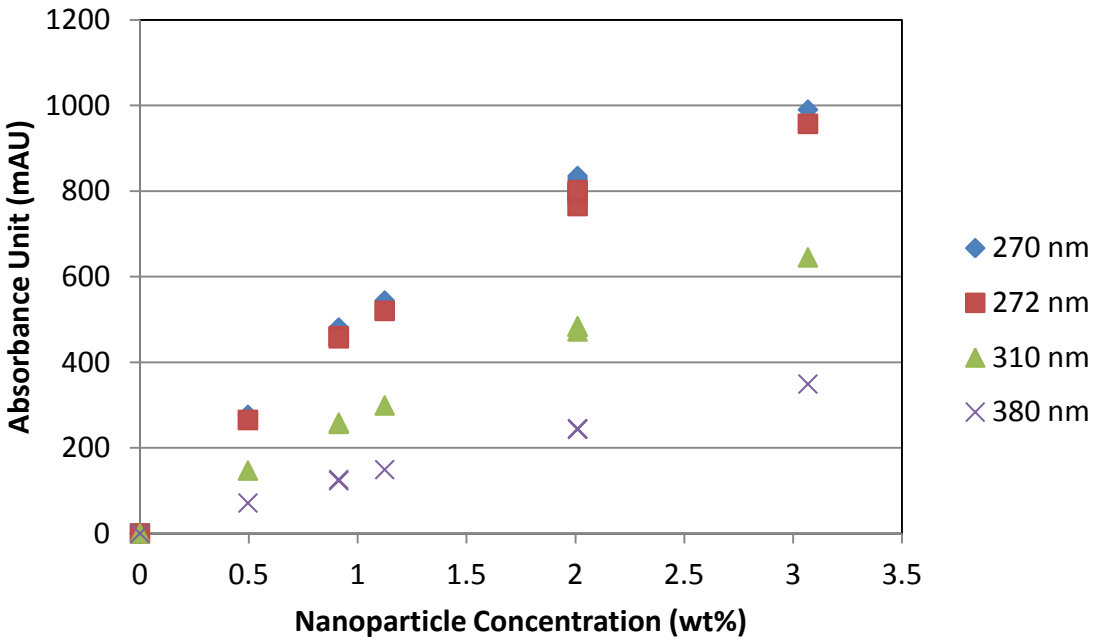

Figure A4.5: Absorbance response for different concentrations of nanoparticles measured at different wavelengths.

Figure A4.4 shows that the absorbance response grows linearly with increasing tracer concentration. The curve for 272 nm showed a better linearity, so 272 nm was chosen as the wavelength for the tracer. However, Figure A4.5 shows that absorbance response do not vary linearly with increasing nanoparticle concentrations, especially at higher nanoparticle concentrations. At low concentrations (up to 1.5 wt%), the absorbance curve was linear. Therefore, we decided the maximum nanoparticle concentration for single-phase flow experiments in Chapter 5 to be 1.5 wt%. These absorbance calibration curves will be used during UV-Vis data processing (Appendix A5) to decouple tracer signals from nanoparticle signals to obtain concentrations of both species in the effluent line.

A5 UV-VIS DATA PROCESSING

UV-Vis detector uses two wavelength channels to monitor the tracer and nanoparticles concentrations in the effluent line. 272-nm channel receives signals from both the tracer and nanoparticles while 180-nm channel receives signal from nanoparticles only. As a result, nanoparticle concentration can be directly calculated with 180-nm signal while tracer concentration needs to go through a process of eliminating the contribution from nanoparticles from the combined 272-nm signal. Figures A5.1 and A5.2 show absorbance data from 272 nm and 380 nm channels, respectively, obtained during Exp. A4, where 1 wt% nanoparticles dispersed in 0.3 M NaI were injected into a Berea sandstone core.

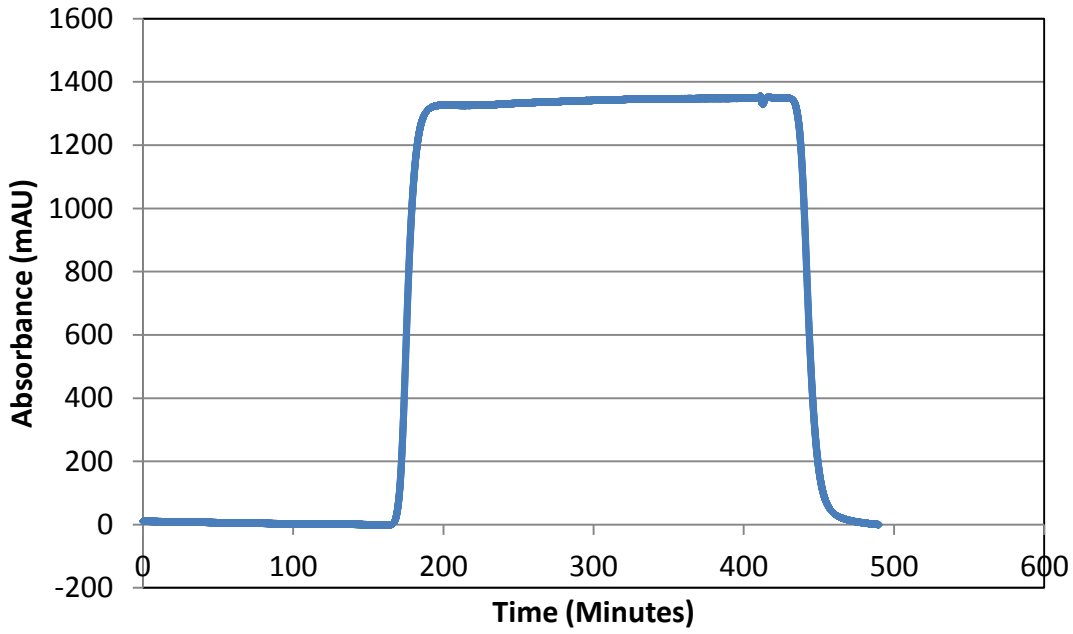

Figure A5.1: Absorbance at 272 nm as a function of time for the injection of 1 wt% nanoparticle dispersions and 0.3 M NaI into a Berea sandstone core (Exp. A4).

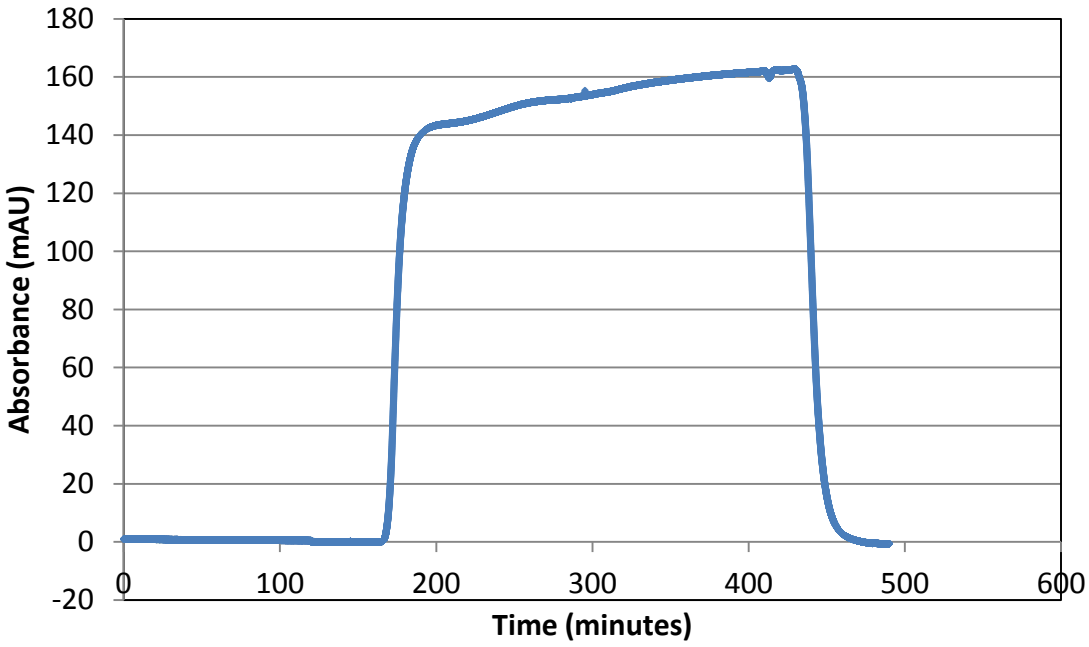

Figure A5.2: Absorbance at 380 nm as a function of time for the injection of 1 wt% nanoparticle dispersions and 0.3 M NaI into a Berea sandstone core (Exp. A4).

During this experiment, autozero was executed at 120 minute. After observing that the absorbance reading was stable, injection of sample started at 148.95 minutes. The start of sample injection was set as the new reference time (0 minute) and the absorbance curves are graphed as a function of PV injected as shown in Figure A5.3 and Figure A5.4.

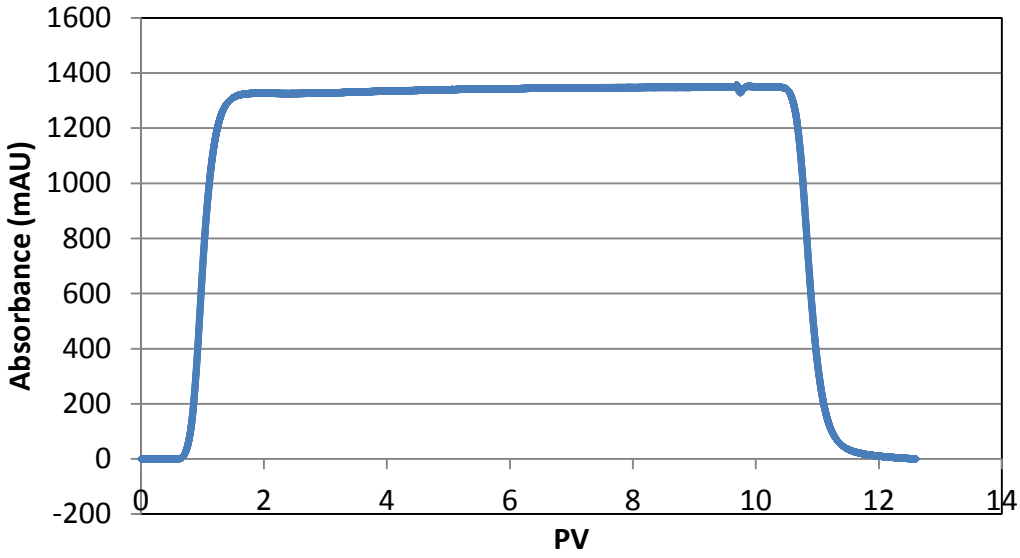

Figure A5.3: Absorbance at 272 nm as a function of PV for the injection of 1 wt% nanoparticle dispersions and 0.3 M NaI into a Berea sandstone core (Exp. A4).

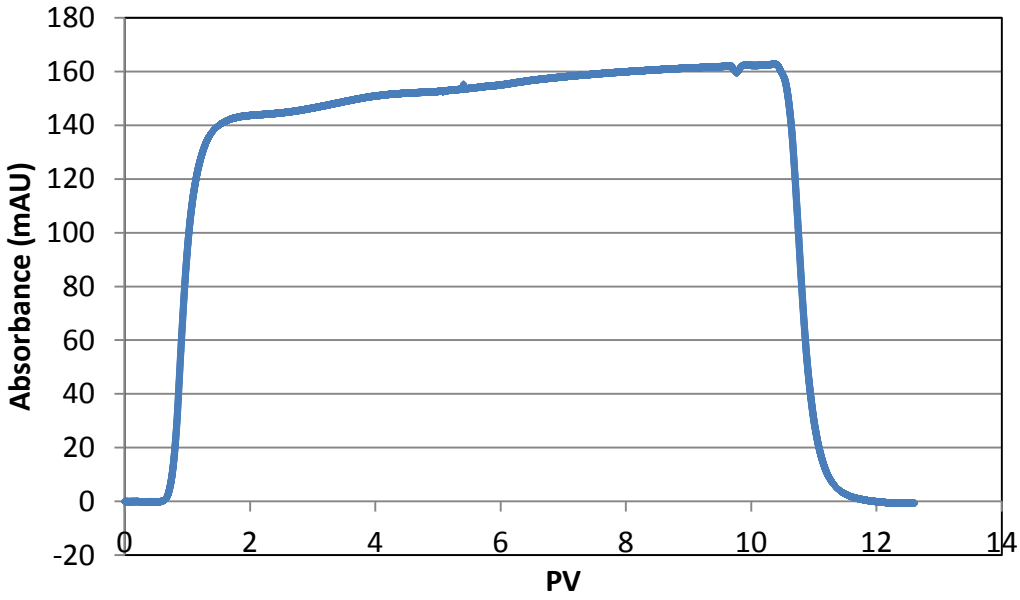

Figure A5.4: Absorbance at 380 nm as a function of PV for the injection of 1 wt% nanoparticle dispersions and 0.3 M NaI into a Berea sandstone core (Exp. A4).

The absorbance history at 380 nm can be converted to nanoparticle concentration using the relationship between nanoparticle concentration and absorbance unit obtained during calibrations. Then, the nanoparticle concentration is normalized by dividing the nanoparticle concentration by the injected concentration. Figure A5.5 shows the resulting normalized nanoparticle concentration history.

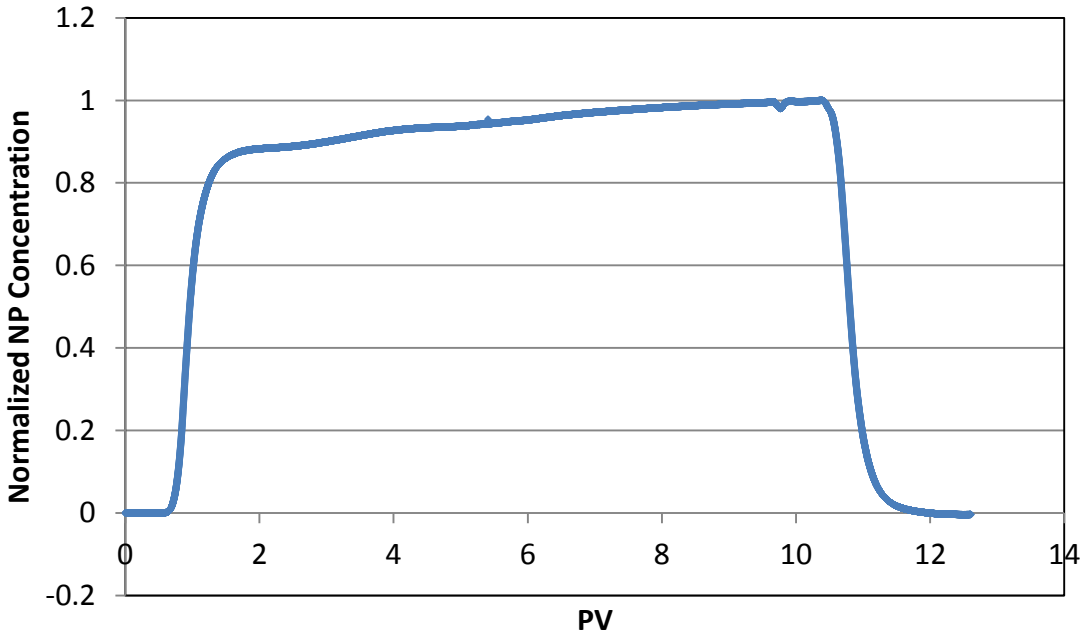

Figure A5.5: Normalized nanoparticle concentration as a function of PV for the injection of 1 wt% nanoparticle dispersions and 0.3 M NaI into a Berea sandstone core (Exp. A4).

With known concentrations of nanoparticle, the contribution of nanoparticle concentrations to the 272-nm absorbance signals can be calculated and subtracted from the total 272-nm absorbance. The resulting signal is the absorbance of the tracer at 272 nm. Using the relationship between tracer concentration and absorbance obtained from tracer calibrations, tracer concentration as a function of time can be calculated. Then, the

tracer concentration is normalized by dividing the tracer concentration by the injected concentration. Figure A5.6 shows the resulting normalized tracer concentration history.

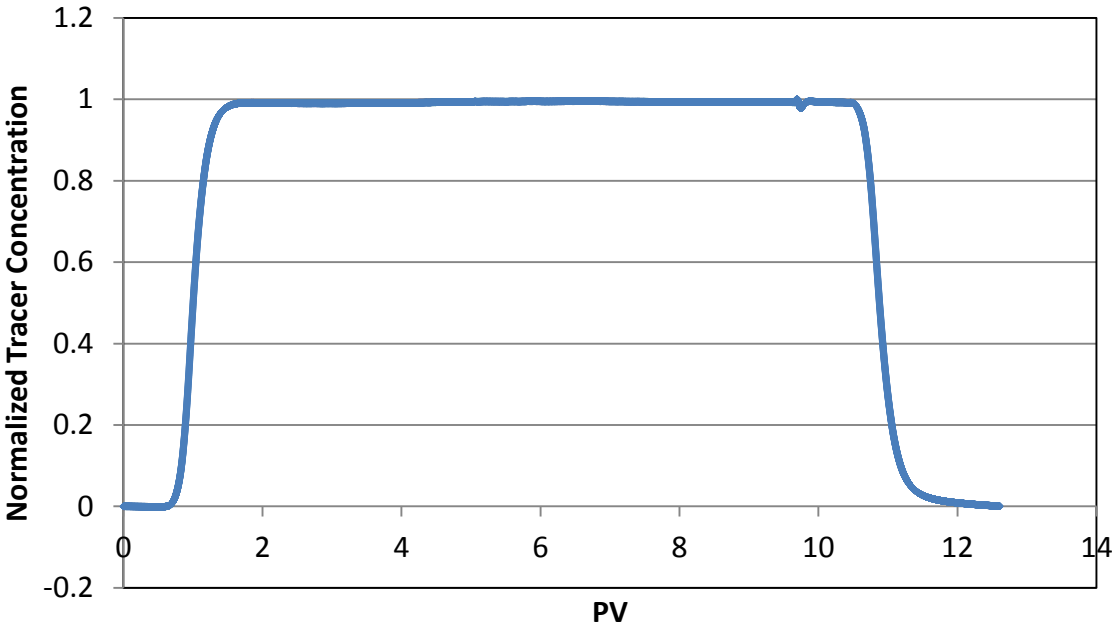

Figure A5.6: Normalized tracer concentration as a function of PV for the injection of 1 wt% nanoparticle dispersions and 0.3 M NaI into a Berea sandstone core (Exp. A4).

Integration of the area under the concentration history curve gives the total PV recovered for each species. By comparing the results from the tracer curve and the nanoparticle curve, the amount of nanoparticles retained in the core can be calculated. The summed PV of the tracer can also be crossed-checked with the actual volume of the sample injected; the two usually fall within 1% error (this particular analysis for Exp. A4 had 0.2 % error).

References

Aminzadeh, B. Experimental Measurement of Sweep Efficiency During Multi-Phase Displacement in the Presence of Nanoparticles, Ph.D. Dissertation, The University of Texas at Austin (2013).

Aminzadeh, B., Z. Zhang, D.H. Chung, S.L. Bryant, C. Huh, and D.A. DiCarlo. Increasing CO_2 storage efficiency using commercial nanoparticles, Presented at the Carbon Capture Utilization and Storage (CCUS) Conference, Pittsburgh, PA (2013).

Berg, S., A.W. Cense, J.P. Hofman, and R.M.M. Smits: Two Phase Flow in Porous Media with Slip Boundary Condition, *Transport in Porous Med.*, 74, 275-292 (2008).

Binks, B.P., and T.S. Horozov. Colloidal Particles at Liquid Interfaces: An Introduction. Colloidal Particles at Liquid Interfaces, Chapter 1, Binks, B.P., and Horozov, T.S., eds., 85-152, Wiley-VCCH Verlag (2006).

Bragg, J.R. Solids-Stabilized Emulsion, *U.S. Patent*, 5910467 (1999).

Braggs, J.R., and R. Varadaraj. Solids-Stabilized Oil-in-Water Emulsion and a Method for Preparing the Same, *World Intellectual Property Organization*, WO 03/057793, (2003).

Buongiorno, J. Convective Transport in Nanofluids, *Journal of Heat Transfer*, 128, 240 - 250 (2006).

Caldelas, F.M. Experimental Parameter Analysis of Nanoparticle Retention in Porous Media, M.S.E. Thesis, The University of Texas at Austin (2010).

Cho, K., X. Xang, S. Nie, Z. Chen, and D.M. Shin. Therapeutic Nanoparticles for Drug Delivery in Cancer, *Clinical Cancer Research*, 14, 1310-1316 (2008).

Dawson, R. and R.B. Lantz. Inaccessible Pore Volume in Polymer Flooding, *SPE J.*, 253, SPE3522 (1972).

da Rocha, S.R.P., K.L. Harrison, and K.P. Johnston. Effect of surfactants on the interfacial tension and emulsion formation between water and carbon dioxide, *Langmuir*, 15, 419-428 (1999).

DiCarlo, D.A., B. Aminzadeh, M. Roberts, D.H. Chung, S.L. Bryant, and C. Huh. Mobility control through spontaneous formation of nanoparticle stabilized emulsions, *Geophysical Research Letters*, Vol. 38, L24404 (2011).

DiCarlo, D.A., A. Sahni, and M.J. Blunt. Three-phase relative permeability of water-wet, oil-wet, and mixed-wet sandpacks, *SPE J.*, 5, 82-91 (2000).

Dickson, J.L., B.P. Binks, K.P. Johnston. Stabilization of Carbon Dioxide-in-Water Emulsions with Silica Nanoparticles, *Langmuir*, 20, 7976-7983 (2004).

Espinosa, D. Nanoparticle Stabilized Supercritical CO_2 Foams for Potential Mobility Control Applications, M.S.E. Thesis, The University of Texas at Austin (2011).

Happel, J. Viscous Flow in Multiparticle Systems: Slow Motion of Fluids Relative to Beds of Spherical Particles, *AlCheE J.*, 4, 197-201 (1958).

Haines, W.B. Studies in the Physical Properties of Soil. IV. A Further Investigation to the Theory of Capillary Phenomena in Soils, *Jour. Agri. Sci.*, 17, 264 (1927).

Hariz, T.R. Nanoparticle-Stabilized CO_2 Foams for Potential Mobility Control Applications, M.S.E. Thesis, The University of Texas at Austin (2012).

IPCC (Intergovernmental Panel on Climate Change) Fourth Assessment Report (2007)

Kovscek, A.R., G.-Q. Tang and C.J. Radke. Verification of Roof snap off as a foam-generation mechanism in porous media at steady state, *Colloids and Surfaces A: Physicochem. Eng. Aspects*, 302, 251 - 260 (2007).

Krishnamurthy, S., P. Bhattacharya, and P.E. Phelan. Enhanced Mass Transport in Nanofluids, *Nano Letters*, 6, No. 3, 419 - 423 (2006).

Lake, L.W. Enhanced Oil Recovery. Englewood Cliffs, NJ: Prentice Hall (1989).

Lecoanet, H.F., J.-Y. Bottero, M.R. Wiesner. Laboratory Assessment of the Mobility of Nanomaterials in Porous Media, *Environ. Sci. Technol.*, 38, 5164-5169 (2004).

Lee, S. Development of a Comprehensive Rheological Property Database for EOR Polymers, M.S.E. Thesis, The University of Texas at Austin (2009).

Melrose, J.C. Wettability as Related to Capillary Action in Porous Media, Presented at the SPE-AIChE Joint Symposium on Wetting and Capillary in Fluid Displacement Processes, Kansas City, MO, SPE 1085 (1965).

Mennella, A., S.L. Bryant, T.P. Lockhart. Analysis of high-dispersion tracer tests in cores containing polymer gels, *Journal of Petroleum Science and Engineering*, 23, 201-212 (1999).

Murphy, M.J. Experimental Analysis of Electrostatic and Hydrodynamic Forces Affecting Nanoparticle Retention in Porous Media, M.S.E. Thesis, The University of Texas at Austin (2012).

O'Melia, C.R. Particle-Particle Interactions in Aquatic Systems, *Colloids and Surfaces*, 38, 255-271 (1989).

Patra, J.K., and S. Gouda. Application of Nanotechnology in Textile Engineering: An Overview, *JETR*, 5, 104-111 (2013).

Pickering, S.U. Emulsions, CXCVI, *J. Chem. Soc.*, 91, 2001 (1907).

Priezjev, N.V. Rate-Dependent Slip Boundary Conditions for Simple Fluids, *Physical Review E*, Vol. 75, 051605 (2007).

Qi, R., T.C. LaForce, M.J. Blunt. Design of Carbon Dioxide Storage in Aquifers, *International Journal of Greenhouse Gas Control*, 3, 195-205 (2009).

Roberts, M.R. Shear-Induced Emulsions Stabilized with Surface-Modified Silica Nanoparticles, M.S.E. Thesis, The University of Texas at Austin (2011).

Rodriguez-Pin, E. Grain-Scale Mechanisms of Particle Retention in Saturated and Unsaturated Granular Materials, Ph.D. Dissertation, The University of Texas at Austin (2010).

Rodriguez-Pin, E., M.R. Roberts, H. Yu, C. Huh, and S.L. Bryant. Enhanced Migration of Surface-Treated Nanoparticles in Sedimentary Rocks, Presented at the SPE Annual Technical Conference and Exhibition, New Orleans, LA, SPE 124418 (2009).

Rueckets, T., K. Kim, E. Joselevich, G. Tseng, C. Cheung, and C.M. Lieber. Carbon nanotube-based nonvolatile random access memory for molecular computing, *Science*, 289, 94-97 (2000).

Roof, J.G. Snap-Off of Oil Droplets in Water-Wet Pores, *SPE J.*, 10, 85-90 (1970).

Stuart, M.A.C., W.T.S. Huck, J. Genzer, M. Muller, C. Ober, M. Stamm, G.B. Sukhorukov, I. Szleifer, V.V. Tsukruk, M. Urban, F. Winnik, S. Zauscher, I. Luzinov, and S. Minko. Emerging Applications of Stimuli-Responsive Polymer Materials, *Nature Materials*, 9, 101-113 (2010).

UGCRP (U.S. Global Change Research Program) Global Climate Change Impacts in the United States (2009).

Vargaftik, N. Tables of the Thermophysical Properties of Liquid and Gases, 2nd ed., Hemisphere, Washington, D.C (2005).

Yu, H. Transport and Retention of Surface-Modified Nanoparticles in Sedimentary Rocks, Ph.D. Dissertations, The University of Texas at Austin (2012).

Zhang, T. Modeling of Nanoparticle Transport in Porous Media, Ph.D. Dissertation, The University of Texas at Austin (2012).

Zhang, T., A. Davidson, S.L. Bryant, and C. Huh. Nanoparticle-Stabilized Emulsions for Applications in Enhanced Oil Recovery, Presented at the SPE Improved Oil Recovery Symposium, Tulsa, OK, SPE 129885 (2010).

Zhang, T., M.R. Roberts, S.L. Bryant, and C. Huh, C. Foams and Emulsions Stabilized with Nanoparticles for Potential Conformance Control Applications, Presented at the SPE International Symposium on Oilfield Chemistry, Woodlands, TX, SPE 121744 (2009).

Vita

Doo Hyun Chung was born in Seoul, South Korea. He first came to the United States in 2002 and attended the Hill School in Pottstown, PA. He graduated with Distinction from Harvey Mudd College in Claremont, CA with a B.S. degree in Engineering in May, 2011. He started his M.S. degree in Petroleum Engineering in August, 2011 and worked as a graduate research assistant under the supervision by Dr. Steven Bryant. He worked as a summer intern at Chevron Corporation in the summer of 2012 and plans to return for a full-time position in August of 2013.

Permanent email: cdhdc77@gmail.com

This thesis was typed by Doo Hyun Chung.